Osaka University Knowledge Archive

Title	低電界エレクトロレフレクタンスによるシリコンの光学的臨界点構造に関する研究
Author(s)	近藤, 和夫
Citation	大阪大学, 1977, 博士論文
Version Type	VoR
URL	https://doi.org/10.18910/31652
rights	
Note	Abstract 著者氏名のヨミに誤りあり。正しくは「コンドウ　カズオ」

Osaka University Knowledge Archive : OUKA

https://ir.library.osaka-u.ac.jp/

Osaka University

STUDY OF OPTICAL CRITICAL-POINT STRUCTURES IN SILICON BY LOW-FIELD ELECTROREFLECTANCE

Kazuo Kondo
Department of Electronics, Osaka University

March 1977

STUDY OF OPTICAL CRITICAL-POINT STRUCTURES IN SILICON BY LOW-FIELD ELECTROREFLECTANCE

by

Kazuo Kondo

March 1977

STUDY OF OPTICAL CRITICAL-POINT STRUCTURES IN SILICON BY LOW-FIELD ELECTROREFLECTANCE

Kazuo Kondo

Department of Electronics
Osaka University, Suita, Osaka, Japan

March 1977

The analytical method of optical critical-point structures by low-field electroreflectance (ER) is described. The three fundamental parameters of optical-critical points, i.e., energies, symmetry locations in the Brillouin zone, and interband-reduced masses are obtained by the line shapes and the polarization dependences of low-field ER spectra. In addition, uniaxial-stress effects on low-field ER give the symmetry locations and the deformation-potential parameters at critical points.

These methods are applied to the E_0', E_1, and E_2 optical structures in Si using the Schottky-barrier ER technique. The fundamental features of critical points related to these structures are analyzed precisely. From the line-shape analysis using the low-field resonant function, we show that the 3.4 eV complexities consist of two critical points, E_0' ($E_g = 3.294 \pm 0.005$ eV; 300 K) and E_1 ($E_g = 3.412 \pm 0.005$ eV; 300 K). Moreover, the E_2 structures consist of three critical points, $E_2(1)$ ($E_g = 4.336 \pm 0.010$ eV; 90 K), $E_2(2)$ ($E_g = 4.459 \pm 0.010$ eV; 90 K), and $E_2(3)$ ($E_g = 4.598 \pm 0.010$ eV; 90 K). As for the symmetry analysis (and the reduced-mass relation), E_1 is assigned conclusively to the $\Lambda_3^v \rightarrow \Lambda_1^c$ or $L_{3'}^v \rightarrow L_1^c$ transition ($\mu_T \ll |\mu_L|$, $\mu_T > 0$, $\mu_L < 0$; M_1 type), $E_2(1)$ is conclusively to the $\Sigma_2^v \rightarrow \Sigma_3^c$ transition ($1/\mu_{T2} + 1/\mu_L = 4/\mu_{T1}$, $\mu_{T1} > 0$, $\mu_{T2}\mu_L < 0$; M_1 type), and $E_2(3)$ is probably to the $\Delta_5^v \rightarrow \Delta_1^c$ transition near the X point ($|\mu_T| \gg \mu_L$, $\mu_T < 0$, $\mu_L > 0$; M_2 type). The interband deformation-potential parameters of the E_1 critical point are also determined

from the uniaxial-stress measurements.

As a synthesis, the $E_{4-5}(\vec{k})$ energy contours of Si are constructed from the experimental results.

ACKNOWLEDGMENTS

I would like to express my appreciation to Dr. A. Moritani for his continued encouragement and guidance throughout the course of this work.

I wish to express my gratitude to Professor J. Nakai and Professor C. Hamaguchi for their kind advices and guidance throughout my graduate research.

I also wish to acknowledge Professors A. Mitsuishi, S. Nakamura, and T. Hanawa for the critical reading of this thesis.

I wish to show my deep recognition to Dr. D. E. Aspnes of Bell Laboratories for his suggestions and comments on the symmetry analysis by low-field electroreflectance, to Professor K. Suzuki of Department of Physics, Osaka University for many enjoyable discussions, and to Dr. G. Kano of Matsushita Electronics Corporation for determining the crystal orientations of Si used in this experiment.

I am indebted to Dr. Y. Sasaki, Mr. M. Iwamoto, Mr. M. Yokogawa, Mr. H. Yokomoto, and Mr. H. Kubo for their active help with both the experiments and the data analyses.

I also wish to thank Chief Professor S. Kodama, Professors O. Kakusho, Z. Kitamura, J. Koyama, Y. Matsuo, H. Ozaki, E. Sugata, K. Terada, and K. Ura for many helpful lectures and encouragements.

The financial support of the Japan Scholarship Foundation is greately acknowledged.

I am very greateful to my parents for their endless encouragement and support.

CONTENT

Page

I. INTRODUCTION 1

II. THEORY 6

A. Optical Dielectric Function and Critical Point 6

a. Optical Dielectric Function. 6

b. Optical Critical Point 9

B. Low-Field Electroreflectance 13

C. Symmetry Analysis by Low-Field Electroreflectance. . . . 17

D. Uniaxial-Stress Effects on Low-Field Electroreflectance. 23

III. EXPERIMENTAL 35

A. Sample Construction. 35

B. Measurement Techniques 35

IV. RESULTS AND ANALYSIS 39

A. E_0' and E_1 Structures. 39

a. Best-Fit Analysis. 39

b. Symmetry Analysis. 44

c. Uniaxial-Stress Effects. 47

B. E_2 Structures. 60

a. Best-Fit Analysis. 60

b. Symmetry Analysis. 63

V. SYNTHESIS. 69

VI. DISCUSSION 73

A. E_0' and E_1 Structures. 73

B. E_2 Structures. 77

C. Synthesis. 81

VII. CONCLUSIONS. 85

A. Theory 85

B. Experiment 85

	Page
APPENDIX A	87
APPENDIX B	90
REFERENCES	96
VITA	105

LIST OF TABLES

TABLE | Page

I. Symmetry properties for Γ, Δ, Λ, L, and Σ critical points in diamond-type crystals. 12

II. Effective components of the vector potential for the star of $\vec{K}_0 = (0, 0, k_0)$, (k_0, k_0, k_0), and $(k_0, k_0, 0)$ in diamond-type crystals. The effective components are primed and the actual components are unprimed. (After Kane.[63]) 20

III. Polarization dependences of low-field electroreflectance form factor F for Γ, Δ, Λ, L, and Σ critical points in diamond-type crystals. Longitudinal geometry is used and $(1\bar{1}0)$ face is preferred for the plane of reflection; electric field $\hat{\mathcal{E}} = (1/\sqrt{2}, -1/\sqrt{2}, 0)$. θ is the polarization angle of the incident light measured with respect to the crystallographic $\hat{z}$ direction. The polarization anisotropy is defined as $r \equiv F_{[001]}/F_{[110]}$ (or $s \equiv F_{[111]}/F_{[11\bar{2}]}$); the subscript of F denotes the polarization of the incident light. (After Kondo and Moritani.[31]) 21

IV. Effective irreducible components of the strain tensor for the star of $\vec{K}_0 = (k_0, k_0, k_0)$ in diamond-type crystals. The effective components are primed and the actual components are unprimed. (After Kane.[63]). 28

V. Energy shift ΔE and electroreflectance form factor F for the degenerate U_3 band in the Λ direction. Spin-orbit interaction is neglected. The factor F has been summed over the eight equivalent components. The subscript of F denotes the polarization of the light. (After Kondo and Moritani.[31]) 30

VI. Energy shift ΔE and electroreflectance form factor F for the degenerate U_5 band in the Δ direction. Spin-orbit interaction is neglected. The factor F has been summed over the six equivalent components. The subscript of F denotes the polarization of the light. (After Kondo and Moritani.[31]) 32

VII. Energy shift ΔE and electroreflectance form factor F for the degenerate U_4 band at the Γ point. Spin-orbit interaction is

TABLE		Page
	neglected. The subscript of F denotes the polarization of the light	34
VIII.	Critical-point parameters of Si in the energy range of E_0' and E_1 transitions as obtained from electroreflectance (ER), wavelength-modulated reflectance (WMR), and thermoreflectance (TR) measurements. RT stands for room temperature	42
IX.	Deformation potentials of the $\Lambda_3^v (L_{3'}^v) - \Lambda_1^c (L_1^c)$ critical point of Si. The previously reported values for Si and Ge are listed for comparison. Experimentally determined and calculated values of pressure coefficients of Si are also listed. RT stands for room temperature	53
X.	The results of the best-fit analysis assuming the existence of two or three critical points in the E_2 spectral region. The data were taken at 90 K using the Schottky-barrier electroreflectance technique. (After Kondo and Moritani.[35])	64
XI.	Calculated critical-point energies of Si in the E_0' and E_1 spectral region (in eV)	75
XII.	Critical-point parameters of Si in the energy range of E_2 transitions as obtained from electroreflectance (ER), wavelength-modulated reflectance (WMR), and thermoreflectance (TR) measurements	78
XIII.	Calculated critical-point energies of Si in the E_2 spectral region (in eV)	80
XIV.	Symmetry group of $\vec{K}_0$ for the first Brillouin zone in diamond-type (Fd3m) crystals	84
XV.	Electroreflectance form factor F for high symmetry Γ, Δ, Λ, L, and Σ critical points in diamond-type crystals. Longitudinal geometry with unpolarized light is used for the (001), (111), and $(1\bar{1}0)$ faces. μ_{T1}, μ_{T2}, and μ_L are defined by Eq. (23)	91

LIST OF FIGURES

FIGURE Page

1. Schematic diagram of electric field modulation process where the lattice periodicity is destroyed. The effect of the perturbation on the energy band structure and optical transition is shown at the left. (After Aspnes.[76]). 15

2. Experimental setup for electroreflectance measurements. The details are shown in the text 36

3. Schematic diagram of (a) the sample cell and (b) the stress apparatus. A: support tube, B: sample cell, C: pushing rod, D: round piece, E: paper sheet, F: sample, G: rectangular piece. A, B, C, D, and G are made of stainless steel 38

4. Schottky-barrier ER spectrum of Si in the energy range of E_0' and E_1 transitions at room temperature (RT). Open circles are the experimental results, taken on $(1\bar{1}0)$ face for [001] polarization in the low-field modulation limit. Short-dashed and long-dashed lines are the calculated three-dimensional (L^{3D}) and two-dimensional (L^{2D}) line shapes, respectively. Solid line is the sum of the above two line shapes. (After Kondo and Moritani.[31]) 40

5. Seraphin coefficients of the air-Ni-Si three phase system at room temperature (RT), calculated from the reflectivity spectra of Ni and Si. The results are shown with the thickness of Ni film as a parameter. (After Kondo and Moritani.[31]). . . 41

6. Polarization anisotropies of the Schottky-barrier ER spectra of Si in the energy range of E_0' and E_1 transitions. Data are taken on $(1\bar{1}0)$ face at 77 K in the low-field modulation limit. (After Kondo and Moritani.[31]). 45

7. Shottky-barrier ER spectra of Si for the E_0' and E_1 transitions under uniaxial (compression) stress along the [001] direction: (a) $T = -3.84 \times 10^9$ dyn/cm^2; (b) $T = -5.35 \times 10^9$ dyn/cm^2; (c) $T = -6.97 \times 10^9$ dyn/cm^2. $S_{IA\perp}$ (or $S_{IA\parallel}$), $S_{II\perp}$ (or $S_{II\parallel}$), etc., are the split-off structures of S_I and S_{II} under [001] stress with perpendicular (or parallel) polari-

FIGURE Page

zation. (After Kondo and Moritani.[31]) 48

8. Schottky-barrier ER spectra of Si for the E_0' and E_1 transitions under uniaxial (compression) stress along the [111] direction: (a) $T = -1.87 \times 10^9$ dyn/cm^2; (b) $T = -5.65 \times 10^9$ dyn/cm^2; (c) $T = -8.78 \times 10^9$ dyn/cm^2. $S_{Ia\perp}$, $S_{Ib\|}$, etc., are the split-off structures of S_I under [111] stress with perpendicular and parallel polarizations. (After Kondo and Moritani.[31]). 49

9. Stress dependences of the peak energies of the S_I structure. The energy positions of positive and negative peaks are plotted together. (a) $\vec{T} \parallel [001]$ and (b) $\vec{T} \parallel [111]$. Solid lines are obtained for $\hat{n} \perp \vec{T}$ and dashed lines for $\hat{n} \parallel \vec{T}$. (After Kondo and Moritani.[31]) 50

10. Uniaxial stress effects of the Λ_3^v valence and Λ_1^c conduction bands for stresses along the [001] and [111] directions. The relative strengths of the ER form factor F for $\hat{n} \parallel \vec{T}$ and $\hat{n} \perp \vec{T}$ configurations are given in the left side of the each arrow. Schematic diagram of the stress-induced energy shifts for the $\Lambda_3^v - \Lambda_1^c$ critical point is given in the right hand side 52

11. Amplitude changes of the positive peak of the S_I structure as a function of uniaxial stresses along (a) the [001] direction and (b) the [111] direction. Solid lines are obtained for $\hat{n} \perp \vec{T}$ and dashed lines for $\hat{n} \parallel \vec{T}$. (After Kondo and Moritani.[31]). 56

12. Stress dependences of the peak energies of the S_{II} structure. (a) $\vec{T} \parallel [001]$ and (b) $\vec{T} \parallel [111]$. Solid lines are obtained for $\hat{n} \perp \vec{T}$ and dashed lines for $\hat{n} \parallel \vec{T}$. (After Kondo and Moritani.[31]). 58

13. Amplitude changes of the positive peak of the S_{II} structure as a function of uniaxial stresses along (a) the [001] direction and (b) the [111] direction. Solid lines are obtained for $\hat{n} \perp \vec{T}$ and dashed lines for $\hat{n} \parallel \vec{T}$. (After Kondo and Moritani.[31]). 59

FIGURE Page

14. Schottky-barrier ER spectrum of Si in the energy range of E_2 transitions at 90 K. Open circles are experimental results, taken on $(1\bar{1}0)$ face in the low-field modulation limit. Line shapes obtained by a least-squares fit assuming the existence of (a) two and (b) three structures are also shown. Long-dashed, dotted, and short-dashed lines are the calculated three-dimentional line shapes for the $E_2(1)$, $E_2(2)$, and $E_2(3)$ structures, respectively. Solid line is the sum of the above (a) two or (b) three line shapes. (After Kondo and Moritani.[35]) 61

15. Seraphin coefficients of the air-Ni-Si three-phase system at 90 K, calculated from the reflectivity spectra of Ni and Si. The results are shown with the thickness of Ni film as a parameter. (After Kondo and Moritani.[35]). 62

16. Polarization anisotropy of the Schottky-barrier ER spectrum of Si in the energy range of E_2 transitions. Data are taken on $(1\bar{1}0)$ face at 77 K in the low-field modulation limit. Solid line is the spectrum for $\hat{n} \parallel [110]$ and dashed line for $\hat{n} \parallel [001]$. (After Kondo and Moritani.[35]). 66

17. The first Brillouin zone of diamond lattice showing the symmetry points and axes 71

18. The $E_{4-5}(\vec{k})$ energy contours of Si in the ΓKWX, ΓKL, and ΓXUL planes constructed from the experimental results (in eV). The critical points (c.p.) listed in this figure are as follows: E_0' : M_0^{3D} c.p. on the Δ axis near the Γ point ($\mu_T/\mu_L = 1-3$, $\mu_T > 0$, $\mu_L > 0$) or some c.p. set around the Γ point; E_1: M_1^{3D} c.p. at the L point ($\mu_T << |\mu_L|$, $\mu_T > 0$, $\mu_L < 0$); E_2: M_1^{3D} c.p. on the Σ axis ($1/\mu_{T2} + 1/\mu_L = 4/\mu_{T1}$, $\mu_{T1} > 0$, $\mu_{T2} < 0$, $\mu_L > 0$, in this case); and M_2^{3D} c.p. on the Δ axis near the X point ($|\mu_T| >> \mu_L$, $\mu_T < 0$, $\mu_L > 0$). (After Kondo and Moritani, Ref. 111). 72

19. The calculated $E_{4-5}(\vec{k})$ energy contours of Si in the ΓKL and ΓXUL planes. Asterisks indicate optical critical points. (After Kane.[47]) 82

FIGURE Page

20. The calculated $E_{4-5}(\vec{k})$ energy contours of Si in the ΓKWX, ΓKL, and ΓXUL planes. Open circles indicate optical critical points. (After Saravia and Brust.[49]) 82

21. Schematic diagram of a three-phase optical system. The complex refractive indices of the phases are denoted by N_0, N_1, and N_2. 89

I. INTRODUCTION

A useful technique for studying the energy band structures of crystals is to look for optical critical points,[1,2] where the gradient of the interband energy vanishes in the Brillouin zone, and to analyze their essential features, i.e., critical-point energies, symmetry locations, and interband-reduced masses. The information of these critical points, together with appropriate smooth curves connecting them, will give a good approximation to the exact interband-energy contours.[2,3] Moreover, knowledge of optical critical points and the interband energy contours is prerequisite to interprete the optical properties of crystals in the energy range above the fundamental absorption edge.

Since the introduction of electroreflectance (ER) technique by Seraphin,[4–6] various types of modulation methods,[7,8] such as piezoreflectance,[9–12] thermoreflectance,[13–15] and wavelength-modulated reflectance,[16–18] have been developed and applied to analyze the optical-critical-point structures of crystals. The power of these methods lies in the fact that modulation techniques enhance the signals at critical points in the Brillouin zone. In recent years, it has been shown by Aspnes[19–23] that the low-field ER technique is suitable for the precise study of optical-critical-point structures. The advantages of low-field ER are as follows:

(i) Low-field ER spectra give the strongly enhanced critical-point structures with strongly suppressed background effects, since they are described by the third-derivative of the unperturbed dielectric function $\epsilon(\hbar\omega)$.[21,23]

(ii) Low-field ER spectra simply scale quadratically in the applied field and the line shapes are invarient to changes in the field.[19,23] Therefore, low-field ER spectra modulated in the surface space charge

region are proportional to the surface potential, which is used to find the low-field modulation limit experimentally.[22,23]

(iii) These linearlized spectra are rigorously independent of dc bias and modulation waveform when they are detected by a phase sensitive system.[22,23]

(iv) Quantitative ER spectra can be obtained in the low-field modulation limit without the need for modulation from the flat band.[22]

Thus, the most accurate values of the optical-critical-point parameters are obtained from low-field ER spectra.[20,23] The polarization dependences of (low-field) ER spectra give in principle the symmetry properties of nondegenerate[24-27] and degenerate[26,28-31] critical points. Moreover, it is clear that the symmetry-breaking perturbation of uniaxial stress is useful for the symmetry analysis.[32,33] Deformation potential parameters can also be obtained from the uniaxial stress effects.

We use the Schottky-barrier[34] configuration for our ER measurements. It is ideal for low-field ER experiments,[29] because (i) Schottky diodes are easy to control the surface potential in a fully depleted space-charge region, (ii) they are majority-carrier devices relatively insensitive to surface states, and (iii) they permit ER measurements to be made over wide ranges of temperature and wavelength. In addition, this technique is advantageous for applying static uniaxial stress, because the evaporated metal on a semiconducting surface may remain in uniform contact with it when the sample is elastically deformed by the stress.

It is the purpose of this paper to describe a method of precise analysis on optical-critical-point structures by low-field ER and apply it to Si,[31,35] which is a widely used semiconducting material. In this paper, we shall concentrate on the E_0', E_1, and E_2 optical structures

of Si in the energy range between 3.0 and 5.0 eV.

The E_0' and E_1 optical structures (3.0 — 4.0 eV) have been the subject of controversy for a long time. A number of experimental and theoretical investigations have been made in this energy region. From the experimental point of view, reflectivity measurements on Ge - Si alloys,[36] dc piezoreflectivity measurements,[33] ac piezoreflectance,[10] wavelength-modulated reflectance,[17] and uniaxial-stress effects on the wavelength-modulated spectra[37,38] have been performed. As for the ER measurements of Si, the pioneering work has been made by Seraphin[39,40] in the MIS (metal-insulator-semiconductor) configuration; later works have followed in the electrolyte[41—43] and in the transverse-electric-field[44] configurations. Schmidt and Vedam[45] have measured the hydrostatic-pressure effects of the Ge - Si alloys using the MIS-ER technique. The uniaxial stress effects on the ER spectra of Ge, GaAs, and Si have been measured by Pollak and Cardona,[46] for the first time, though their analysis was insufficient in the sense that the measured ER spectra were out of the low-field conditions and the quantitative comparison with the ER theory[19] was unsatisfactory. Most of the experimental results suggest equally except for details that the 3.4 eV structures arise from at least two distinct critical points with different symmetries. On the other hand, the existence of an extremely complex nest of critical points in this energy region has been predicted by detailed energy-band-structure calculations.[47—50] Kane[47] has pointed out that the energy gaps at Γ, X, and L are very close in energy in this region and *critical points along the Δ line* give a dominant contribution to the 3.4 eV structures. Saravia and Brust[49] have shown that the 3.4 eV structures come mainly from two regions near the Γ point and *the Λ line (including the L point)*. To be short, the above experimental and theoretical evidences may be

divided into two parts for the symmetry assignment of the dominant critical point in this energy region: the $\Lambda_3^v \to \Lambda_1^c$ (or $L_{3'}^v \to L_1^c$) transition[17,31,32,38,45,48,51–53] and $\Delta_5^v \to \Delta_1^c$ transition near the Γ point (including the $\Gamma_{25'}^v \to \Gamma_{15}^c$ transition).[3,10,16,33,36,37,46,47,54–60]

The existence of a cluster of critical points in the E_2 spectral region (4.0 – 5.0 eV) has been predicted by Brust,[3] Cardona and Pollak,[60] Kane,[47] and Saravia and Brust[49] in their band-structure calculations. Especially, Kane[47] and Saravia and Brust[49] have shown that the E_2 peak in the imaginary part of the dielectric function, $\epsilon_2(\hbar\omega)$, originates from the large region in the Brillouin zone and not from the high symmetry points or axes. On the other hand, two structures have been observed experimentally in the modulated-reflectivity spectra, such as ER,[41,42] thermoreflectance,[15] and wavelength-modulated-reflectance;[16,17] and the critical points related to these structures have been attributed to the $X_4^v \to X_1^c$ and $\Sigma_2^v \to \Sigma_3^c$ transitions. The assignment, however, may be tentative because it depends largely on the results of the existing energy-band-structure calculations.[3,47,49,52,60]

The outline of this paper is as follows: Theoretical background is given in Sec. II. In Sec. II A, the optical properties of crystals, especially the interactions between the propagating photon field and electrons in crystals, are described in terms of the optical dielectric function. The concept of optical-critical point is explained in connection with the dielectric function. In addition, the topological types and symmetry properties of critical points are presented. The theoretical concept and the general expressions of low-field ER are explained in Sec. II B. In Sec. II C, a method of symmetry analysis by low-field ER is presented. Uniaxial stress effects on low-field ER spectra are described in Sec. II D.

In Secs. III A and III B, experimental details of sample preparation, measurement techniques, and stress arrangement are discussed.

The data for the E_0' and E_1 structures are presented and analyzed in Sec. IV A and the data for the E_2 structures in Sec. IV B.

Section V shows a synthesis of the optical-critical points analyzed in Sec. IV: A method of synthesis is explained and the interband energy contours of Si are constructed from the experimental results.

In Sec. VI, the results obtained in Secs. IV and V are discussed and compared to other experimental and calculated results.

The conclusions obtained in this paper are summarized in Sec. VII.

The Seraphin coefficients for the three-phase optical system are given in Appendix A. Appendix B shows the theoretical basis for measuring doping inhomogeneity on semiconductor surfaces by the low-field ER technique.

II. THEORY

A. Optical Dielectric Function and Critical Point

a. *Optical Dielectric Function*

We first consider the interaction of light with solid in order to explain the optical dielectric function. An electromagnetic wave propagating in an isotropic and homogeneous solid can be described by its electric field $\vec{\mathcal{E}}$. When the solid is electrically neutral with no external current flow, the electric field induces a microscopic current $\vec{j}(\vec{r}, t)$, which gives rise to a polarization $\vec{p}(\vec{r}, t)$ of the microscopic charge distribution. Since we consider the wavelength of the electromagnetic wave to be much larger than the atomic dimensions of the solid, it is convenient to perform local averages of $\vec{j}(\vec{r}, t)$ and $\vec{p}(\vec{r}, t)$. For sufficiently weak fields, the Fourier transform of an average displacement $\vec{D}$ of the system is defined by

$$\vec{D}(\hbar\omega) = \vec{\mathcal{E}}(\hbar\omega) + 4\pi \langle \vec{p}(\hbar\omega) \rangle, \tag{1}$$

$$\equiv \epsilon(\hbar\omega) \cdot \vec{\mathcal{E}}(\hbar\omega). \tag{2}$$

The tensor $\epsilon(\hbar\omega)$ in Eq. (2) is defined to be the optical dielectric function. Because of time reversal, $\epsilon(\hbar\omega)$ is always a symmetric tensor, $\epsilon_{ij} = \epsilon_{ji}$, in the absence of external magnetic fields.[61] The importance of the dielectric function is that it completely describes the interaction of an electromagnetic wave with elementally excitations in the solid on macroscopic scale.[62]

The photon field with sufficient energy interacts strongly with electrons in crystals. The field excites electron from the filled states to an empty state and makes an electron-hole pair. Considering an electron-hole pair band " t ", whose wave vector is represented by $\vec{K}_0$ in the Brillouin zone, and ignoring the small wave vector of the light,

we can describe the pair state by a two-particle function[63]

$$\psi_{j\alpha}^{t}(\vec{r}_1, \vec{r}_2) = \sum_{j1} a_{j1}^{t} \sum_{\alpha 1, \alpha 2} \gamma_{j1\alpha 1, j2\alpha 2; j\alpha} \mathcal{F}_{j1\alpha 1}^{t}(\vec{r}_1 - \vec{r}_2)\, U_{j2\alpha 2}(\vec{r}_1, \vec{r}_2), \quad (3)$$

where the coordinate $\vec{r}_1$ and $\vec{r}_2$ refer to the electron and hole, the factor " a " is the normalization constant, and γ is the unitary Clebsch-Gordan matrix.[64] Some useful γ matrices are tabulated by Koster et al.[65] for the thirty-two point groups. $\mathcal{F}$ and U in Eq. (3) are the envelope and the Bloch parts of the pair state function. The subscript j, j1, j2 of ψ, $\mathcal{F}$, U denote the irreducible representations of the group of $\vec{K}_0$ and the symbols α, $\alpha 1$, $\alpha 2$ label the partner functions of j, j1, j2.

The irreducible pair band $U_{j\alpha}$ consists of the product of one-electron Bloch function $u_{j\alpha}(\vec{r})\exp(i\vec{K}_0 \cdot \vec{r})$ as[63]

$$U_{j\alpha}(\vec{r}_1, \vec{r}_2) = \sum_{\alpha 1, \alpha 2} \gamma_{j1\alpha 1, (j2\alpha 2)^*; j\alpha}\, u_{j1\alpha 1}(\vec{r}_1)\, u_{j2\alpha 2}^{\dagger}(\vec{r}_2) \times \exp[i\vec{K}_0 \cdot (\vec{r}_1 - \vec{r}_2)]. \quad (4)$$

Here we take the usual "one-electron" view so the hole wave function is the adjoint ($\dagger$) of the corresponding one-electron wave function.

The functional form of the envelope part $\mathcal{F}_{j\alpha}$ and the normalization constant " a " can be found from the solution of the effective-mass equation, using the effective Hamiltonian[63,66]

$$H = E^t + H_{KE}, \quad (5)$$

where

$$E^t \equiv E_{c,t}(\vec{K}_0) - E_{v,t}(\vec{K}_0), \quad (6)$$

$$H_{KE} = \sum_{s,j,\alpha} (W_{j\alpha}^{s})^{*} \tilde{\gamma}_{j\alpha} R_j^{s}, \quad (7)$$

$$\langle j1\alpha 1 | \tilde{\gamma}_{j\alpha} | j2\alpha 2 \rangle \equiv \sqrt{n}\, \gamma_{j1\alpha 1, (j2\alpha 2)^*; j\alpha}. \quad (8)$$

Here the Coulomb interaction is neglected. E^t is the interband energy at $\vec{K}_0$. The kinetic-energy operator H_{KE} acts only on $\mathcal{G}$ and can be written in the irreducible form shown in Eq. (7), where an operator W is quadratic in the crystal momentum operator $\vec{p}$ and its irreducible form $W_{j\alpha}^{s}$ is constructed from $W_{ij} = p_i p_j/2$ under the group of $\vec{K}_0$. R_j^s is a reciprocal reduced-mass parameter. Equation (7) is also applicable to the degenerate bands due to the term $\tilde{\gamma}_{j\alpha}$.

We wish to discuss the optical-matrix element of the momentum operator. The electron-photon interaction operator H_{opt} can be written in an irreducible form[63]

$$H_{opt} = \frac{e}{mc} \sum_{j,\alpha} A_{j\alpha}^{*} p_{j\alpha} , \tag{9}$$

where $\vec{A}$ is the vector potential. Following Elliott[67] and Kane,[63] the optical-matrix element $P_{j\alpha}^{t}$ between the ground state $|0\rangle$ and the excited state $|\psi_{j\alpha}^{t}\rangle$ can be written

$$P_{j\alpha}^{t} \equiv \langle 0|p_{j\alpha}|\psi_{j'\alpha'}^{t}(\vec{r}_1, \vec{r}_2)\rangle , \tag{10}$$

$$= a_1^t \mathcal{G}_1^t(0) \sqrt{V} \langle 0|p_{j\alpha}|U_{j\alpha}(\vec{r}, \vec{r})\rangle \delta_{jj'} \delta_{\alpha\alpha'} , \tag{11}$$

where V is the crystal volume, $\mathcal{G}_1(0)$ is the envelope function evaluated at the origin, $\vec{r}_1 = \vec{r}_2 = \vec{r}$. It is very important that only the envelope function with identity symmetry, $\mathcal{G}_1(0)$, is involved in Eq. (11); therefore, the selection rules of the optical transition can be determined by the pair band $U_{j\alpha}(\vec{r}, \vec{r})$.

On the basis of the above arguments, the optical dielectric tensor for nondegenerate electron-hole pairs can be written[68]

$$\epsilon_{ij}(\hbar\omega + i\Gamma) = 1 + \sum_{t}\sum_{\vec{K}_0} \epsilon_{ij}^{t}(\hbar\omega + i\Gamma, \vec{K}_0) , \tag{12a}$$

$$= 1 + \sum_{t} \epsilon_{ij}^{t}(\hbar\omega + i\Gamma) , \tag{12b}$$

where for a single electron-hole pair band " t "

$$\epsilon_{ij}^{t}(\hbar\omega + i\Gamma) = - \frac{e^2\hbar^2}{\pi^2 m^2 (\hbar\omega + i\Gamma)^2} \int_{BZ} \frac{P_i^t(\vec{k})\, P_j^t(\vec{k})}{\hbar\omega + i\Gamma - E^t(\vec{k})} d^3k, \tag{13}$$

$$E^t(\vec{k}) = E_{c,t}(\vec{k}) - E_{v,t}(\vec{k}). \tag{14}$$

Here, $\hbar\omega$ is the photon energy, Γ is the phenomenological broadening energy (phenomenological life time parameter $\tau \sim \hbar/\Gamma$), and $E^t(\vec{k})$ is the $\vec{k}$ dependence of the single electron-hole pair-band (interband) energy.

b. Optical Critical Point

As shown in Eqs. (12) through (14), the dielectric function $\epsilon(\hbar\omega + i\Gamma)$ is mainly determined by the $\vec{k}$ dependences of the interband energy $E^t(\vec{k})$; and it is closely related with certain points in the Brillouin zone, called "critical points", where the gradient of the interband energy vanishes. We will show this point clearly. We first transform Eq. (13) from a volume integration in $\vec{k}$ space to a surface integration using the coordinate transformation

$$d^3k = \frac{dE^t dS^t}{|\nabla_{\vec{k}} E^t(\vec{k})|}, \tag{15}$$

where dS^t represents an element area of the constant interband energy surface $E^t(\vec{k}) = E^t$ in $\vec{k}$ space and dE^t is the energy increment in that space. The result is

$$\epsilon_{ij}^{t}(\hbar\omega + i\Gamma) = - \frac{e^2\hbar^2}{\pi^2 m^2 (\hbar\omega + i\Gamma)^2} \int_{S^t} \frac{P_i^t P_j^t dS^t}{|\nabla_{\vec{k}} E^t(\vec{k})|} \int_0^{\infty} \frac{dE^t}{\hbar\omega + i\Gamma - E^t}. \tag{16}$$

Using the relation

$$\delta(x - x_0) = \frac{1}{\pi} \lim_{\rho \to 0} \frac{\rho}{(x - x_0)^2 + \rho^2}, \tag{17}$$

the imaginary part $\epsilon_{2,ij}{}^{t}$ of the optical dielectric function may be written in the limit of $\Gamma \to 0$ as

$$\epsilon_{2,ij}{}^{t}(\hbar\omega) = \lim_{\Gamma \to 0} \mathrm{Im}\left\{\epsilon_{ij}{}^{t}(\hbar\omega + i\Gamma)\right\} , \tag{18}$$

$$= -\frac{e^2}{\pi m^2 \omega^2}\int_{S^t} \frac{P_i{}^t P_j{}^t \, dS^t}{|\nabla_{\vec{k}} E^t(\vec{k})|}\int_0^{\infty} \delta(\hbar\omega - E^t)\, dE^t, \tag{19}$$

$$= -\frac{e^2}{\pi m^2 \omega^2}\int_{S^t} \frac{P_i{}^t P_j{}^t \, dS^t}{|\nabla_{\vec{k}} E^t(\vec{k})|}\Bigg|_{\hbar\omega = E^t} . \tag{20}$$

Then, the singularities may occur where the gradient of the interband energy vanishes, i.e., when $\nabla_{\vec{k}} E^t(\vec{k}) = 0$ at $\hbar\omega = E^t$. This type of singularities are called the Van Hove singularities.[1] We assume here that critical points belong to the single electron-hole pair band are independent of each other because of the lifetime broadening effects. Then, the topological properties of the pair band (interband) energy $E^t(\vec{k})$ in the vicinity of a critical point "τ" at $\vec{K}_0$ in the Brillouin zone can be explicitly written in a Taylor series

$$E^{\tau}(\vec{k}) = E_g{}^{\tau} + \frac{1}{2}\sum_{i,j} \frac{\partial^2 E^t(\vec{k})}{\partial k_i \, \partial k_j}\Bigg|_{\vec{k} = \vec{K}_0} (k_i - K_{0,i})(k_j - K_{0,j}) + \cdot \cdot \cdot , \tag{21}$$

where the summation indices i, j represent the coordinate axes x, y, z. We neglect the terms higher than triplet in Eq. (21) in the parabolic approximation. For nondegenerate critical points, Eq. (21) can be rewritten in the coordinate in which the quadratic term is diagonalized

$$E^{\tau}(\vec{k}) = E_g{}^{\tau} + \frac{\hbar^2}{2}\left[\frac{(k_{T1} - K_{0,T1})^2}{\mu_{T1}} + \frac{(k_{T2} - K_{0,T2})^2}{\mu_{T2}} + \frac{(k_L - K_{0,L})^2}{\mu_L} \right], \tag{22}$$

where the longitudinal axis L is defined to be parallel to the representative vector $\vec{K}_0$ of the critical point. μ_{T1}, μ_{T2}, and μ_L are the diagonal components of the second-rank interband reduced-mass tensor, which is defined as

$$\frac{1}{\mu_i} = \frac{1}{\hbar^2} \frac{\partial^2}{\partial k_i^{\,2}} E^t(\vec{k}). \tag{23}$$

The relation between the interband reduced-mass tensors, μ_i and R_j^s (defined in Eq. (7)), can be calculated for some specific cases.[69a] For degenerate critical points, we neglect the warping effect[69b] of the interband energy surfaces,in addition to the parabolic approximation, which is equal to neglecting the non-diagonal terms of the kinetic energy Hamiltonian in Eq. (7). These simple parabolic models of the effective-mass approximation enable us to treat the transition between degenerate bands as the sum of transitions between nondegenerate bands.[31] This assumption may be accepted only in the case of optical transitions with large broadening energy.

Critical points are characterized by four distinct combinations of signes of the masses: The critical point is said to be of type M_ℓ ($\ell = 0, 1, 2, 3$) when ℓ-number of the principal reduced-masses μ_{T1}, μ_{T2}, and μ_L are negative. Then, the types are as follows:

$$\begin{aligned}
M_0 &: \quad \mu_{T1} > 0,\ \mu_{T2} > 0,\ \mu_L > 0,\\
M_1 &: \quad \mu_{T1} > 0,\ \mu_{T2} > 0,\ \mu_L < 0,\\
M_2 &: \quad \mu_{T1} < 0,\ \mu_{T2} < 0,\ \mu_L > 0,\\
M_3 &: \quad \mu_{T1} < 0,\ \mu_{T2} < 0,\ \mu_L < 0.
\end{aligned} \tag{24}$$

We wish to discuss the symmetry characters of critical points. Since we consider only the excited states which couple strongly to light (see Eq. (11)), the critical points at $\vec{K}_0$ may be represented by the irreducible pair states $U_{j\alpha}$ which transform in the same way as the irreducible components of the momentum operator $p_{j\alpha}$ under the group of $\vec{K}_0$. For example, we show in Table I the symmetry characters of critical

TABLE I. Symmetry properties for Γ, Δ, Λ, L, and Σ critical points in diamond-type crystals.

Critical point location	Pair state symmetry	Basis function	$\hat{B}_{\gamma\alpha}$
Γ ; O_h (m3m)	U_{4-}	x	; $\hat{B}_{4T1} = (1, 0, 0)$
		y	; $\hat{B}_{4T2} = (0, 1, 0)$
		z	; $\hat{B}_{4L} = (0, 0, 1)$
Δ ; C_{4v} (4mm)	U_1	z	; $\hat{B}_1 = (0, 0, 1)$
	U_5	x	; $\hat{B}_{5T1} = (1, 0, 0)$
		y	; $\hat{B}_{5T2} = (0, 1, 0)$
Λ ; C_{3v} (3m)	U_1	$(x+y+z)/\sqrt{3}$	; $\hat{B}_1 = (\frac{1}{\sqrt{3}})(1, 1, 1)$
	U_3	$(x-y)/\sqrt{2}$	; $\hat{B}_{3T1} = (\frac{1}{\sqrt{2}})(1, -1, 0)$
		$(x+y-2z)/\sqrt{6}$	; $\hat{B}_{3T2} = (\frac{1}{\sqrt{6}})(1, 1, -2)$
L ; D_{3d}	U_{2-}	$(x+y+z)/\sqrt{3}$	; $\hat{B}_2 = (\frac{1}{\sqrt{3}})(1, 1, 1)$
	U_{3-}	$(x-y)/\sqrt{2}$	; $\hat{B}_{3T1} = (\frac{1}{\sqrt{2}})(1, -1, 0)$
		$(x+y-2z)/\sqrt{6}$	; $\hat{B}_{3T2} = (\frac{1}{\sqrt{6}})(1, 1, -2)$
Σ ; C_{2v} (mm2)	U_1	$(x+y)/\sqrt{2}$	; $\hat{B}_1 = (\frac{1}{\sqrt{2}})(1, 1, 0)$
	U_2	z	; $\hat{B}_2 = (0, 0, 1)$
	U_3	$(x-y)/\sqrt{2}$	; $\hat{B}_3 = (\frac{1}{\sqrt{2}})(1, -1, 0)$

points at $\vec{K}_0 = (0, 0, 0) : \Gamma$, $(\frac{2\pi}{a})(0, 0, k_0) : \Delta$, $(\frac{2\pi}{a})(k_0, k_0, k_0) : \Lambda$, $(\frac{2\pi}{a})(1, 1, 1) : L$, and $(\frac{2\pi}{a})(k_0, k_0, 0) : \Sigma$ in diamond-type crystals. In Table I, $\hat{B}_{\gamma\alpha}$ is the unit vector transforming in the same way as the basis function.

B. Low-Field Electroreflectance

The electric-field effects in crystals were first treated by Franz[70] and Keldysh.[71] The general formula of the electric-field effects on the dielectric function have been derived and summarized by Aspnes in the series of papers.[72–75]

When an electric field is applied to a crystal, basically two different effects occur: the relative positions of the atoms in the crystal lattice shift, and the electron-hole pair state functions in the crystal become distorted. The first effect is weak in most crystals except for ferroelectric crystals and, then, we consider the second effects only.

The effective Hamiltonian for electron-hole states in the presence of uniform electric field can be written as

$$H = E_g^{\tau} + H_{KE} + H_{EL}, \tag{25}$$

where

$$H_{EL} = - e\, \vec{\mathcal{E}} \cdot (\vec{r}_1 - \vec{r}_2). \tag{26}$$

The Hamiltonian is therefore no longer invarient to lattice translations in the direction of the field depending on the potential energy term H_{EL} which varies linearly in position. The electron and hole accelerate and their quasi-continuous wave vectors $\vec{k}_1$ and $\vec{k}_2$ will be mixed in the field direction as[74,75]

$$\vec{k}_1(t) = \vec{k}_1(0) - \frac{e\vec{\mathcal{E}}t}{\hbar}, \tag{27}$$

$$\vec{k}_2(t) = \vec{k}_2(0) + \frac{e\vec{\mathcal{E}}t}{\hbar}, \tag{28}$$

where t is an independent variable. Consequently, the pair state wave functions of the unperturbed crystal become mixed. This is equivalent to spreading the formerly sharp vertical transitions over a finite range of initial and final momenta, as shown in Fig. 1.[76] If the field is sufficiently small and the phenomenological broadening energy of the state is reletively large, the accelerated electrons and holes may be immediately scattered or recombined; and, then, the mixing of the wave functions will be restricted to those near the originally vertical allowed transition. This will smear out structure in the unperturbed dielectric function, yielding a complicated difference spectrum as indicated in Fig. 1.

Following Aspnes,[19] the optical dielectric function can be written in the presence of sufficiently low fields

$$\epsilon_{ij}^{\tau}(\hbar\omega + i\Gamma, \vec{\mathcal{E}}) = \epsilon_{ij}^{\tau}(\hbar\omega + i\Gamma) + \Delta\epsilon_{ij}^{\tau}(\hbar\omega + i\Gamma, \vec{\mathcal{E}}), \tag{29}$$

where

$$\Delta\epsilon_{ij}^{\tau}(\hbar\omega + i\Gamma, \vec{\mathcal{E}}) = \frac{e^2\hbar^2}{\pi^2 m^2 (\hbar\omega + i\Gamma)^2} \int_{BZ} \frac{2(\hbar\Omega)^3 P_i^{\tau}(\vec{k}) P_j^{\tau}(\vec{k})}{[\hbar\omega + i\Gamma - E^{\tau}(\vec{k})]^4} d^3k, \tag{30}$$

$$(\hbar\Omega)^3 = \frac{e^2}{8}(\vec{\mathcal{E}} \cdot \nabla_{\vec{k}})^2 E^{\tau}(\vec{k}). \tag{31}$$

The equation (30) will be valid only in the case of $|\hbar\Omega| \leqq \frac{\Gamma}{3}$, which is the low-field modulation limit. When we assume that the momentum matrix element is $\vec{k}$ independent in the vicinity of a critical point and the $\vec{k}$ dependence of the interband energy is written in the parabolic form shown in Eq. (22), the integral in Eq. (30) can be extended to infinity in all three dimensions, and we obtain the three-dimensional low-field line shape[19, 23]

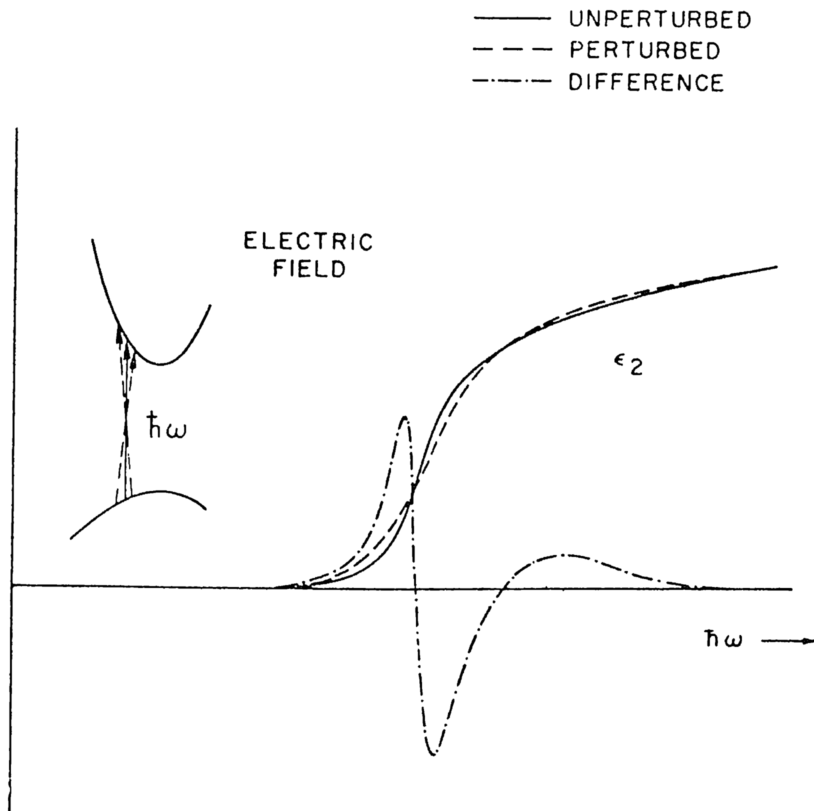

FIG. 1. Schematic diagram of electric field modulation process where the lattice periodicity is destroyed. The effect of the perturbation on the energy band structure and optical transition is shown at the left. (After Aspnes.[76])

$$\Delta \epsilon_{ij}{}^{\tau}(\hbar\omega + i\Gamma, \vec{\mathcal{E}}) = \frac{e^4\hbar^4}{4\pi^2 m^2}\frac{\pi^2}{8}\left|\frac{8\mu_{T1}\mu_{T2}\mu_L}{\hbar^6}\right|^{\frac{1}{2}} i^{\ell-3} (\hbar\omega + i\Gamma)^{-2} (\hbar\omega + i\Gamma - E_g{}^{\tau})^{-\frac{5}{2}}$$

$$\times P_i{}^{\tau} P_j{}^{\tau} \left(\frac{(\mathcal{E}_{T1})^2}{\mu_{T1}} + \frac{(\mathcal{E}_{T2})^2}{\mu_{T2}} + \frac{(\mathcal{E}_L)^2}{\mu_L}\right) \mathcal{E}^2, \quad (32)$$

where $\mathcal{E}_{T1}$, $\mathcal{E}_{T2}$, and $\mathcal{E}_L$ are the three principal components of the unit vector $\hat{\mathcal{E}}$ in the electric field direction. ℓ is the number of negative reduced masses at a critical point.

General expression relating the field-induced change $\Delta\epsilon$ in the dielectric function to the relative reflectivity change $\Delta R/R$ can be given[23]

$$\frac{\Delta R}{R}(\hbar\omega, \Gamma) = \mathrm{Re}\left\{ \tilde{C}\,[\alpha(\hbar\omega) - i\beta(\hbar\omega)] \sum_{\tau}\sum_{i,j} n_i n_j \, \Delta\epsilon_{ij}{}^{\tau}(\hbar\omega + i\Gamma, \vec{\mathcal{E}})\right\}, \quad (33)$$

where $\hat{n}$ is the unit polarization vector of the incident radiation. The quantity $\tilde{C}$ is a product of complex functions which represent the effect of a nonuniform modulating field,[77]

$$\tilde{C}_{in} = -i\frac{2\omega}{c}(n + ik)\int_{-\infty}^{0} dz\, [\mathcal{E}(z)/\mathcal{E}(0)]^2 \exp[-i\frac{2\omega}{c}(n + ik)z], \quad (34)$$

and the electron-hole effect in the contact-exciton approximation,[78]

$$\tilde{C}_{ex} = [1 + g(\epsilon(\hbar\omega) - 1)]^{-2}; \qquad g \leq 0, \quad (35)$$

where g is the strength parameter, which can be assumed to be constant for a given structure. The function $\alpha(\hbar\omega) - i\beta(\hbar\omega)$ is the complex Seraphin coefficient.[79] By substituting Eq. (32) into Eq. (33), we obtain

$$\frac{\Delta R}{R}(\hbar\omega, \Gamma) = \mathrm{Re}\left\{\tilde{C}\,[\alpha(\hbar\omega) - i\beta(\hbar\omega)] \sum_{\tau} i^{\ell-3} L^{\tau}(\hbar\omega + i\Gamma)\right\} F^{\tau} \mathcal{E}^2, \quad (36)$$

where the line shape part L is[19,23]

$$L^{\tau}(\hbar\omega + i\Gamma) = \frac{e^4\hbar^4}{4\pi^2 m^2}\frac{\pi^2}{8}\left|\frac{8\mu_{T1}\mu_{T2}\mu_L}{\hbar^6}\right|^{\frac{1}{2}} (\hbar\omega + i\Gamma)^{-2} (\hbar\omega + i\Gamma - E_g{}^{\tau})^{-\frac{5}{2}}, \quad (37)$$

and the symmetry part F may be written[31]

$$F^{\tau} = \sum_{\nu,\alpha} (\hat{n}^{\nu}\cdot\hat{B}_{\gamma\alpha})^2 \left(\frac{(\mathcal{E}^{\nu}_{T1})^2}{\mu_{T1}} + \frac{(\mathcal{E}^{\nu}_{T2})^2}{\mu_{T2}} + \frac{(\mathcal{E}^{\nu}_{L})^2}{\mu_{L}}\right) f^0, \quad (38)$$

$$f^0 \equiv \langle 0|p_{\gamma\alpha}|\psi_{\gamma\alpha}{}^{\tau}\rangle^2, \quad (39)$$

here, $\hat{B}_{\gamma\alpha}$ is the unit vector transforming in the same way as the pair state $\psi_{\gamma\alpha}$ with symmetry U_{γ} under the group of $\vec{K}_0$. $\sum_{\alpha}$ represents the sum over the order of degeneracy of a critical point and $\sum_{\nu}$ represents the sum over all the equivalent critical-point set, in which the superscript ν of $\hat{n}$ and $\hat{\mathcal{E}}$ shows that it is the effective component at the ν-th equivalent critical point.

The function $i^{\ell-3} L^{\tau}(\hbar\omega + i\Gamma)$ mainly determines the line shape of ER spectra and we can use Eq. (37) for determining the energy E_g, the phenomenological broadening parameter Γ, and the type M_{ℓ} of the critical point. The symmetry part represents the effects of the polarization of the light and the applied electric field on low-field ER spectra. We can use this anisotropy factor for determining the location $\vec{K}_0$ and the reduced-mass relation at critical point,[31] which will be described in Sec. II C.

C. Symmetry Analysis by Low-Field Electroreflectance

A theoretical basis for symmetry analysis using ER has been reviewed by Seraphin[79] and later by Rehn.[27] In this section, we describe a new method of symmetry analysis by low-field ER and apply it to diamond-type crystals.[31]

At sufficiently low fields, ER spectra can be factored into line-shape and symmetry parts as shown in Eq. (36). The symmetry location $\vec{K}_0$ of a critical point may be deduced from the combination of the polarization anisotropy and the line shape of the low-field ER spectrum. The

relation among the interband-reduced masses at the critical point may also be obtained from the analysis.

We wish to calculate the polarization dependences of low-field ER spectra using Eq. (38) and show the criteria of symmetry analysis for high symmetry critical points in diamond-type crystals. We will consider only a longitudinal ER geometry in order to analyze the Schottky-barrier ER spectra, where the directions of the incident light and the modulation field are normal to the plane of reflection. Moreover, we will choose the $(1\bar{1}0)$ face for the plane of reflection, since this surface includes all the four high-symmetry directions ([001], $[11\bar{2}]$, [111], and [110]) obtained for diamond-type crystals.[29] Thus the unit vectors of the applied electric field $\hat{\mathcal{E}}$ and the polarization of the incident light $\hat{n}$ are

$$\hat{\mathcal{E}} = (\frac{1}{\sqrt{2}}, -\frac{1}{\sqrt{2}}, 0) , \tag{40}$$

and

$$\hat{n} = (\frac{\sin\theta}{\sqrt{2}}, \frac{\sin\theta}{\sqrt{2}}, \cos\theta) , \tag{41}$$

respectively. When we neglect the effect of the spin-orbit interaction, the unit vectors $\hat{B}_{\gamma\alpha}$ for high symmetry $\Gamma(O_h)$, $\Delta(C_{4v})$, $\Lambda(C_{3v})$, $L(D_{3d})$, and $\Sigma(C_{2v})$ critical points in diamond-type crystals can be easily obtained from the Koster's table,[65] which are listed in Table I.
Since the interband reduced masses μ_{T1}, μ_{T2}, and μ_L are the diagonal components of the second-rank tensor, $\mu_{T1} = \mu_{T2} = \mu_L \equiv \mu$ (spherical symmetry) for the Γ critical point and $\mu_{T1} = \mu_{T2} \equiv \mu_T$ (local rotational symmetry) for the Δ, Λ, and L critical points.[61] Next, we sum over the star of $\vec{K}_0$ for Δ, Λ, L, and Σ critical points by summing over the effective components of $\hat{n}^\nu$ and $\hat{\mathcal{E}}^\nu$ in Eq. (38). Let g^ν be a minimal set of symmetry operators of the crystal point group which generates the star of $\vec{K}_0$,[63]

$$g^{\nu}\vec{K}_0 = \vec{K}_0^{\nu}\,. \tag{42}$$

Thus effective irreducible components of the vector potential for points in the star of $\vec{K}_0$ can be given

$$\vec{A}^{\nu} = (g^{\nu})^{-1}\,\vec{A}\,. \tag{43}$$

We present the apparent components of $\vec{A}$ in Table II, where we consider only the half part of the minimal set, since the dielectric function is bilinear in $\vec{A}$ and, then, $\vec{K}_0$ and $-\vec{K}_0$ are equivalent.

The calculated results for the polarization dependences of the ER form factor on the $(1\bar{1}0)$ face are listed in Table III. In Table III, we also list conditions on the polarization anisotropy $r \equiv F_{[001]}/F_{[110]}$ (or $s \equiv F_{[111]}/F_{[11\bar{2}]}$) for the four types of critical point, which can be used as criteria of symmetry analysis combined with the type of critical point determined from the line shape analysis.

In the case that the effect of the spin-orbit interaction is large compared to the lifetime broadening effect, the polarization dependences of the low-field ER spectra for the two split-off critical points can be easily calculated. The results are the same as listed in Table III for each of the two split-off structures.

This method of symmetry analysis, however, cannot lead us to the unique conclusion in some cases, since the criteria for some critical points are not exclusive of each other, as seen in Table III. We can get rid of this difficulty with help of the results of band structure calculations. Moreover, the three-dimensional ER line shapes of $M_{1\perp}$ and $M_{1\parallel}$, or $M_{2\perp}$ and $M_{2\parallel}$ critical points[80] may not be distinguished from each other in the low-field modulation limit or in the large broadening region. It may be useful to measure ER spectra in the Franz-Keldysh (or Airy convolution) range[23,74] in order to determine the critical point types correctly.

TABLE II. Effective components of the vector potential for the star of $\vec{K}_0 = (0, 0, k_0)$, (k_0, k_0, k_0), and $(k_0, k_0, 0)$ in diamond-type crystals. The effective components are primed and the actual components are unprimed. (After Kane.[63])

Δ critical point

	$(0, 0, k_0)$	$(0, k_0, 0)$	$(k_0, 0, 0)$
A_x'	A_x	A_z	A_y
A_y'	A_y	A_x	A_z
A_z'	A_z	A_y	A_x

Λ or L critical point

	(k_0, k_0, k_0)	$(k_0, \bar{k}_0, \bar{k}_0)$	$(\bar{k}_0, k_0, \bar{k}_0)$	$(\bar{k}_0, \bar{k}_0, k_0)$
A_x'	A_x	A_x	$-A_x$	$-A_x$
A_y'	A_y	$-A_y$	A_y	$-A_y$
A_z'	A_z	$-A_z$	$-A_z$	A_z

Σ critical point

	$(k_0,k_0,0)$	$(k_0,\bar{k}_0,0)$	$(k_0,0,k_0)$	$(k_0,0,\bar{k}_0)$	$(0,k_0,k_0)$	$(0,k_0,\bar{k}_0)$
A_x'	A_x	A_x	A_z	$-A_z$	A_y	A_y
A_y'	A_y	$-A_y$	A_x	A_x	A_z	$-A_z$
A_z'	A_z	A_z	A_y	A_y	A_x	A_x

TABLE III. Polarization dependences of low-field electroreflectance form factor F for Γ, Δ, Λ, L, and Σ critical points in diamond-type crystals. Longitudinal geometry is used and $(1\bar{1}0)$ face is preferred for the plane of reflection; electric field $\hat{\mathcal{E}} = (1/\sqrt{2}, -1/\sqrt{2}, 0)$. θ is the polarization angle of the incident light measured with respect to the crystallographic $\hat{z}$ direction. The polarization anisotropy is defined as $r \equiv F_{[001]}/F_{[110]}$ (or $s \equiv F_{[111]}/F_{[11\bar{2}]}$); the subscript of F denotes the polarization of the incident light. (After Kondo and Moritani, Ref. 31.)

Critical point location	Pair state symmetry	Polarization dependences of low-field electroreflectance form factor F	Conditions of the polarization anisotropy r(or s) for all types of critical point
Γ	U_{4-}	$\frac{1}{\mu} f^0$	for all cases; M_0, M_3
Δ	U_1	$\frac{1}{2}[(\frac{3}{\mu_T}+\frac{1}{\mu_L}) + (\frac{1}{\mu_T}-\frac{1}{\mu_L})\cos 2\theta]\, f^0$	$0 \leqq r \leqq 2$ $(4/5 \leqq s \leqq 2)$; M_0, M_3 $r \leqq 0$, $2 \leqq r$ $(s \leqq 4/5,\ 2 \leqq s)$; M_1, M_2
	U_5	$\frac{1}{2}[(\frac{5}{\mu_T}+\frac{3}{\mu_L}) - (\frac{1}{\mu_T}-\frac{1}{\mu_L})\cos 2\theta]\, f^0$	$2/3 \leqq r \leqq 2$ $(4/5 \leqq s \leqq 8/7)$; M_0, M_3 $r \leqq 2/3$, $2 \leqq r$ $(s \leqq 4/5,\ 8/7 \leqq s)$; M_1, M_2
Λ	U_1	$\frac{4}{9}[(\frac{5}{\mu_T}+\frac{1}{\mu_L}) - (\frac{1}{\mu_T}-\frac{1}{\mu_L})\cos 2\theta]\, f^0$	$2/3 \leqq r$ $(1/2 \leqq s \leqq 8/7)$; M_0, M_3 $r \leqq 2/3$ $(s \leqq 1/2,\ 8/7 \leqq s)$; M_1, M_2
	U_3	$\frac{4}{9}[(\frac{7}{\mu_T}+\frac{5}{\mu_L}) + (\frac{1}{\mu_T}-\frac{1}{\mu_L})\cos 2\theta]\, f^0$	$2/3 \leqq r \leqq 4/3$ $(10/11 \leqq s \leqq 8/7)$; M_0, M_3 $r \leqq 2/3$, $4/3 \leqq r$ $(s \leqq 10/11,\ 8/7 \leqq s)$; M_1, M_2

TABLE III. *(Continued)*

Critical point location	Pair state symmetry	Polarization dependences of low-field electroreflectance form factor F	Conditions of the polarization anisotropy r(or s) for all types of critical point
L	U_{2-}	$\frac{2}{9}[(\frac{5}{\mu_T}+\frac{1}{\mu_L}) - (\frac{1}{\mu_T}-\frac{1}{\mu_L})\cos 2\theta] f^0$	$2/3 \leqq r$ $(1/2 \leqq s \leqq 8/7)$; M_0, M_3 $r \leqq 2/3$ $(s \leqq 1/2,\ 8/7 \leqq s)$; M_1, M_2
	U_{3-}	$\frac{2}{9}[(\frac{7}{\mu_T}+\frac{5}{\mu_L}) + (\frac{1}{\mu_T}-\frac{1}{\mu_L})\cos 2\theta] f^0$	$2/3 \leqq r \leqq 4/3$ $(10/11 \leqq s \leqq 8/7)$; M_0, M_3 $r \leqq 2/3,\ 4/3 \leqq r$ $(s \leqq 10/11,\ 8/7 \leqq s)$; M_1, M_2
Σ	U_1	$\frac{1}{4}[(\frac{2}{\mu_{T1}}+\frac{1}{\mu_L})(3+\cos 2\theta)$ $+(\frac{1}{\mu_{T2}})(7-3\cos 2\theta)] f^0$	$2/5 \leqq r \leqq 2$ $(4/5 \leqq s \leqq 4/3)$; $(\frac{2}{\mu_{T1}}+\frac{1}{\mu_L})\frac{1}{\mu_{T2}} \geqq 0$ $r \leqq 2/5,\ 2 \leqq r$ $(s \leqq 4/5,\ 4/3 \leqq s)$; $(\frac{2}{\mu_{T1}}+\frac{1}{\mu_L})\frac{1}{\mu_{T2}} \leqq 0$
	U_2	$\frac{1}{2}[(\frac{1}{\mu_{T2}}+\frac{1}{\mu_L})(3+\cos 2\theta)$ $+(\frac{2}{\mu_{T1}})(1-\cos 2\theta)] f^0$	$0 \leqq r \leqq 2$ $(4/5 \leqq s \leqq 2)$; $(\frac{1}{\mu_{T2}}+\frac{1}{\mu_L})\frac{1}{\mu_{T1}} \geqq 0$ $r \leqq 0,\ 2 \leqq r$ $(s \leqq 4/5,\ 2 \leqq s)$; $(\frac{1}{\mu_{T2}}+\frac{1}{\mu_L})\frac{1}{\mu_{T1}} \leqq 0$
	U_3	$\frac{1}{4}[(\frac{2}{\mu_{T1}}+\frac{1}{\mu_{T2}})(3+\cos 2\theta)$ $+(\frac{1}{\mu_L})(7-3\cos 2\theta)] f^0$	$2/5 \leqq r \leqq 2$ $(4/5 \leqq s \leqq 4/3)$; $(\frac{2}{\mu_{T1}}+\frac{1}{\mu_{T2}})\frac{1}{L} \geqq 0$ $r \leqq 2/5,\ 2 \leqq r$ $(s \leqq 4/5,\ 4/3 \leqq s)$; $(\frac{2}{\mu_{T1}}+\frac{1}{\mu_{T2}})\frac{1}{\mu_L} \leqq 0$

D. Uniaxial-Stress Effects on Low-Field Electroreflectance[31]

The application of a uniaxial stress and the induced strain produces a change in the lattice parameter and the symmetry of solids, which results in significant changes in the electronic band structures, such as shifts of energy levels[46,63,81–85] and mixing of wave functions.[46,63] Considering optical transitions, strain induces changes of the interband energy $E(\vec{k})$ and variations of the optical matrix element P including the selection rules. The stress effects on low-field ER spectra may be easily treated theoretically, when the stress applied to a solid is small enough and the $\vec{k}$ dependence of the interband energy $E(\vec{k})$ in the vicinity of critical point can be assumed to be still described in the parabolic model shown in Eq. (22). In this stress region, low-field ER may be divided into line-shape and symmetry parts as shown in Eq. (36) even in the presence of strain. Thus, we can calculate the stress-induced changes in the line-shape part (the energy shifts and splittings) and in the symmetry part (the stress-dependences of the ER form factor F) using the effective strain Hamiltonian and the pair state functions to first order in the strain. These treatments may be accepted when the phenomenological broadening energy is large compared to the stress-induced energy shifts; in higher interband transitions, the shifts are nearly always small compared to the broadening energy even for large stress.

The effective Hamiltonian for electron-hole states in the presence of uniaxial stress and uniform electric field may be written

$$H = E_g^{\tau} + H_{KE} + H_{EL} + H_{str} , \tag{44}$$

where H_{str} is the effective strain Hamiltonian. Since the strain has infinite wavelength, H_{str} commutes with the envelope wave function $\mathcal{G}$ and operates on the pair band U. On the other hand, the electric field

may be considered to operate on $\mathcal{S}$ rather than U, when the field is very weak and the electron (and hole) acceleration mechanism is dominant,[23] which is the case treated in Sec. II B. Then, we can consider the effects of strain and electric field independently.

When the strain applied to a solid is small in the sense that the strain-induced splittings are small compared to the exciton binding energy or the phenomenological broadening energy, the effective strain Hamiltonian can be written[63]

$$H_{str} = \sum_{s,j,\alpha} (e_{j\alpha}^{s})^{*} \tilde{\gamma}_{j\alpha} \mathcal{D}_{j}^{s,\tau} , \tag{45}$$

where $e_{j\alpha}^{s}$ is the irreducible component of the second-rank strain tensor, $\tilde{\gamma}_{j\alpha}$ is an operator on the $\psi_{j\alpha}^{\tau}$ subspace, and $\mathcal{D}$'s are the pair-band deformation potential parameters. Since $e_{j\alpha}$ is real, the * in Eq. (45) is not needed effectively. Equation (45) is sufficient to calculate the energy shifts of the pair state $\psi_{j\alpha}^{\tau}$ to first order in the strain.

Next we wish to write the pair state function to first order in the strain for the purpose of computing optical matrix elements to that order. We can write[63]

$$\psi^{\tau,j\alpha} = \psi_{j\alpha}^{\tau} + \sum_{\substack{j1,\alpha1,s \\ j2,\alpha2}} \gamma_{j1\alpha1,j2\alpha2;j\alpha}\, e_{j1\alpha1}^{s}\, \psi_{j2\alpha2}^{\tau,s} , \tag{46}$$

where, γ is the Clebsch-Gordan coefficients,[64] $e_{j\alpha}^{s}$ is the strain tensor, and $\psi_{j\alpha}^{\tau,s}$ is the pair state function which is mixed with the state $\psi_{j\alpha}^{\tau}$ by the strain.

The strain [e] and the stress [T] are both symmetric second-rank tensors; the strain tensor e_{ij} is related to the stress tensor T_{kl} by the elastic compliance constants s_{11}, s_{12}, s_{44} in cubic crystals. The relations are[61,85,86]

$$\begin{pmatrix} e_{xx} \\ e_{yy} \\ e_{zz} \\ e_{yz} \\ e_{xz} \\ e_{xy} \end{pmatrix} = \begin{pmatrix} s_{11} & s_{12} & s_{12} & & & \\ s_{12} & s_{11} & s_{12} & & & \\ s_{12} & s_{12} & s_{11} & & & \\ & & & s_{44}/2 & & \\ & & & & s_{44}/2 & \\ & & & & & s_{44}/2 \end{pmatrix} \begin{pmatrix} T_{xx} \\ T_{yy} \\ T_{zz} \\ T_{yz} \\ T_{xz} \\ T_{xy} \end{pmatrix} . \tag{47}$$

On the other hand, the stress tensor [T] for the applied force $\vec{T}$ can be written

$$[T] = \begin{pmatrix} T_{xx} & T_{xy} & T_{xz} \\ T_{xy} & T_{yy} & T_{yz} \\ T_{xz} & T_{yz} & T_{zz} \end{pmatrix} = \begin{pmatrix} \alpha\alpha & \alpha\beta & \alpha\gamma \\ \alpha\beta & \beta\beta & \beta\gamma \\ \alpha\gamma & \beta\gamma & \gamma\gamma \end{pmatrix} T , \tag{48}$$

where α, β, γ are the direction cosines between the applied force $\vec{T}$ and the three principal coordinates $\vec{x}$, $\vec{y}$, $\vec{z}$, respectively. T is the magnitude of the applied force; its sign is minus for compression.[87]
For example, we show the stress and the strain tensors for the [001] and [111] stresses

[001] stress

$$\alpha = 0,\ \beta = 0,\ \gamma = 1, \tag{49}$$

$$T_{zz} = T,\ T_{xx} = T_{yy} = T_{yz} = T_{xz} = T_{xy} = 0, \tag{50}$$

$$e_{xx} = e_{yy} = s_{12}T,\ e_{zz} = s_{11}T,\ e_{yz} = e_{xz} = e_{xy} = 0, \tag{51}$$

[111] stress

$$\alpha = \beta = \gamma = 1/\sqrt{3}, \tag{52}$$

$$T_{xx} = T_{yy} = T_{zz} = T_{yz} = T_{xz} = T_{xy} = T/3, \tag{53}$$

$$e_{xx} = e_{yy} = e_{zz} = (s_{11} + 2s_{12})T/3,\ e_{yz} = e_{xz} = e_{xy} = s_{44}/6. \tag{54}$$

On the basis of the above arguments, we calculate the stress effects of the degenerate $\Lambda_3^v - \Lambda_1^c$ critical point. The optical properties of this critical point are represented by the U_3 pair band in the Λ direction

($\Gamma_3 \times \Gamma_1 = \Gamma_3$, in Koster's notation).[65] First, the strain Hamiltonian of Eq. (45) can be written down as

$$H_{str} = D_1^1 e_1^1 I + D_1^5 e_1^5 I + \mathcal{D}_3^3 (e_{3\alpha}^3 \tilde{\gamma}_{3\alpha} + e_{3\beta}^3 \tilde{\gamma}_{3\beta}) + \mathcal{D}_3^5 (e_{3\alpha}^5 \tilde{\gamma}_{3\alpha} + e_{3\beta}^5 \tilde{\gamma}_{3\beta}) , \quad (55)$$

where

$$\begin{pmatrix} e_1^1 \\ e_{3\alpha}^3 \\ e_{3\beta}^3 \\ e_1^5 \\ e_{3\alpha}^5 \\ e_{3\beta}^5 \end{pmatrix} = \frac{1}{\sqrt{6}} \begin{pmatrix} \sqrt{2} & \sqrt{2} & \sqrt{2} & & & \\ -1 & -1 & 2 & & & \\ \sqrt{3} & -\sqrt{3} & 0 & & & \\ & & & \sqrt{2} & \sqrt{2} & \sqrt{2} \\ & & & -1 & -1 & 2 \\ & & & \sqrt{3} & -\sqrt{3} & 0 \end{pmatrix} \begin{pmatrix} e_{xx} \\ e_{yy} \\ e_{zz} \\ e_{yz} \\ e_{zx} \\ e_{xy} \end{pmatrix} , \quad (56)$$

$$I = \begin{pmatrix} 1 & 0 \\ 0 & 1 \end{pmatrix} , \quad \tilde{\gamma}_{3\alpha} = \begin{pmatrix} -1 & 0 \\ 0 & 1 \end{pmatrix} , \quad \tilde{\gamma}_{3\beta} = \begin{pmatrix} 0 & 1 \\ 1 & 0 \end{pmatrix} . \quad (57)$$

Equation (57) refers to the basis set $\psi_{3\alpha}^{\tau}$, $\psi_{3\beta}^{\tau}$.

Second, we may write the pair state functions to first order in the strain using Eq. (46)

$$\psi^{\tau,3\alpha} = \psi_{3\alpha}^{\tau} + \left(\frac{-e_{3\alpha}^3 \psi_{3\alpha}^{\tau,3}}{\sqrt{2}} + \frac{e_{3\beta}^3 \psi_{3\beta}^{\tau,3}}{\sqrt{2}}\right) + \left(\frac{-e_{3\alpha}^5 \psi_{3\alpha}^{\tau,5}}{\sqrt{2}} + \frac{e_{3\beta}^5 \psi_{3\beta}^{\tau,5}}{\sqrt{2}}\right) , \quad (58)$$

$$\psi^{\tau,3\beta} = \psi_{3\beta}^{\tau} + \left(\frac{e_{3\alpha}^3 \psi_{3\beta}^{\tau,3}}{\sqrt{2}} + \frac{e_{3\beta}^3 \psi_{3\alpha}^{\tau,3}}{\sqrt{2}}\right) + \left(\frac{e_{3\alpha}^5 \psi_{3\beta}^{\tau,5}}{\sqrt{2}} + \frac{e_{3\beta}^5 \psi_{3\alpha}^{\tau,5}}{\sqrt{2}}\right) . \quad (59)$$

Here, the irreducible pair state functions, $\psi_{3\alpha}^{\tau}$ and $\psi_{3\beta}^{\tau}$, in the absence of strain can be written down using Eq. (3):

$$\psi_{3\alpha}{}^{\tau} = a_1{}^{\tau}\mathcal{G}_1{}^{\tau}U_{3\alpha} - a_2{}^{\tau}\mathcal{G}_2{}^{\tau}U_{3\beta} - \frac{a_3{}^{\tau}}{\sqrt{2}}\mathcal{G}_{3\alpha}{}^{\tau}U_{3\alpha} + \frac{a_3{}^{\tau}}{\sqrt{2}}\mathcal{G}_{3\beta}{}^{\tau}U_{3\beta}{}^{\tau}, \quad (60)$$

$$\psi_{3\beta}{}^{\tau} = a_1{}^{\tau}\mathcal{G}_1{}^{\tau}U_{3\beta} + a_2{}^{\tau}\mathcal{G}_2{}^{\tau}U_{3\alpha} + \frac{a_3{}^{\tau}}{\sqrt{2}}\mathcal{G}_{3\alpha}{}^{\tau}U_{3\beta} + \frac{a_3{}^{\tau}}{\sqrt{2}}\mathcal{G}_{3\beta}{}^{\tau}U_{3\alpha}{}^{\tau}. \quad (61)$$

From Eq. (11), only the first terms in the right sides of Eqs. (60) and (61) may be important in order to calculate the optical matrix element P. Due to this fact, the calculations of the strain-induced changes of P using Eqs. (10), (11), and (58) through (61) may be much simplified. Third, the $\Lambda_3^v - \Lambda_1^c$ critical point consists of the eight equivalent components along the <111> lines in the Brillouin zone. Since uniaxial stress does not remove the inversion symmetry of the crystal, we need not consider all eight components but four along the [111], $[1\bar{1}\bar{1}]$, $[\bar{1}1\bar{1}]$, $[\bar{1}\bar{1}1]$ lines. The simplest way to sum over the star of $\vec{K}_0$ is to keep $\vec{K}_0$ fixed and sum over a complete set of the effective components of the strain tensor. The effective irreducible components of the strain tensor for the star of $\vec{K}_0 = (\frac{2\pi}{a})(\vec{k}_0, \vec{k}_0, \vec{k}_0)$ are presented in Table IV. The effective components of the vector potential are already given in Table II.

The energy shifts of the U_3 band for stresses in the [001] and [111] directions can be obtained by diagonalyzing Eq. (55) with use of Eqs. (51), (54), (56), (57), and Table IV. The stress-induced changes of the ER form factor F can also be calculated from Eq. (38) with use of Eqs. (10), (11), (39) through (41), (51), (54), (56), (58) through (61), and Tables I, II, IV. The results are presented in Table V. In Table V, D_1^1 $(=\mathcal{D}_1^1)$ is the hydrostatic deformation parameter, D_1^5 $(=\mathcal{D}_1^5)$ is the interband deformation parameter for [111] stress, and $\mathcal{D}_3^3$ $(\mathcal{D}_3^5)$ is the intraband deformation parameter for [001] ([111]) stress. The factor F is given for the polarizations in the [100], [010], [001], $[1\bar{1}0]$, and [110] directions with [001] stress and for the polarizations in the $[1\bar{1}0]$, $[11\bar{2}]$,

TABLE IV. Effective irreducible components of the strain tensor for the star of $\vec{K}_0 = (k_0, k_0, k_0)$ in diamond-type crystals. The effective components are primed and the actual components are unprimed. (After Kane.[63])

	(k_0, k_0, k_0)	$(k_0, \bar{k}_0, \bar{k}_0)$	$(\bar{k}_0, k_0, \bar{k}_0)$	$(\bar{k}_0, \bar{k}_0, k_0)$
$(e_1^1)'$	e_1^1	e_1^1	e_1^1	e_1^1
$(e_{3\alpha}^3)'$	$e_{3\alpha}^3$	$e_{3\alpha}^3$	$e_{3\alpha}^3$	$e_{3\alpha}^3$
$(e_{3\beta}^3)'$	$e_{3\beta}^3$	$e_{3\beta}^3$	$e_{3\beta}^3$	$e_{3\beta}^3$
$(e_1^5)'$	e_1^5	$-\frac{1}{3}e_1^5 - \frac{\sqrt{2}}{3}e_{3\alpha}^5 + \frac{\sqrt{2}}{\sqrt{3}}e_{3\beta}^5$	$-\frac{1}{3}e_1^5 - \frac{\sqrt{2}}{3}e_{3\alpha}^5 - \frac{\sqrt{2}}{\sqrt{3}}e_{3\beta}^5$	$-\frac{1}{3}e_1^5 + \frac{2\sqrt{2}}{3}e_{3\alpha}^5$
$(e_{3\alpha}^5)'$	$e_{3\alpha}^5$	$-\frac{\sqrt{2}}{3}e_1^5 - \frac{2}{3}e_{3\alpha}^5 - \frac{1}{\sqrt{3}}e_{3\beta}^5$	$-\frac{\sqrt{2}}{3}e_1^5 - \frac{2}{3}e_{3\alpha}^5 + \frac{1}{\sqrt{3}}e_{3\beta}^5$	$\frac{2\sqrt{2}}{3}e_1^5 + \frac{1}{3}e_{3\alpha}^5$
$(e_{3\beta}^5)'$	$e_{3\beta}^5$	$\frac{\sqrt{2}}{\sqrt{3}}e_1^5 - \frac{1}{\sqrt{3}}e_{3\alpha}^5$	$-\frac{\sqrt{2}}{\sqrt{3}}e_1^5 + \frac{1}{\sqrt{3}}e_{3\alpha}^5$	$-e_{3\beta}^5$

and [111] directions with [111] stress. f^0 is a unit of the optical matrix element defined by Eq. (39) in the unstrained crystal and f^s is a change due to admixture of first-order wave function $\psi_{3\alpha}{}^s$ in the strain.

The uniaxial-stress effects on low-field ER spectra for the degenerate $\Delta_5^v - \Delta_1^c$ critical point are presented in Table VI. The optical properties of this critical point are represented by the U_5 pair band in the Δ direction. In Table VI, D_1^3 is the interband deformation parameter for [001] stress and $\mathcal{D}_3$ ($\mathcal{D}_4$) is the intraband deformation parameter for [001] ([111]) stress. f^s is a change of the optical matrix element due to admixture of first-order wave function $\psi_{3\alpha}{}^s$ in the strain.

The uniaxial stress effects on low-field ER spectra for the degenerate $\Gamma_{25'}^v - \Gamma_{15}^c$ critical point are presented in Table VII. The optical properties of this critical point are represented by the U_{4-} pair band at the Γ point. In Table VII, $\mathcal{D}_3$($\mathcal{D}_5$) is the intraband deformation parameter for [001] ([111]) stress. f^s is a change of the optical matrix element due to admixture of first-order wave function $\psi_{4\alpha}{}^s$ in the strain.

TABLE V. Energy shift ΔE and electroreflectance form factor F for the degenerate U_3 band in the Λ direction. Spin-orbit interaction is neglected. The factor F has been summed over the eight equivalent components. The subscript of F denotes the polarization of the light. (After Kondo and Moritani.[31])

Energy shift[a]	Electroreflectance form factor
	[001] stress
$\Delta E^A = \frac{D_1^1}{\sqrt{3}}(s_{11}+2s_{12})T + \sqrt{\frac{2}{3}}\mathcal{D}_3^3(s_{11}-s_{12})T$	$F^A_{[100]} = F^A_{[010]} = \frac{1}{4}F^A_{[001]} = \frac{4}{9}(\frac{2}{\mu_T}+\frac{1}{\mu_L})\, f^3_+$
	$F^A_{[1\bar{1}0]} = \frac{4}{9}[(\frac{2}{\mu_T}+\frac{1}{\mu_L}) + 2(\frac{1}{\mu_T}-\frac{1}{\mu_L})\mathcal{E}_x\mathcal{E}_y]\, f^3_+$
	$F^A_{[110]} = \frac{4}{9}[(\frac{2}{\mu_T}+\frac{1}{\mu_L}) - 2(\frac{1}{\mu_T}-\frac{1}{\mu_L})\mathcal{E}_x\mathcal{E}_y]\, f^3_+$
$\Delta E^B = \frac{D_1^1}{\sqrt{3}}(s_{11}+2s_{12})T - \sqrt{\frac{2}{3}}\mathcal{D}_3^3(s_{11}-s_{12})T$	$F^B_{[100]} = F^B_{[010]} = \frac{4}{3}(\frac{2}{\mu_T}+\frac{1}{\mu_L})\, f^3_-$, $F^B_{[001]} = 0$
	$F^B_{[1\bar{1}0]} = \frac{4}{3}[(\frac{2}{\mu_T}+\frac{1}{\mu_L}) - 2(\frac{1}{\mu_T}-\frac{1}{\mu_L})\mathcal{E}_x\mathcal{E}_y]\, f^3_-$
	$F^B_{[110]} = \frac{4}{3}[(\frac{2}{\mu_T}+\frac{1}{\mu_L}) + 2(\frac{1}{\mu_T}-\frac{1}{\mu_L})\mathcal{E}_x\mathcal{E}_y]\, f^3_-$
	[111] stress
$\Delta E^a = \frac{D_1^1}{\sqrt{3}}(s_{11}+2s_{12})T + \frac{D_1^5}{2\sqrt{3}}s_{44}T$	$F^a_{[1\bar{1}0]} = F^a_{[11\bar{2}]} = \frac{2}{3}[(\frac{2}{\mu_T}+\frac{1}{\mu_L}) - 2(\frac{1}{\mu_T}-\frac{1}{\mu_L})(\mathcal{E}_x\mathcal{E}_y+\mathcal{E}_y\mathcal{E}_z+\mathcal{E}_z\mathcal{E}_x)]\, f^0$

TABLE V. *(Continued)*

Energy shift[a]	Electroreflectance form factor
	$F^{a}_{[111]} = 0$
$\Delta E^{b} = \frac{D^{1}_{1}}{\sqrt{3}}(s_{11} + 2s_{12})T - \frac{D^{5}_{1}}{6\sqrt{3}} s_{44}T + \frac{\sqrt{2}}{3\sqrt{3}} \mathcal{D}^{5}_{3} s_{44}T$	$F^{b}_{[1\bar{1}0]} = \frac{1}{9}[(\frac{2}{\mu_T} + \frac{1}{\mu_L}) + 2(\frac{1}{\mu_T} - \frac{1}{\mu_L}) \mathcal{E}_x \mathcal{E}_y] f^{5}_{+}$
	$F^{b}_{[11\bar{2}]} = \frac{1}{27}[3(\frac{2}{\mu_T} + \frac{1}{\mu_L}) - 2(\frac{1}{\mu_T} - \frac{1}{\mu_L})(\mathcal{E}_x \mathcal{E}_y - 2\mathcal{E}_y \mathcal{E}_z - 2\mathcal{E}_z \mathcal{E}_x)] f^{5}_{+}$
	$F^{b}_{[111]} = \frac{16}{27}[3(\frac{2}{\mu_T} + \frac{1}{\mu_L}) + 2(\frac{1}{\mu_T} - \frac{1}{\mu_L})(\mathcal{E}_x \mathcal{E}_y + \mathcal{E}_y \mathcal{E}_z + \mathcal{E}_z \mathcal{E}_x)] f^{5}_{+}$
$\Delta E^{c} = \frac{D^{1}_{1}}{\sqrt{3}}(s_{11} + 2s_{12})T - \frac{D^{5}_{1}}{6\sqrt{3}} s_{44}T - \frac{\sqrt{2}}{3\sqrt{3}} \mathcal{D}^{5}_{3} s_{44}T$	$F^{c}_{[1\bar{1}0]} = \frac{1}{3}[3(\frac{2}{\mu_T} + \frac{1}{\mu_L}) - 2(\frac{1}{\mu_T} - \frac{1}{\mu_L})(\mathcal{E}_x \mathcal{E}_y - 2\mathcal{E}_y \mathcal{E}_z - 2\mathcal{E}_z \mathcal{E}_x)] f^{5}_{-}$
	$F^{c}_{[11\bar{2}]} = [(\frac{2}{\mu_T} + \frac{1}{\mu_L}) + 2(\frac{1}{\mu_T} - \frac{1}{\mu_L}) \mathcal{E}_x \mathcal{E}_y] f^{5}_{-}$
	$F^{c}_{[111]} = 0$

$$f^{3}_{+} = f^{0} + \frac{1}{\sqrt{3}}(s_{11} - s_{12})Tf^{3} \qquad f^{3}_{-} = f^{0} - \frac{1}{\sqrt{3}}(s_{11} - s_{12})Tf^{3}$$

$$f^{5}_{+} = f^{0} + \frac{1}{3\sqrt{3}} s_{44}Tf^{5} \qquad f^{5}_{-} = f^{0} - \frac{1}{3\sqrt{3}} s_{44}Tf^{5}$$

$$f^{0} \equiv \langle 0|p_{3\alpha}|\psi_{3\alpha}\rangle^{2} \qquad f^{s} \equiv 2\langle 0|p_{3\alpha}|\psi_{3\alpha}\rangle\langle\psi^{s}_{3\alpha}|p_{3\alpha}|0\rangle$$

[a] These energy shifts have been calculated by E. O. Kane. See Table VII of Ref. 63.

TABLE VI. Energy shift ΔE and electroreflectance form factor F for the degenerate U_5 band in the Δ direction. Spin-orbit interaction is neglected. The factor F has been summed over the six equivalent components. The subscript of F denotes the polarization of the light. (After Kondo and Moritani.[31])

Energy shift[a]	Electroreflectance form factor
	[001] stress
$\Delta E^A = \frac{D_1^1}{\sqrt{3}}(s_{11}+2s_{12})T + \sqrt{\frac{2}{3}}D_1^3(s_{11}-s_{12})T$	$F^A_{[100]} = F^A_{[010]} = 2[\frac{1}{\mu_T} - (\frac{1}{\mu_T}-\frac{1}{\mu_L})\mathcal{E}_z^2]f^0, \quad F^A_{[001]} = 0$
	$F^A_{[1\bar{1}0]} = F^A_{[110]} = 2[\frac{1}{\mu_T} - (\frac{1}{\mu_T}-\frac{1}{\mu_L})\mathcal{E}_z^2]f^0$
$\Delta E^B = \frac{D_1^1}{\sqrt{3}}(s_{11}+2s_{12})T - \frac{D_1^3}{\sqrt{6}}(s_{11}-s_{12})T + \frac{\mathcal{D}_3}{\sqrt{2}}(s_{11}-s_{12})T$	$F^B_{[100]} = F^B_{[010]} = F^B_{[1\bar{1}0]} = F^B_{[110]} = 0$
	$F^B_{[001]} = 2[(\frac{1}{\mu_T}+\frac{1}{\mu_L}) + (\frac{1}{\mu_T}-\frac{1}{\mu_L})\mathcal{E}_z^2]f_+^3$
$\Delta E^C = \frac{D_1^1}{\sqrt{3}}(s_{11}+2s_{12})T - \frac{D_1^3}{\sqrt{6}}(s_{11}-s_{12})T - \frac{\mathcal{D}_3}{\sqrt{2}}(s_{11}-s_{12})T$	$F^C_{[100]} = 2[\frac{1}{\mu_T} - (\frac{1}{\mu_T}-\frac{1}{\mu_L})\mathcal{E}_y^2]f_-^3$
	$F^C_{[010]} = 2[\frac{1}{\mu_T} - (\frac{1}{\mu_T}-\frac{1}{\mu_L})\mathcal{E}_x^2]f_-^3$
	$F^C_{[1\bar{1}0]} = F^C_{[110]} = [(\frac{1}{\mu_T}+\frac{1}{\mu_L}) + (\frac{1}{\mu_T}-\frac{1}{\mu_L})\mathcal{E}_z^2]f_-^3$
	$F^C_{[001]} = 0$

TABLE VI. *(Continued)*

Energy shift[a]	Electroreflectance form factor
	[111] stress
$\Delta E^a = \frac{D_1^1}{\sqrt{3}}(s_{11} + 2s_{12})T + \frac{\mathcal{D}_4}{6} s_{44}T$	$F^a_{[1\bar{1}0]} = \frac{1}{2}[(\frac{1}{\mu_T} + \frac{1}{\mu_L}) + (\frac{1}{\mu_T} - \frac{1}{\mu_L}) \mathcal{E}_z^2]\, f_+^4$
	$F^a_{[11\bar{2}]} = \frac{1}{6}[(\frac{5}{\mu_T} + \frac{1}{\mu_L}) - 3(\frac{1}{\mu_T} - \frac{1}{\mu_L}) \mathcal{E}_z^2]\, f_+^4$
	$F^a_{[111]} = \frac{4}{3}(\frac{2}{\mu_T} + \frac{1}{\mu_L})\, f_+^4$
$\Delta E^b = \frac{D_1^1}{\sqrt{3}}(s_{11} + 2s_{12})T - \frac{\mathcal{D}_4}{6} s_{44}T$	$F^b_{[1\bar{1}0]} = \frac{1}{2}[(\frac{5}{\mu_T} + \frac{1}{\mu_L}) - 3(\frac{1}{\mu_T} - \frac{1}{\mu_L}) \mathcal{E}_z^2]\, f_-^4$
	$F^b_{[11\bar{2}]} = \frac{3}{2}[(\frac{1}{\mu_T} + \frac{1}{\mu_L}) + (\frac{1}{\mu_T} - \frac{1}{\mu_L}) \mathcal{E}_z^2]\, f_-^4$
	$F^b_{[111]} = 0$
$f_+^3 = f^0 + \frac{1}{\sqrt{2}}(s_{11} - s_{12})Tf^3$	$f_-^3 = f^0 - \frac{1}{\sqrt{2}}(s_{11} - s_{12})Tf^3$
$f_+^4 = f^0 + \frac{1}{6} s_{44}Tf^4$	$f_-^4 = f^0 - \frac{1}{6} s_{44}Tf^4$
$f^0 \equiv \langle 0 \vert p_{5\alpha} \vert \psi_{5\alpha} \rangle^2$	$f^s \equiv 2\langle 0 \vert p_{5\alpha} \vert \psi_{5\alpha} \rangle \langle \psi^s_{5\alpha} \vert p_{5\alpha} \vert 0 \rangle$

[a] These energy shifts have been calculated by E. O. Kane. See Table III of Ref. 63.

TABLE VII. Energy shift ΔE and electroreflectance form factor F for the degenerate U_4 band at the Γ point. Spin-orbit interaction is neglected. The subscript of F denotes the polarization of the light.

Energy shift[a]	Electroreflectance form factor
	[001] stress
$\Delta E^A = \frac{D_1^1}{\sqrt{3}}(s_{11}+2s_{12})T + \frac{2}{\sqrt{3}}\mathcal{D}_3(s_{11}-s_{12})T$	$F^A_{[100]} = F^A_{[010]} = F^A_{[1\bar{1}0]} = F^A_{[110]} = 0$
	$F^A_{[001]} = \frac{1}{\mu}[f^0 + \frac{2\sqrt{2}}{\sqrt{3}}(s_{11}-s_{12})Tf^3]$
$\Delta E^B = \frac{D_1^1}{\sqrt{3}}(s_{11}+2s_{12})T - \frac{1}{\sqrt{3}}\mathcal{D}_3(s_{11}-s_{12})T$	$F^B_{[100]} = F^B_{[010]} = F^B_{[1\bar{1}0]} = F^B_{[110]} = \frac{1}{\mu}[f^0 - \frac{\sqrt{2}}{\sqrt{3}}(s_{11}-s_{12})Tf^3]$
	$F^B_{[001]} = 0$
	[111] stress
$\Delta E^a = \frac{D_1^1}{\sqrt{3}}(s_{11}+2s_{12})T + \frac{\mathcal{D}_5}{\sqrt{6}}s_{44}T$	$F^a_{[1\bar{1}0]} = F^a_{[11\bar{2}]} = 0,\ F^a_{[111]} = \frac{1}{\mu}(f^0 + \frac{1}{3}s_{44}Tf^5)$
$\Delta E^b = \frac{D_1^1}{\sqrt{3}}(s_{11}+2s_{12})T - \frac{\mathcal{D}_5}{2\sqrt{6}}s_{44}T$	$F^b_{[1\bar{1}0]} = F^b_{[11\bar{2}]} = \frac{1}{\mu}(f^0 - \frac{1}{6}s_{44}Tf^5),\ F^b_{[111]} = 0$
$f^0 \equiv \langle 0 \vert p_{4\alpha} \vert \psi_{4\alpha}\rangle^2$	$f^s \equiv 2\langle 0 \vert p_{4\alpha} \vert \psi_{4\alpha}\rangle\langle \psi^s_{4\alpha} \vert p_{4\alpha} \vert 0\rangle$

[a] These energy shifts have been calculated by E. O. Kane. See Eqs. (3.39) through (3.42) of Ref. 63.

III. EXPERIMENTAL

A. Sample Construction

The Si single-crystal samples used in the experiment were all n-type and had a room-temperature resistivity of about 0.5 Ω cm. The crystal orientation of the samples was determined from x-ray diffraction with an accuracy of 1 degree. These samples were cut into rectangular parallelepipeds to dimensions of $12.0 \times 1.0 \times 1.0$ mm^3 such that the long axis was in either the [001] or [111] direction.

The surfaces of all the samples were mechanically polished and chemically etched in order to remove surface damages. An optically flat $(1\bar{1}0)$ face was chosen as a plane of reflection and the Schottky-barrier was formed by evaporating a semitransparent Ni film on the surface. The thickness of the Ni film is estimated to be 10 − 20 nm from the reflectivity measurements of the air-Ni-Si system.[88] A thick In film was evaporated onto the back surface of the sample in order to make a nonrectifying contact.

B. Measurement Techniques

Electroreflectance spectra were measured with standard optical and phase-sensitive electronic detection techniques.[7] The block diagram of the system is shown in Fig. 2.

The optical system consisted of a 500-W Ushio model UXL 500 D xenon lamp, a JASCO model CT-50 0.5-m grating monochromator with a 1200-line/mm grating blazed at 300 nm, a cryotip refrigerator on a cryostat in a stress apparatus, and a Hamamatsu TV model R 376 photomultiplier. The polarization measurements were made with a Glan-Thompson polarizer in the energy range from 3.0 to 4.0 eV and with a Rochon prism in the energy range from 4.0 to 5.0 eV.

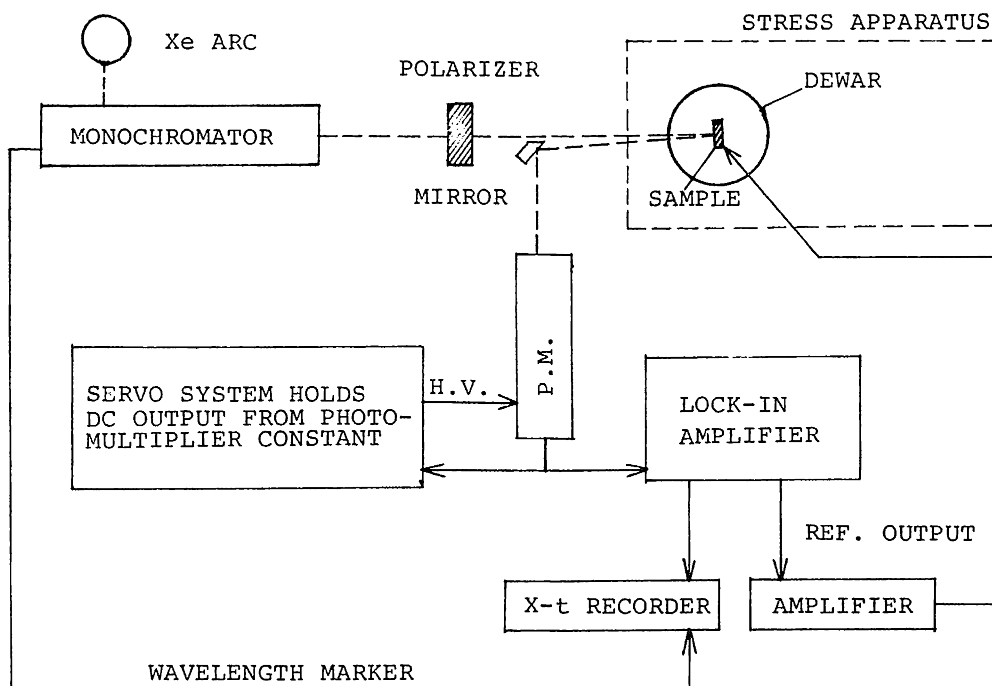

FIG. 2. Experimental setup for electroreflectance measurements. The details are shown in the text.

The samples used in the stress experiment were mounted in a sample cell of the stress apparatus such that the long axis of the sample was parallel to the pushing rod. Schematic diagram of the sample cell and the stress apparatus is shown in Fig. 3. In Fig. 3(a), a paper sheet (E) was placed between the round piece (D) and the sample (F) in order to reduce the imperfect alignment. The position of the light spot on the sample was adjusted by replacing the rectangular piece (G). As shown in Fig. 3(b), a static load was applied to the sample by a simple lever system.

The dc bias and 400-Hz square-wave ac-modulation voltage were applied to the metal layer by means of a thin copper wire attached to the metal film with a dot of silver paint. Since low-field ER spectra are independent of the modulating waveform,[22,23] the square-wave voltage was used in our measurements.

The detection system was as follows: The dc signal of the photomultiplier, which is proportional to $R+\Delta R \cong R$, was held constant by varying the photomultiplier gain electronically.[89] Then, the ac signal of the photomultiplier by the electric field modulation, which is a direct measure of $\Delta R/R$, was detected with a PAR HR-8 lock-in amplifier and recorded on a x-t recorder.

We check the observed ER spectra to be actually in the low-field modulation limit by inspecting the linear relation of the reflectivity change $\Delta R/R$ versus ac-modulating voltage with holding the dc bias constant.[22,23] The energy shifts of the peak positions with ac-modulating voltage were not observed in the measurements.

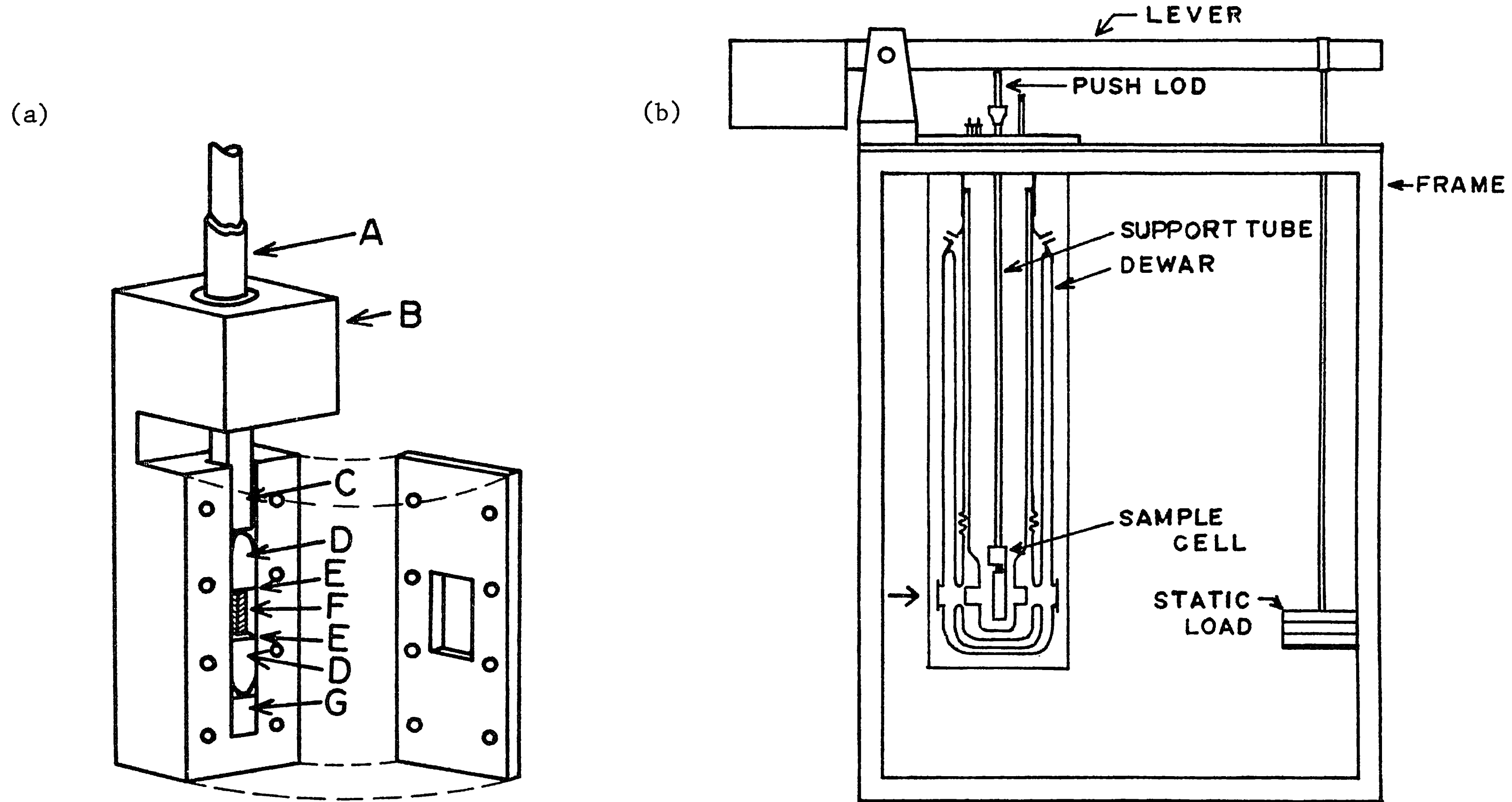

FIG. 3. Schematic diagram of (a) the sample cell and (b) the stress apparatus. A: support tube, B: sample cell, C: pushing rod, D: round piece, E: paper sheet, F: sample, G: rectangular piece. A, B, C, D, and G are made of stainless steel.

IV. RESULTS AND ANALYSIS

A. E_0' and E_1 Structures

a. *Best-Fit Analysis*

Figure 4 shows a Schottky-barrier ER spectrum of Si in the energy range from 3.2 to 3.6 eV at room temperature. The spectrum shown in Fig. 4 is rather complicated; however, it is reasonable to consider that two different structures are found in this spectrum. One is a dominant structure (S_I) and the other is a weak one (S_{II}) which is superimposed on the low-energy negative peak of the S_I structure. We have determined the band-edge parameters by performing a least-squares fit of the three- and two-dimensional low-field resonant functions to the observed spectra. The determined parameters are listed in Table VIII with values quoted from other modulation measurements in the literature. The calculated line shapes are also illustrated in Fig. 4.

In the best-fit procedures, the field inhomogeneity effect (Eq. (34)) was neglected in our samples and the strength parameter g of the contact-exciton effect (Eq. (35)) was considered as an adjustable parameter. The Seraphin coefficients of the air-Ni-Si three phase system were used, which is derived in Appendix A. The values of the Seraphin coefficients calculated from the reflectivity spectra of Si and Ni are plotted in Fig. 5 with the thickness of the Ni film as a parameter.[92] As shown in Fig. 5, both α and β decrease and become rather structureless on increasing the thickness of the Ni film. Since the estimated thickness of the Ni film may be 10 nm in our samples, $\alpha \simeq \beta$ at 3.3 eV and $|\alpha| < |\beta|$, $\beta > 0$ around 3.4 eV in Fig. 5. Therefore, the S_{II} structure of $\Delta R/R$ is affected by $\Delta\epsilon_1$ and $\Delta\epsilon_2$ in almost the same amount and the S_I structure is nearly $\Delta\epsilon_2$ dominant.

Returning to Fig. 4, the two-dimensional resonant function[19,23] was

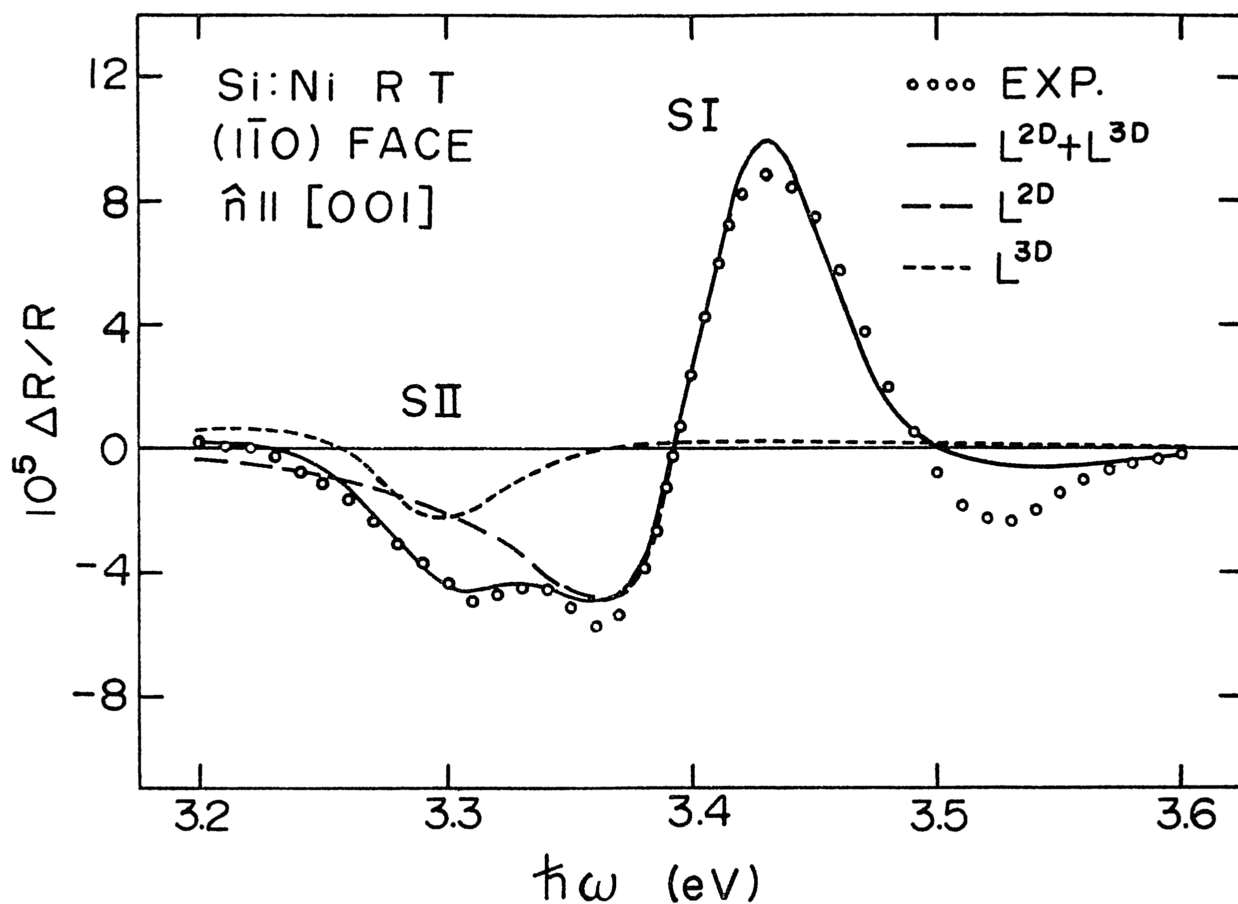

FIG. 4. Schottky-barrier ER spectrum of Si in the energy range of E_0' and E_1 transitions at room temperature (RT). Open circles are the experimental results, taken on (1$\bar{1}$0) face for [001] polarization in the low-field modulation limit. Short-dashed and long-dashed lines are the calculated three-dimensional (L^{3D}) and two-dimensional (L^{2D}) line shapes, respectively. Solid line is the sum of the above two line shapes. (After Kondo and Moritani.[31])

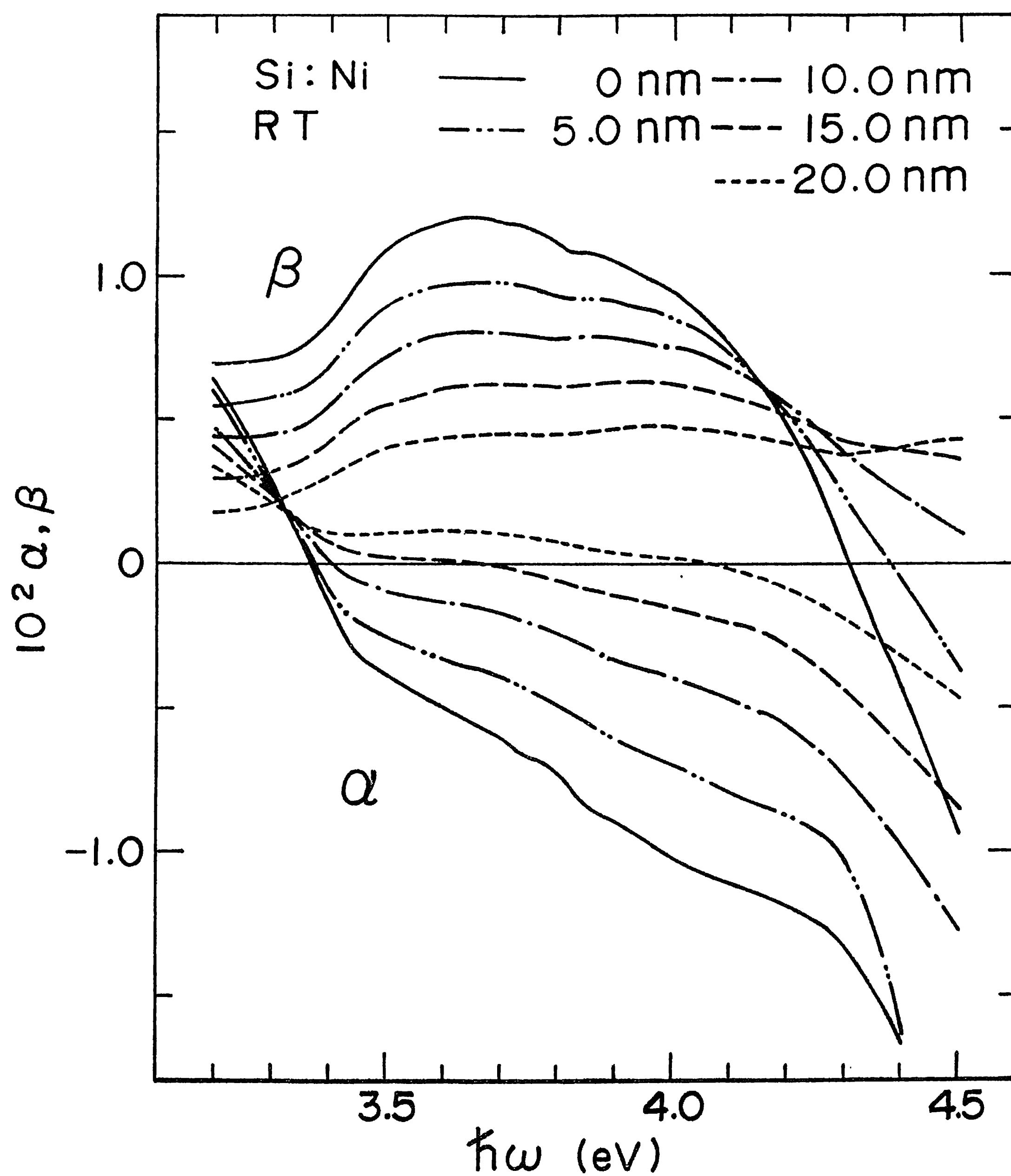

FIG. 5. Seraphin coefficients of the air-Ni-Si three phase system at room temperature (RT), calculated from the reflectivity spectra of Ni and Si. The results are shown with the thickness of Ni film as a parameter. (After Kondo and Moritani.[31])

TABLE VIII. Critical-point parameters of Si in the energy range of E_0' and E_1 transitions as obtained from electroreflectance (ER), wavelength-modulated reflectance (WMR), and thermoreflectance (TR) measurements. RT stands for room temperature.

		This work[a] ER (RT)	Grover and Handler[b] ER (RT)	Lukeš et al.[c] ER (90 K)	Seraphin and Bottka[d] ER (95 K)
	E_g (eV)	3.412 ± 0.005	3.360 ± 0.016	3.44 ± 0.05	3.41
	Γ (eV)	0.060 ± 0.005	0.05322 ± 0.00236		0.035
E_1	Symmetry	$\Lambda_3^v(L_{3'}^v) \rightarrow \Lambda_1^c(L_1^c)$	$\Lambda_3^v \rightarrow \Lambda_1^c$		
	Type (reduced-mass relations)	M_1^{3D} $(\mu_T << \lvert\mu_L\rvert, \mu_T > 0, \mu_L < 0)$	M_0^{2D}	M_1^{3D}	M_1^{3D}
	E_g (eV)	3.294 ± 0.005	3.281 ± 0.007	3.34 ± 0.05	3.33
	Γ (eV)	0.060 ± 0.005	0.05177 ± 0.01286		0.035
E_0'	Symmetry	$\Delta_5^v \rightarrow \Delta_1^c$ near Γ		$\Gamma_{25'}^v \rightarrow \Gamma_{15}^c$	
	Type (reduced-mass relations)	M_0^{3D} $(\mu_T/\mu_L = 1-3, \mu_T > 0, \mu_L > 0)$	M_1^{3D}	M_0^{3D}	M_0^{3D}

[a] Reference 31.

[b] Reference 43.

[c] Reference 90.

[d] Reference 40.

TABLE VIII. *(Continued)*

		Forman et al.[e] ER	Zucca et al.[f] WMR (5 K)	Braunstein and Welkowsky[g] WMR (80 K)	Matatagui et al.[h] TR (77 K)
	E_g (eV)	3.485 ± 0.015	3.45 ± 0.004	3.41	3.43
	Γ (eV)				
E_1	Symmetry	$\Lambda_3^v \rightarrow \Lambda_1^c$	$\Lambda_3^v \rightarrow \Lambda_1^c$	$\Delta_5^v \rightarrow \Delta_1^c$	
	Type (reduced-mass relations)		M_1^{3D}	M_1^{3D}	M_1^{3D}
	E_g (eV)	3.370 ± 0.030	3.40 ± 0.008	3.36	3.32
	Γ (eV)				
E_0'	Symmetry	$\Gamma_{25'}^v \rightarrow \Gamma_{15}^c$	$\Delta_5^v \rightarrow \Delta_1^c$	$\Gamma_{25'}^v \rightarrow \Gamma_{15}^c$	
	Type (reduced-mass relations)			M_0^{3D}	M_0^{3D}

[e] Reference 44; see also Ref. 91.
[f] Reference 17; see also Ref. 50.
[g] Reference 16.
[h] Reference 15.

used for the S_I structure only because it gives the better-fitted result for S_I than the three-dimensional function. Almost the same values of the critical point energy were obtained for the two line-shape functions. Note, however, that it is necessary to determine the type of a critical point and the broadening energy with use of the three-dimensional function. Thus the critical points related to the S_I and S_{II} structures are determined to be the three-dimensional M_1 and M_0 types, respectively.

b. Symmetry Analysis

Next we consider the symmetry assignment for the critical points related to the S_I and S_{II} structures. The polarization anisotropies of the Schottky-barrier ER spectra of Si are shown in Fig. 6. Data were taken on the $(1\bar{1}0)$ face at 77 K. The top pair of curves was obtained at a low-field condition with two principal orthogonal polarizations, $\hat{n} \parallel [001]$ (dashed line) and $\hat{n} \parallel [110]$ (solid line). The bottom pair of curves was obtained at a low-field condition with two principal orthogonal polarizations, $\hat{n} \parallel [111]$ (dashed line) and $\hat{n} \parallel [11\bar{2}]$ (solid line). The line shapes of these spectra are analogous to that obtained by Forman et al.[44] using the transverse ER technique. As shown in Fig. 6, the S_I and S_{II} structures, especially the latter one, become sharper at 77 K than at room temperature.

We analyze the S_I structure first. From the results shown in Fig. 6, we obtain the polarization anisotropies $|r| = (\Delta R/R)_{[001]}/(\Delta R/R)_{[110]} = 1.35 \pm 0.05$ and $|s| = (\Delta R/R)_{[111]}/(\Delta R/R)_{[11\bar{2}]} = 0.86 \pm 0.05$ at the positive peak of the structure. The experimental results can be compared to the theoretical criteria listed in Table III for high symmetry Γ, Δ, Λ, L, and Σ critical points. First, the Γ critical point may be ruled out, since it gives the isotropic polarization effect. Second, the Δ

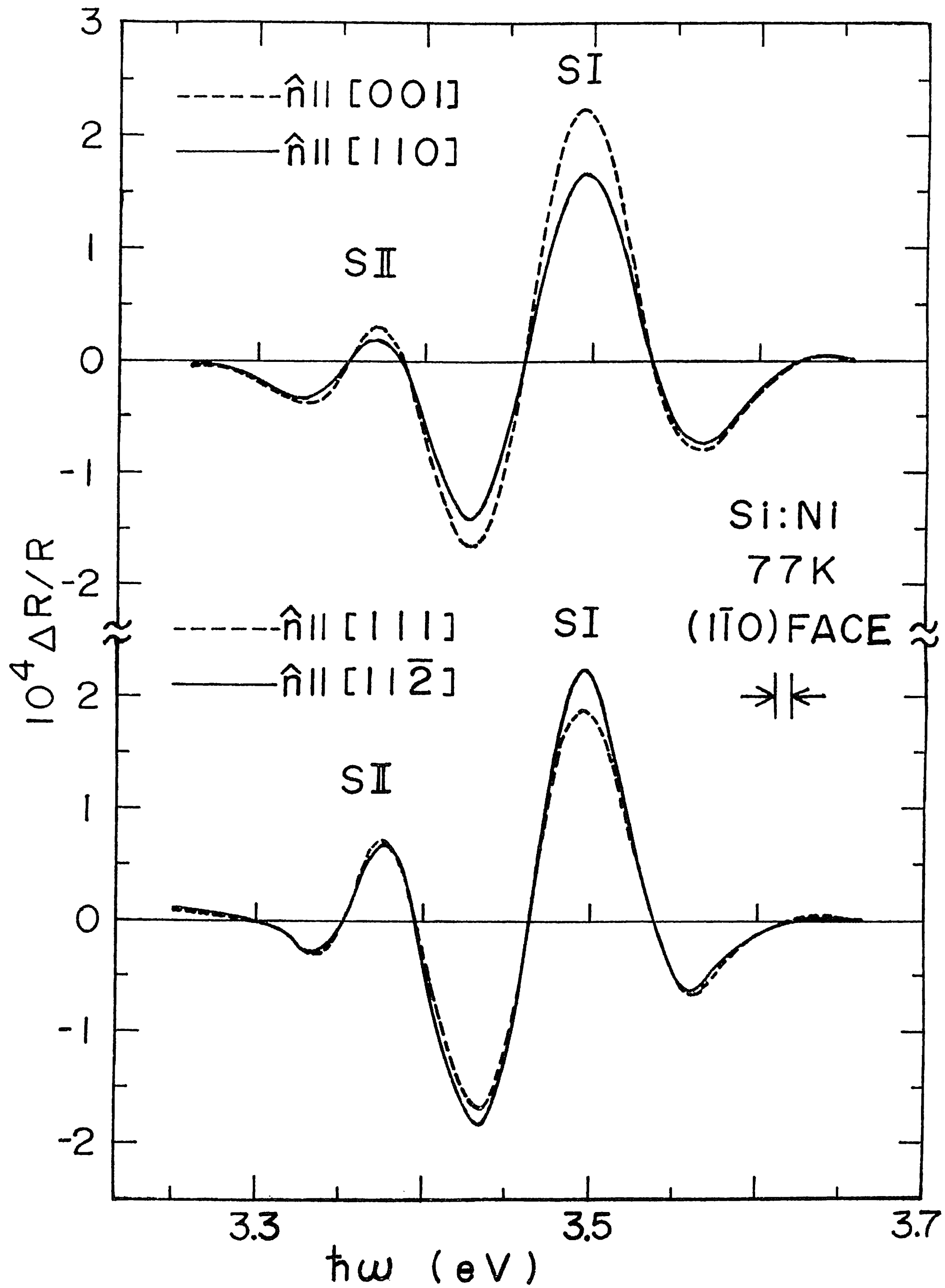

FIG. 6. Polarization anisotropies of the Schottky-barrier ER spectra of Si in the energy range of E_0' and E_1 transitions. Data are taken on (1$\bar{1}$0) face at 77 k in the low-field modulation limit. (After Kondo and Moritani.[31])

critical point may be ruled out, since the combinations of the observed polarization anisotropies and the critical point type (M_1) conflict with the conditions of the Δ critical point with U_1 and U_5 symmetry. Third, the Λ (or L) critical point with U_1 (or U_{2-}) symmetry may be ruled out because of the same reasons as in the case of the Δ critical point. For the Λ (or L) critical point with U_3 (or U_{3-}) symmetry, the polarization anisotropies may be written from Table III as

$$r = \frac{2\left(\frac{2}{\mu_T} + \frac{1}{\mu_L}\right)}{3\left(\frac{1}{\mu_T} + \frac{1}{\mu_L}\right)} , \tag{62}$$

and

$$s = \frac{2\left(\frac{5}{\mu_T} + \frac{4}{\mu_L}\right)}{\frac{11}{\mu_T} + \frac{7}{\mu_L}} , \tag{63}$$

where μ_L is the mass along the representative direction of the Λ critical point ([111] direction in this case). From Eqs. (62) and (63), the theoretical polarization anisotropies become $r = \frac{4}{3}$ and $s = \frac{10}{11}$ if we assume the reduced-mass relations to be $|\mu_T| \ll |\mu_L|$, $\mu_T > 0$, and $\mu_L < 0$. In this case, the experimental results are well explained. Finally, the Σ critical point may be ruled out, since it cannot explain the stress effects, as will be shown in Sec. IV A *c*. Thus, we conclude that the S_I structure is attributed to the Λ (or L) critical point with U_3 (or U_{3-}) symmetry [$\Lambda_3^v \rightarrow \Lambda_1^c$ (or $L_{3'}^v \rightarrow L_1^c$); E_1 in Si]. In addition, we conclude from the mass relation, $\mu_T \ll |\mu_L|$, that the critical point may be rather two-dimensional M_0 type ($\mu_T > 0$).

We consider the S_{II} structure next. In Fig. 6, the polarization anisotropies are found to be $|r| = 1.4 \pm 0.1$ and $|s| = 1.0 \pm 0.1$ at the positive peak of the structure. The observed results can also be com-

pared to the theoretical criteria listed in Table III. In this case, however, we cannot determine the location $\vec{K}_0$ of the critical point uniquely from the above method of symmetry analysis. Moreover, the observed polarization anisotropy ratios may be uncertain because the S_{II} structure is much interfered with the S_I structure.
The transitions $\Gamma^v_{25'} \rightarrow \Gamma^c_{15}$ and $\Delta^v_5 \rightarrow \Delta^c_1$ near the Γ point may be possible for S_{II} from the results of the band-structure calculations.[98] The symmetry location of the S_{II} structure will be discussed further in Sec. IV A *c*.

c. Uniaxial-Stress effects

Schottky-barrier ER spectra of Si for compression stresses along the [001] and [111] directions are shown in Figs. 7 and 8, respectively, with the light polarized parallel and perpendicular to the stress axis. The stress-induced energy shifts and amplitude changes are apparent in both cases. The spectra without stress are shown in Fig. 6, where the top and bottom pair of curves correspond to the [001] and [111] stress configurations, respectively.

First we analyze the S_I structure. The energy shifts of the structure for [001] and [111] stresses are shown in Figs. 9(a) and 9(b), respectively, where the energy positions of the positive and negative peaks are plotted together. In case of [001] stress, the S_I structure splits into two parts for transverse polarization, i.e., one shifts to higher energy and the other to lower energy; and, for parallel polarization, the structure shifts to lower energy without any splitting. In case of [111] stress, the shifts and the splittings of the structure are also observed, though the shifts are smaller: For perpendicular polarization the structure splits into two parts, i.e., one shifts to higher energy and the

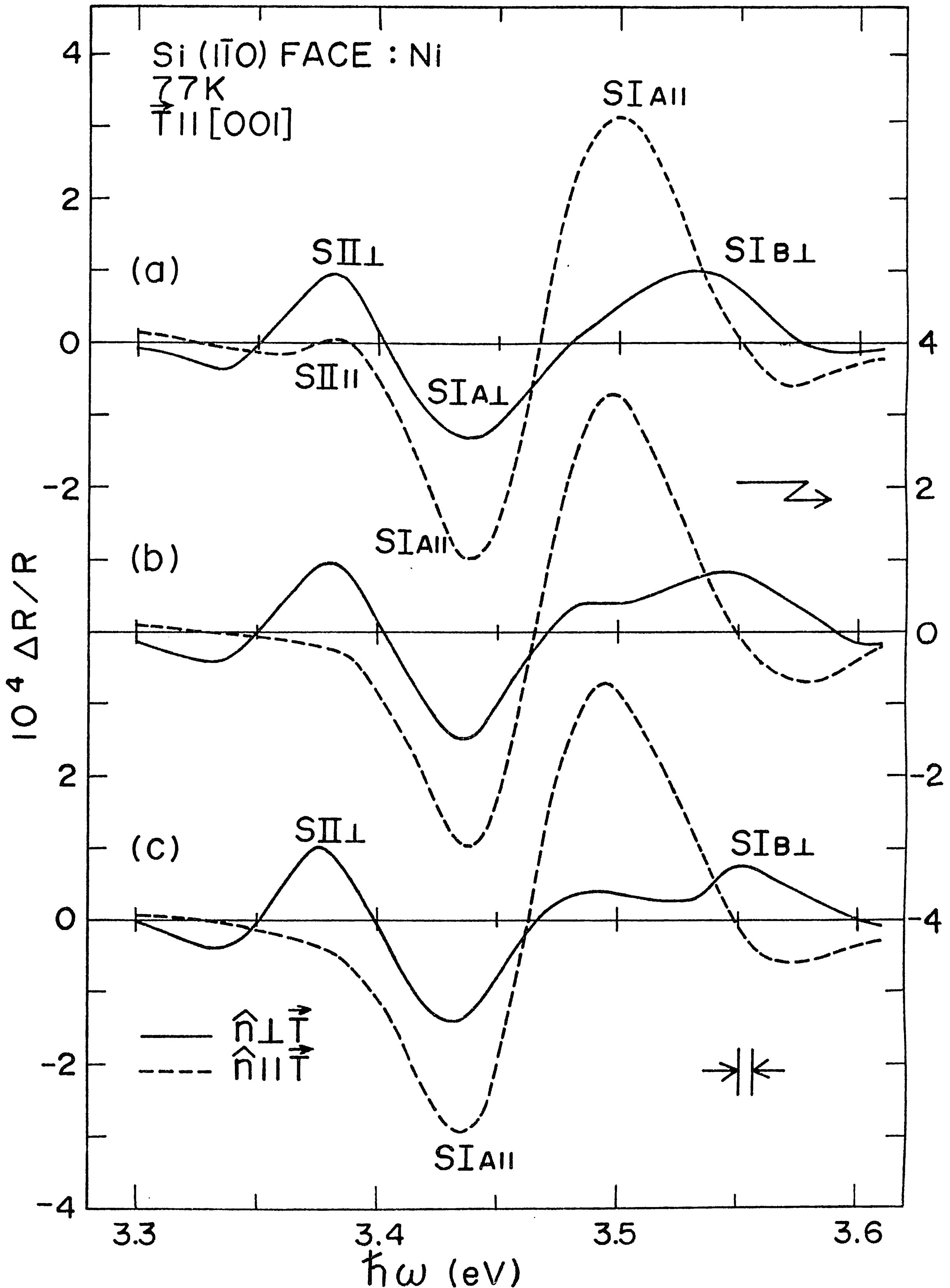

FIG. 7. Schottky-barrier ER spectra of Si for the E_0' and E_1 transitions under uniaxial (compression) stress along the [001] direction: (a) T = -3.84×10^9 dyn/cm^2; (b) T = -5.35×10^9 dyn/cm^2; (c) T = -6.97×10^9 dyn/cm^2. $S_{IA\perp}$ (or $S_{IA||}$), $S_{II\perp}$ (or $S_{II||}$), etc., are the split-off structures of S_I and S_{II} under [001] stress with perpendicular (or parallel) polarization. (After Kondo and Moritani.[31])

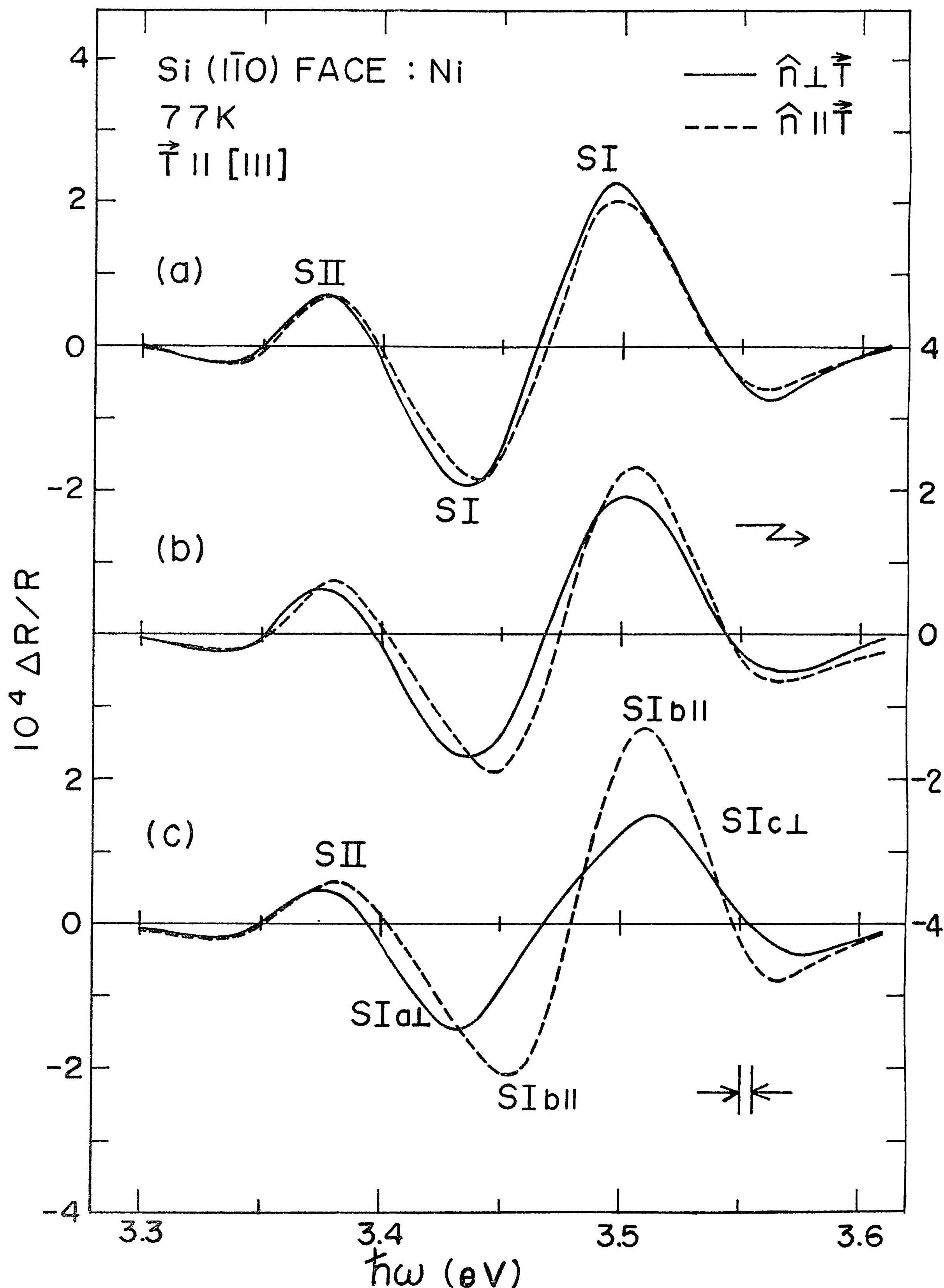

FIG. 8. Schottky-barrier ER spectra of Si for the E_0' and E_1 transitions under uniaxial (compression) stress along the [111] direction: (a) T = -1.87×10^9 dyn/cm^2; (b) T = -5.65×10^9 dyn/cm^2; (c) T = -8.78×10^9 dyn/cm^2. $S_{Ia\perp}$, $S_{Ib\parallel}$, etc., are the split-off structures of S_I under [111] stress with perpendicular and parallel polarizations. (After Kondo and Moritani.[31])

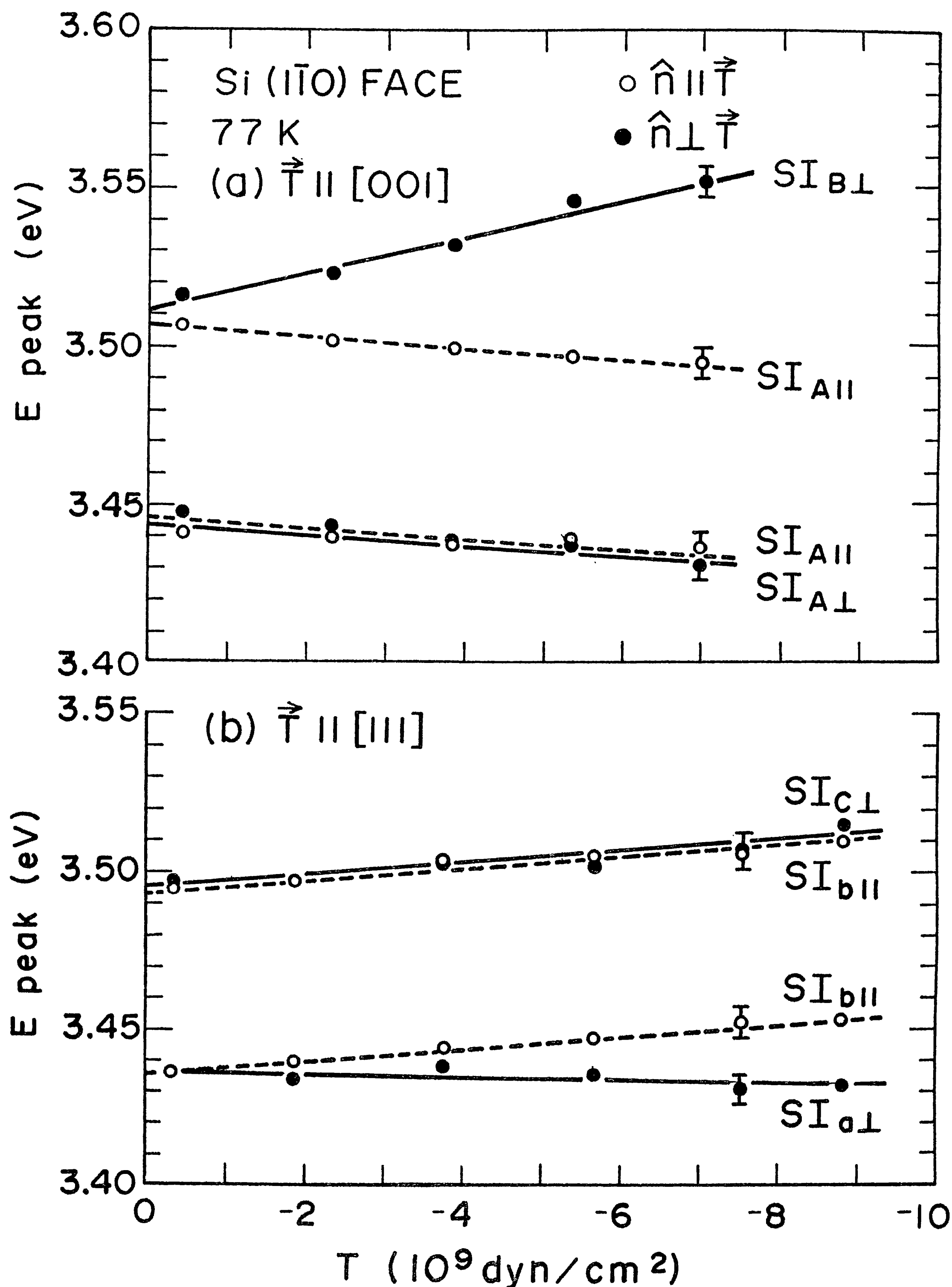

FIG. 9. Stress dependences of the peak energies of the S_I structure. The energy positions of positive and negative peaks are plotted together. (a) $\vec{T} \parallel$ [001] and (b) $\vec{T} \parallel$ [111]. Solid lines are obtained for $\hat{n} \perp \vec{T}$ and dashed lines for $\hat{n} \parallel \vec{T}$.(After Kondo and Moritani.[31])

other to lower energy; for parallel polarization the structure shifts to higher energy without any splitting. These energy shifts and splittings of the S_I structure are well explained by the stress effects of the degenerate $\Lambda_3^v - \Lambda_1^c$ or $L_{3'}^v - L_1^c$ (E_1) critical point in the following way: The uniaxial stress effects on low-field ER spectra for the $\Lambda_3^v - \Lambda_1^c$ critical point are summarized in Table V and the schematic features of the band splittings and shifts derived from Table V are shown in Fig. 10. In case of [001] stress, the U_3 (or U_{3-}) pair band splits into two parts due to intraband splitting; one component labeled A is allowed for both $\hat{n} \parallel \vec{T}$ and $\hat{n} \perp \vec{T}$, while the other component B is allowed only for $\hat{n} \perp \vec{T}$. Moreover, the relative ER form factor of the split bands for parallel and perpendicular polarizations are $F^A_{\parallel} : F^B_{\parallel} = 8 : 0$ and $F^A_{\perp} : F^B_{\perp} = 3 : 3$ with zero stress in our experimental configuration: the unit vector of the applied electric field $\hat{\mathcal{E}} = (1/\sqrt{2}, -1/\sqrt{2}, 0)$ and the effective mass relation is $\mu_T \ll |\mu_L|$. In case of [111] stress, the U_3 (or U_{3-}) pair band splits into three parts due to interband and intraband splittings: Two components labeled a and c are allowed only for $\hat{n} \perp \vec{T}$ and the other component b is allowed for both $\hat{n} \parallel \vec{T}$ and $\hat{n} \perp \vec{T}$. However, the relative ER form factor of the split bands for parallel and perpendicular polarizations are $F^a_{\parallel} : F^b_{\parallel} : F^c_{\parallel} = 0 : 80 : 0$ and $F^a_{\perp} : F^b_{\perp} : F^c_{\perp} = 54 : 7 : 27$ with zero stress. Then, the structure due to the intermediate component b is negligibly small and the two components a and c will be observed for $\hat{n} \perp \vec{T}$. We have calculated the deformation-potential parameters from the stress-induced energy shifts using the compliance constants at 77 K (in units of 10^{-12} cm^2/dyn)[99];

$$s_{11} = 0.762, \quad s_{12} = -0.213, \quad \text{and} \quad s_{44} = 1.249. \qquad (64)$$

The obtained values are listed in Table IX.

The stress-induced amplitude changes of $\Delta R/R$ are also explained by

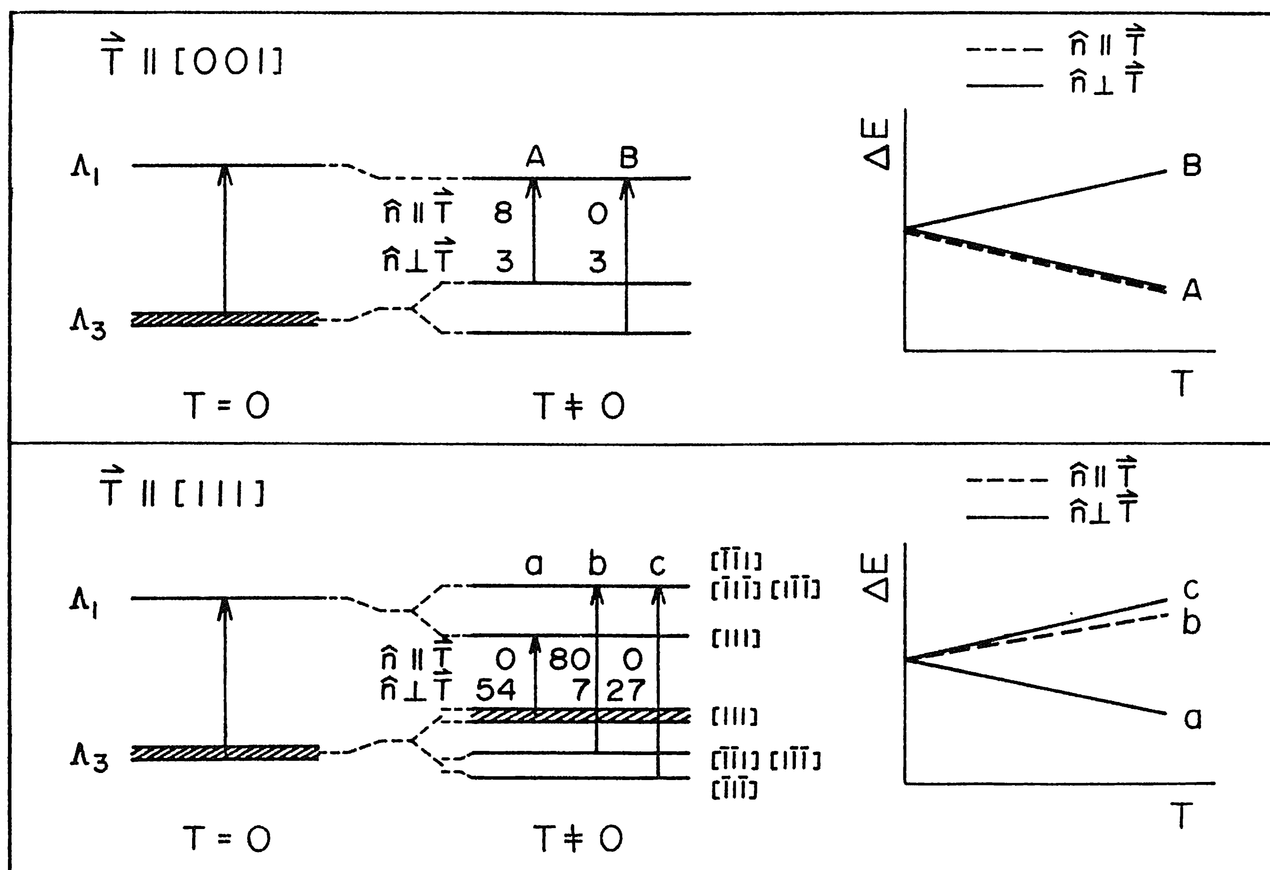

FIG. 10 . Uniaxial stress effects of the Λ_3^v valence and Λ_1^c conduction bands for stresses along the [001] and [111] directions. The relative strengths of the ER form factor F for $\hat{n} \parallel \vec{T}$ and $\hat{n} \perp \vec{T}$ configurations are given in the left side of the each arrow. Schematic diagram of the stress-induced energy shifts for the Λ_3^v - Λ_1^c critical point is given in the right hand side.

TABLE IX. Deformation potentials of the $\Lambda_3^v\,(L_{3'}^v) - \Lambda_1^c\,(L_1^c)$ critical point of Si. The previously reported values for Si and Ge are listed for comparison. Experimentally determined and calculated values of pressure coefficients of Si are also listed. RT stands for room temperature.

	This work[a]	Pollak and Rubloff[b]	Sell and Kane[c]	Pressure coefficients	
	Si (77 K)	Si (77 K)	Ge (RT)	Experiment Si	Calculated Si
D_1^1 (eV)	9.8 ± 1.3	-8 ± 1	-9.7 ± 1		
D_1^5 (eV)	6.5 ± 1.4	10 ± 2	7.5 ± 0.8		
$\mathcal{D}_3^3$ (D_3^3) (eV)	4.7 ± 0.5	5 ± 1	$2.2^{+1}_{-0.5}$		
$\mathcal{D}_3^5$ (D_3^5) (eV)	3.0 ± 1.7	4 ± 1	$1.5^{+0.6}_{-0.3}$		
$\frac{dE_g}{dP}$ (10^{-6} eV/bar)	5.7 ± 0.8			5.2 ± 0.5[d] 6.2 ± 0.4[e]	5.3 (RT)[f] 4.4[g] 5.7[h] 5.6 ± 0.6 (RT)[i] 4.8[j] 5.9[k]

[a] Reference 31.
[b] Reference 38.
[c] Reference 11.

[d] Reference 100.

[e] Reference 45.

[f] Reference 52. The conversion from their units to ours is based on the identity -1.00 eV/(unit dilatation) = 1.02×10^{-6} eV/bar for Si at room temperature.

[g] Reference 32. The conversion from their units to ours is based on the identity 1.00 eV/atm = 0.987 eV/bar.

[h] Reference 101.

[i] Reference 102. See Ref. f for the conversion from their units to ours.

[j] Reference 53.

[k] Reference 103. The conversion from their units to ours is based on the identity 1.00 eV cm^2/kg = 1.02 eV/bar.

the stress effects of the degenerate $\Lambda_3^v - \Lambda_1^c$ or $L_{3'}^v - L_1^c$ critical point. The amplitude changes of $\Delta R/R$ at the positive peaks are plotted in Figs. 11(a) and 11(b) as a function of [001] and [111] stresses, respectively. Since we observe these changes at the peak position of the structure, the observed changes consist of substantial stress-induced one and unsubstantial one due to the splitting of the structure. We find in Fig. 11(a) a large and nonlinear change for [001] stress and perpendicular polarization ($S_{IB\perp}$). It seems to be due mainly to the unsubstantial change, because the energy shifts ΔE^A and ΔE^B are relatively large in this configuration (as shown in Fig. 9(a)) and because the observed amplitude change for parallel polarization ($S_{IA||}$) is very small: The amplitude of $S_{IA||}$ and $S_{IB\perp}$ should vary with the same value but different sign as shown in Table V. From the variation of $S_{IA||}$, the optical-matrix element ratio was estimated to be $f^3/10^3 f^0 \cong 0$. This ratio shows the admixture of wave functions from the U_3 symmetry multiplet under [001] stress, and, in this case, the admixture of wave functions between the split bands may be very small. On the other hand, the amplitude changes of $\Delta R/R$ for [111] stress shown in Fig. 11(b) seem to represent the substantial changes of the optical-matrix element, because the energy shifts of the S_I structure are relatively small as shown in Fig. 9(b). The observed amplitude changes may also be explained by the equations given in Table V and we can estimate the optical-matrix element ratio to be $f^5/10^3 f^0 = -0.20 \pm 0.02$. In this case, the admixture of wave functions between the split bands may be relatively large.

The observed uniaxial-stress effects of the S_I structure described above cannot be explained by the behaviors of any Σ critical point under stress. Since all the irreducible pair bands U_1, U_2, and U_3 in the Σ direction are nondegenerate, the ER form factor F may not be changed with stress,[104] ignoring the mixing between the pair bands with different sym-

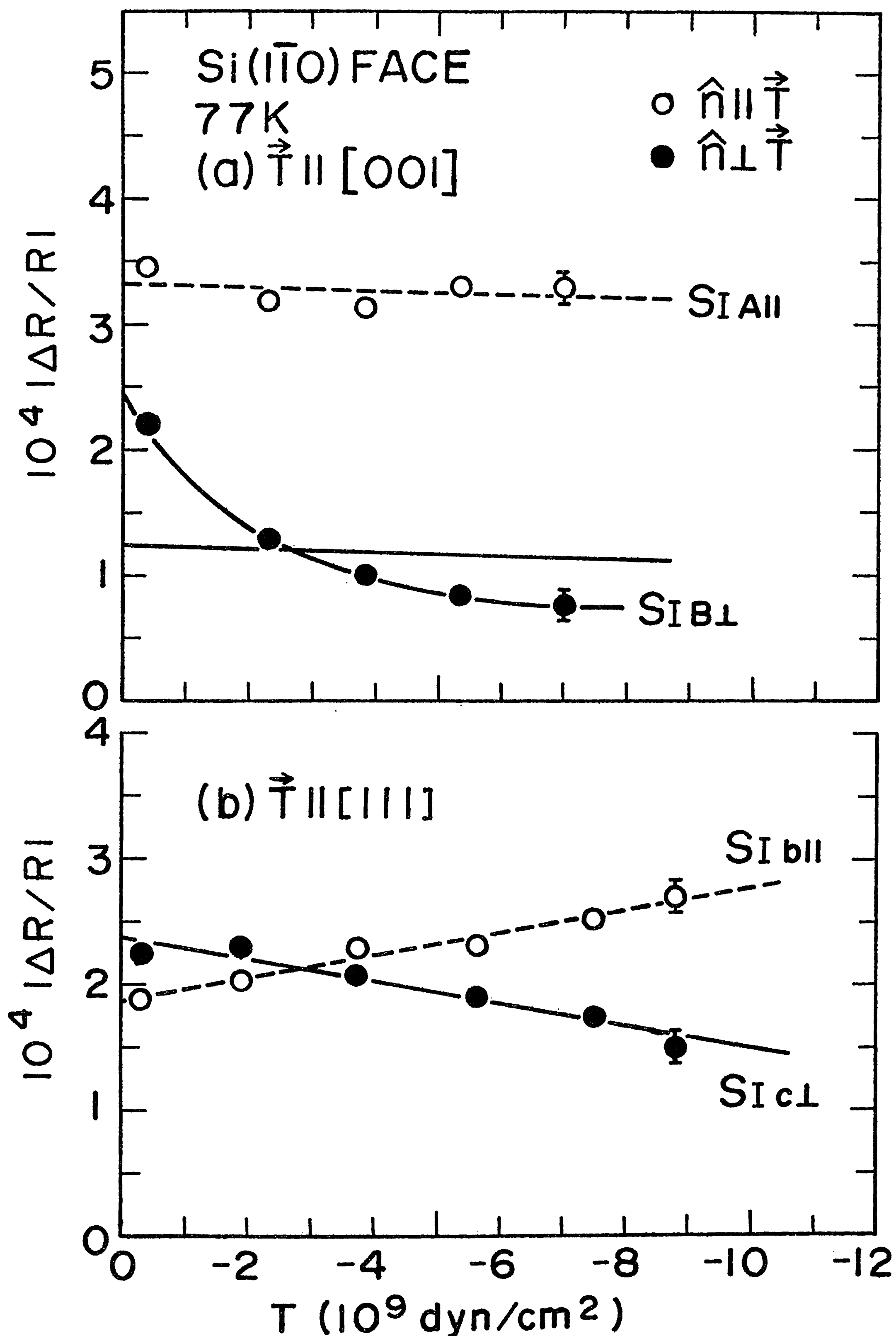

FIG. 11. Amplitude changes of the positive peak of the S_I structure as a function of uniaxial stresses along (a) the [001] direction and (b) the [111] direction. Solid lines are obtained for $\hat{n} \perp \vec{T}$ and dashed lines for $\hat{n} \parallel \vec{T}$. (After Kondo and Moritani.[31])

metries. This is apparently incompatible with the observed amplitude changes of $\Delta R/R$ with stress.

Next we consider the S_{II} structure. Figures 12(a) and 12(b) show the dependences of positive peak energy for [001] and [111] stresses, respectively. As shown in Fig. 12, the structure splits into two parts for both stress directions: The structure shifts to higher energy for parallel polarization and to lower energy for perpendicular polarization, though these shifts are very small. We also show the amplitude changes in Figs. 13(a) and 13(b) as functions of [001] and [111] stresses, respectively. It is interesting that the amplitude of $\Delta R/R$ for parallel polarization decreases as increasing the stress in the [001] direction and that the structure disappears at about 7×10^9 dyn/cm^2, while the amplitude for perpendicular polarization does not change with stress. From these results, we can obtain the information about the location $\vec{K}_0$ of the critical point related to the S_{II} structure if we assume the high-symmetry critical point. First, the Δ critical point with U_1 symmetry, the Λ (or L) critical point with U_1 (or U_{2-}) symmetry, and the Σ critical point with U_1, U_2, and U_3 symmetry may be ruled out, since these critical points are strain decoupled and, therefore, the optical matrix elements will not be changed by strain.[63] Second, the Λ (or L) critical point with U_3 (or U_{3-}) symmetry may be ruled out, since the observed energy shifts and amplitude changes of the S_{II} structure are much different from those of the S_I structure, which is attributed to the critical point with this symmetry. Third, the Γ critical point with U_{4-} symmetry ($\Gamma^v_{25'} - \Gamma^c_{15}$ in Si) may be ruled out, since the theoretical equations for the Γ transition cannot explain the amplitude changes for [001] stress: From Table VII, $(\Delta R/R)_\perp$ for [001] stress should increase by $\frac{1}{2}$ times less than $(\Delta R/R)_{||}$ if $(\Delta R/R)_{||}$ decreases. The remaining high-symmetry critical

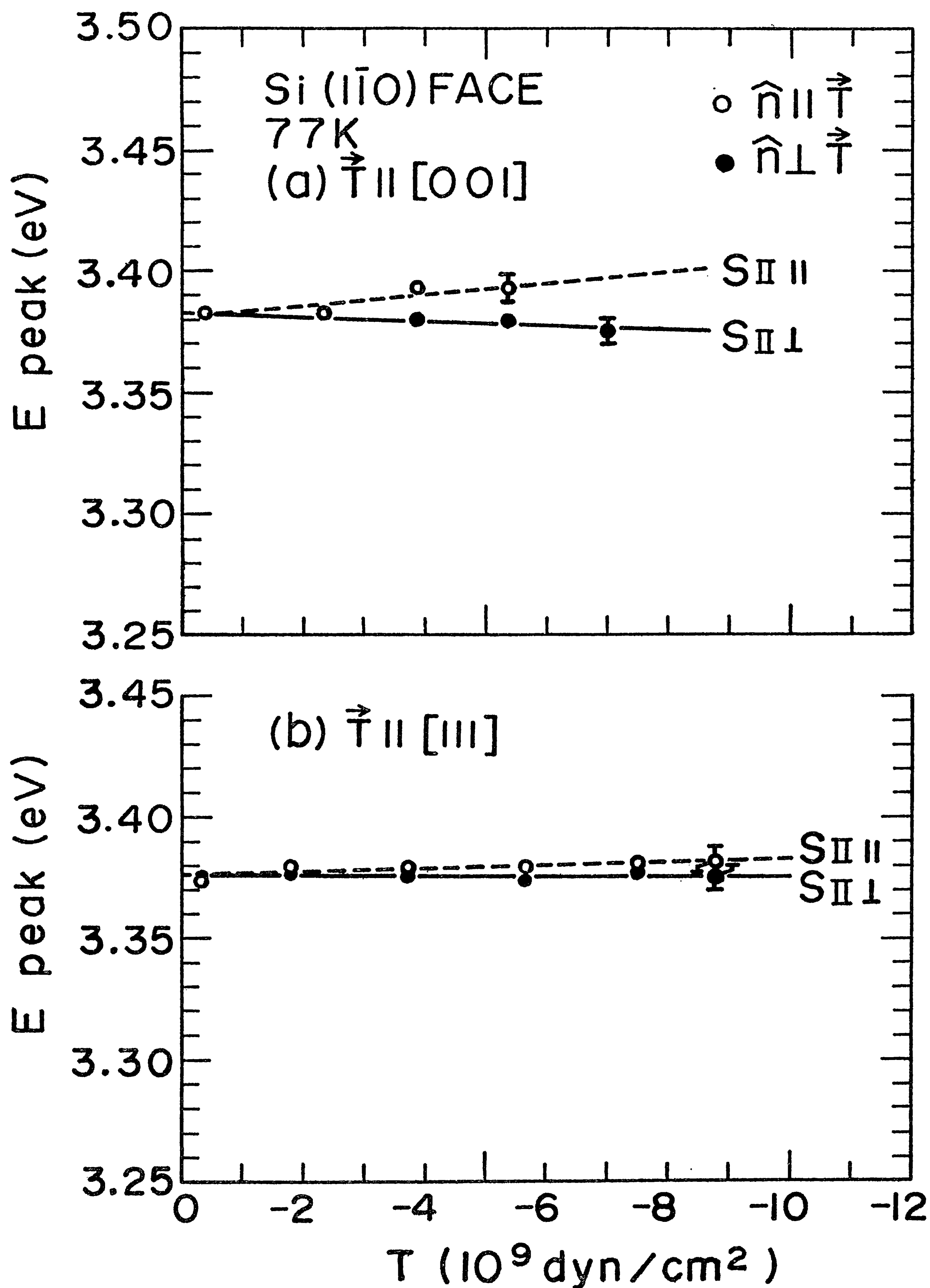

FIG. 12. Stress dependences of the peak energies of the S_{II} structure. (a) $\vec{T} \parallel [001]$ and (b) $\vec{T} \parallel [111]$. Solid lines are obtained for $\hat{n} \perp \vec{T}$ and dashed lines for $\hat{n} \parallel \vec{T}$. (After Kondo and Moritani.[31])

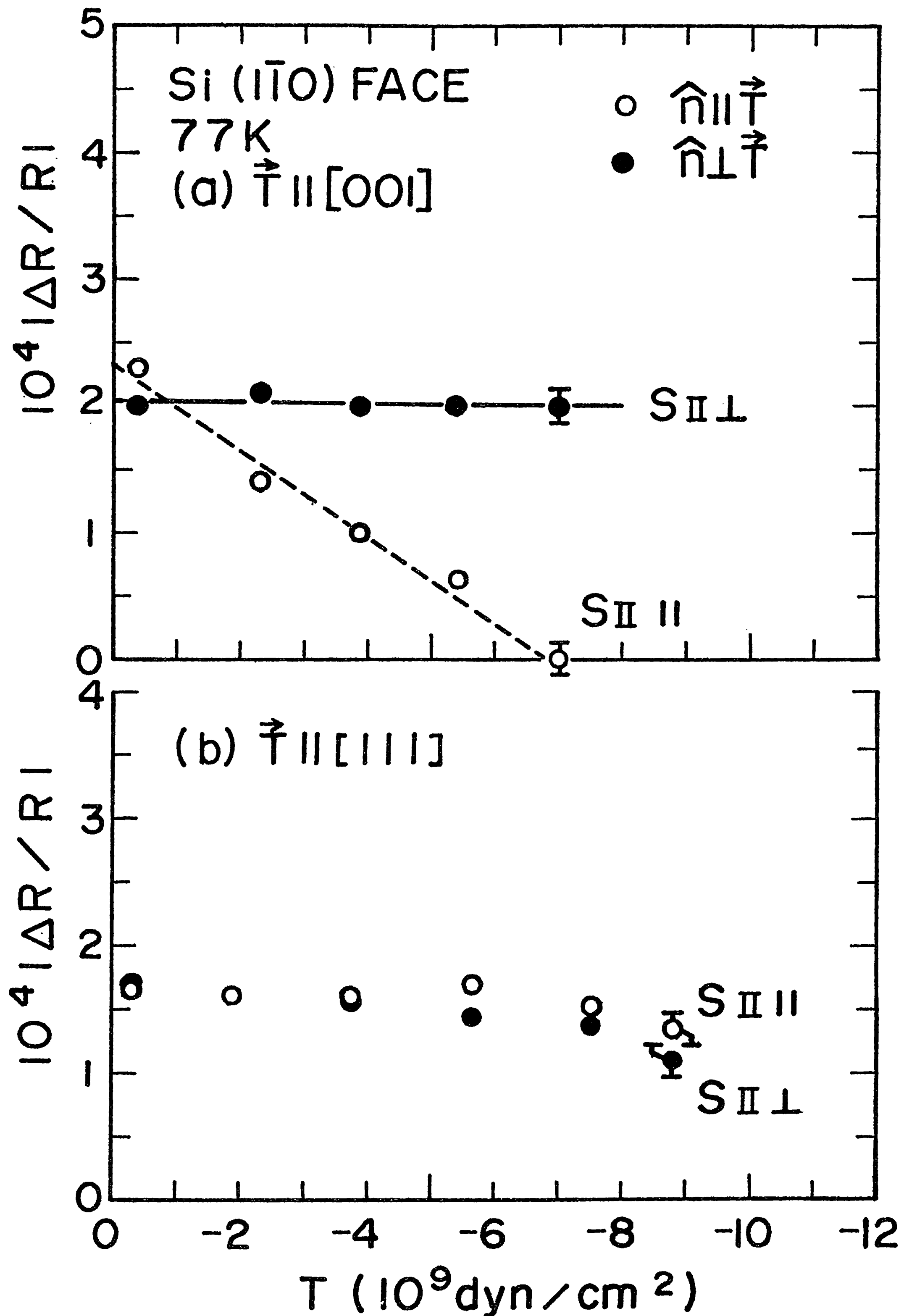

FIG. 13. Amplitude changes of the positive peak of the S_{II} structure as a function of uniaxial stresses along (a) the [001] direction and (b) the [111] direction. Solid lines are obtained for $\hat{n} \perp \vec{T}$ and dashed lines for $\hat{n} \parallel \vec{T}$. (After Kondo and Moritani.[31])

points along the Δ axis with U_5 symmetry ($\Delta_5^v \rightarrow \Delta_1^c$ near Γ in Si) are now more likely to explain the experimental results due to the manifold splittings for [001] stress as shown in Table VI. The more detailed analysis, however, is difficult, since the observed energy shifts and amplitude changes under stress are quite small. We may conclude at the present stage that the S_{II} structure is due to the Δ critical point with U_5 symmetry (E_0') if we assume high-symmetry critical points. This assignment is one of the possibilities obtained from the symmetry analysis in the absence of strain. The effective-mass relations are $\mu_T/\mu_L = 1-3$, $\mu_T > 0$, and $\mu_L > 0$ in this case.

B. E_2 Structures

a. Best-Fit Analysis

Figure 14 shows Schottky-barrier ER spectra for Si in the energy range of E_2 transitions measured at 90 K in a low-field condition. A small dip near 4.2 eV may be the structures for E_0 and $E_0 + \Delta_0$, which have been found and assigned to the $\Gamma_{8+}^v \rightarrow \Gamma_{7+}^c$ and $\Gamma_{7+}^v \rightarrow \Gamma_{7-}^c$ transitions, respectively, by Aspnes and Studna.[105] We will consider larger structures above 4.2 eV. We have performed a least-squares fit of the three-dimensional low-field resonant function (see Eq. (37)) to the observed ER spectra. The calculated results assuming the existence of two and three structures are shown in Figs. 14(a) and 14(b), respectively.

In the best-fit procedures, the Seraphin coefficients α and β of the air-Ni-Si three-phase system were used. The values of α and β at 90 K from 3.3 to 5.0 eV are shown in Fig. 15 as a parameter of the thickness of the Ni film.[106] Since β changes drastically in the energy range between 4.2 and 5.0 eV as increasing the thickness of Ni film, it is necessary to take account of this effect in order to determine the type of a

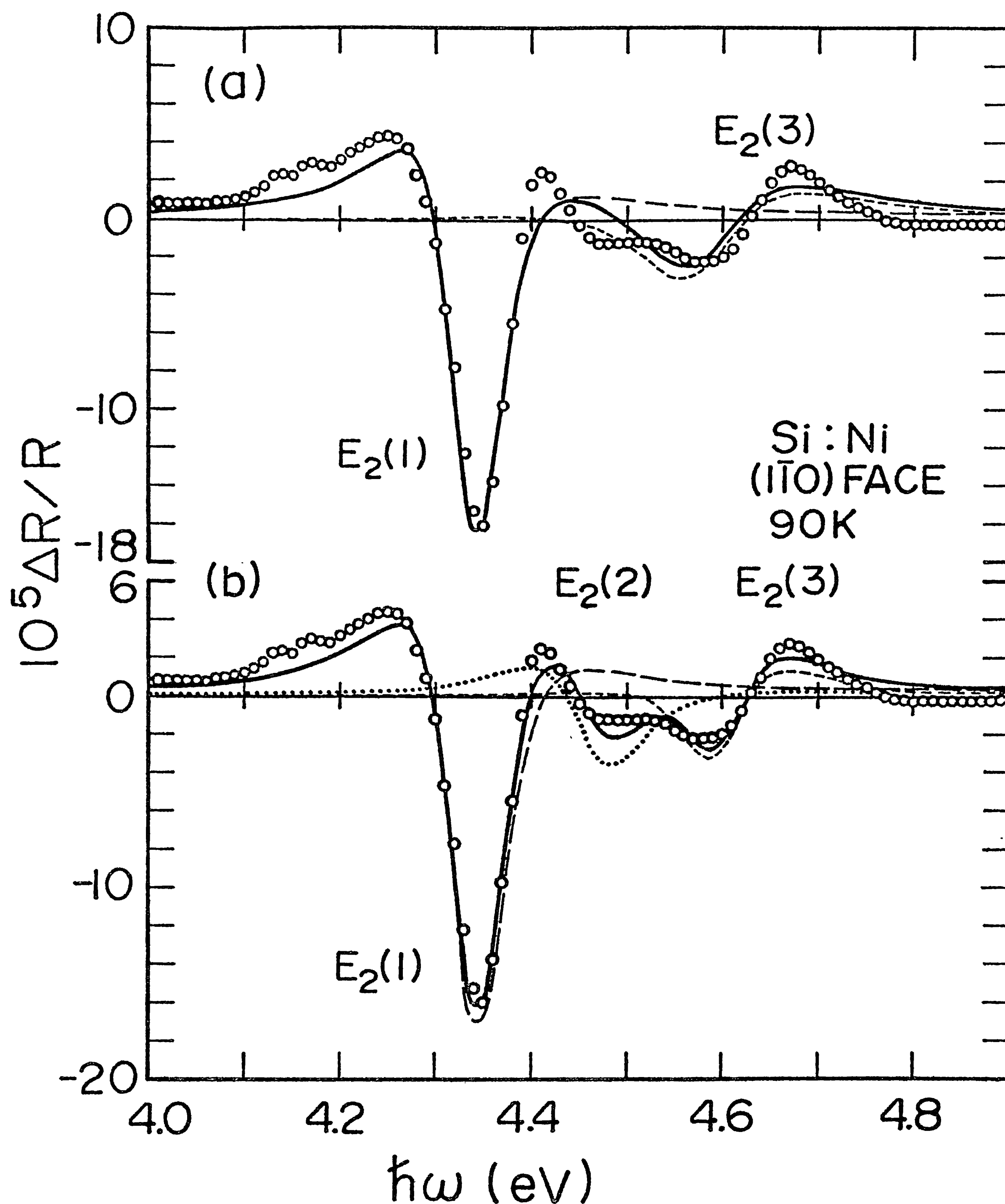

FIG. 14. Schottky-barrier ER spectrum of Si in the energy range of E_2 transitions at 90 K. Open circles are experimental results, taken on (1$\bar{1}$0) face in the low-field modulation limit. Line shapes obtained by a least-squares fit assuming the existence of (a) two and (b) three structures are also shown. Long-dashed, dotted, and short-dashed lines are the calculated three-dimensional line shapes for the $E_2(1)$, $E_2(2)$, and $E_2(3)$ structures, respectively. Solid line is the sum of the above (a) two or (b) three line shapes. (After Kondo and Moritani.[35])

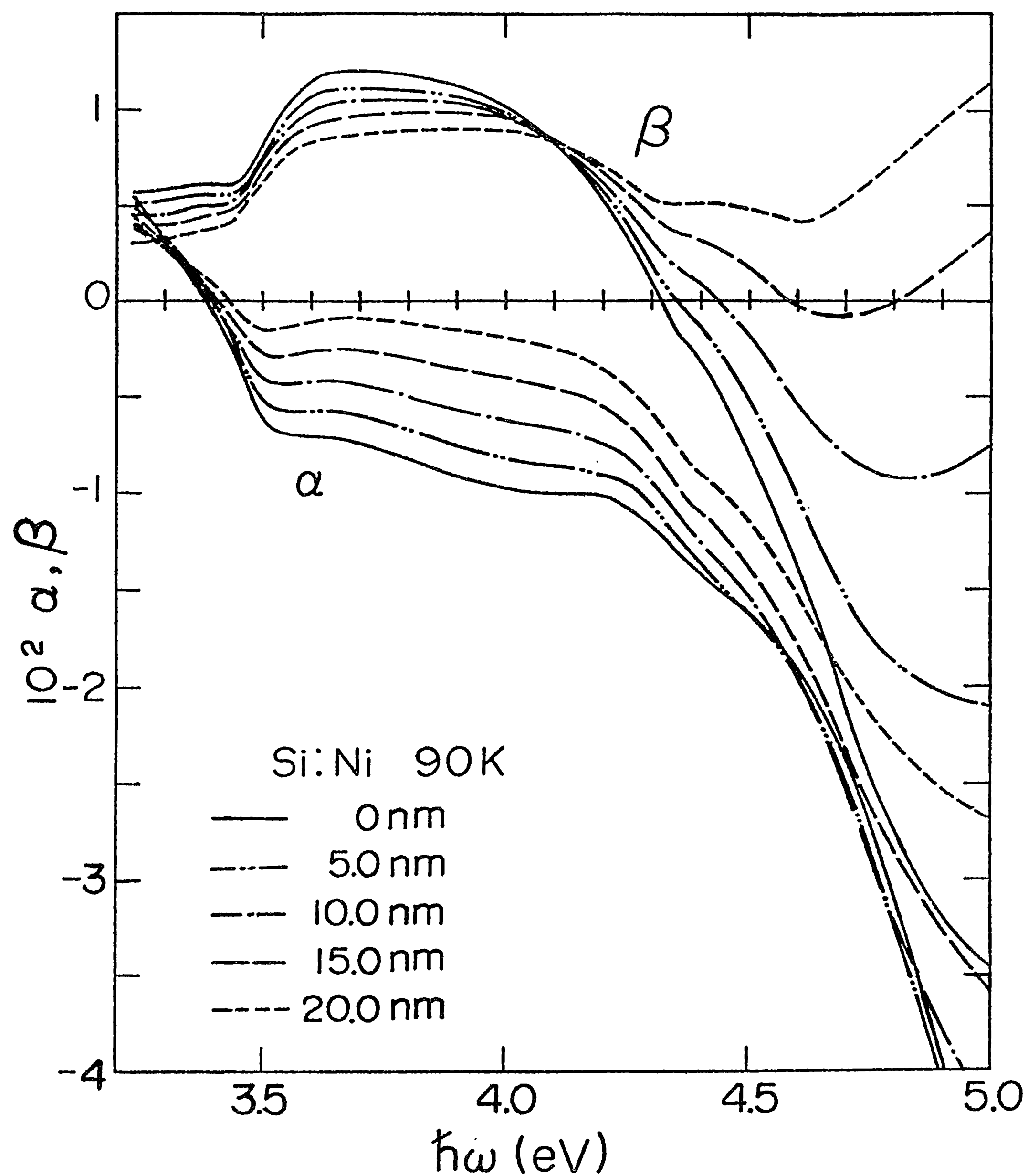

FIG. 15. Seraphin coefficients of the air-Ni-Si three-phase system at 90 K, calculated from the reflectivity spectra of Ni and Si. The results are shown with the thickness of Ni film as a parameter. (After Kondo and Moritani.[35])

critical point from the line shape. We have estimated the thickness of the Ni film to be 10 nm from the reflectivity measurements of the Ni - Si system.[88] The field inhomogeneity effect (Eq. (34)) can be neglected in our samples and the strength parameter g of the contact-exciton effect (Eq. (35)) was considered as an adjustable parameter.

Returning to Fig. 14, we can consider that three structures are concerned to this spectrum. When we assume the existence of two structures (Fig. 14(a)), the calculated line shape for the structure in the higher energy side is much broader and shifts a little to lower energy than the experimental one. In addition, the experimental line shape near 4.45 eV cannot be represented exactly by the calculated line shape. If we assume three structures in this energy region (Fig. 14(b)), the result of fit is much improved. We name the three structures $E_2(1)$, $E_2(2)$, and $E_2(3)$ from the lower-energy side. If one structure represented by the low-field resonant function corresponds to one critical point, $E_2(1)$, $E_2(2)$, and $E_2(3)$ are determined to be three-dimensional M_1, M_1, and M_2 types, respectively. The critical point parameters determined from the best fit are listed in Table X for the above two cases. As shown in Table X, the broadening parameter of the $E_2(3)$ critical point becomes more reasonable assuming the existence of three structures than two. The obtained band parameters of the $E_2(2)$ critical point may be acceptable. Moreover, the low-field ER spectra measured on samples with a rather thick Ni film (∿ 20 nm) as an electrode give an additional support of the existence of $E_2(2)$ critical point.[108]

b. Symmetry Analysis

Next we consider the symmetry assignment of the $E_2(1)$ and $E_2(3)$ critical points. The symmetry assignment of the $E_2(2)$ critical point is

TABLE X. The results of the best-fit analysis assuming the existence of two or three critical points in the E_2 spectral region. The data were taken at 90 K using the Schottky-barrier electroreflectance technique. (After Kondo and Moritani.[35])

		Two critical points	Three critical points
$E_2(1)$	E_g (eV)	4.333 ± 0.010	4.336 ± 0.010
	Γ (eV)	0.064 ± 0.010	0.066 ± 0.010
	Type	M_1^{3D}	M_1^{3D}
$E_2(2)$	E_g (eV)		4.459 ± 0.010
	Γ (eV)		0.086 ± 0.010
	Type		M_1^{3D}
$E_2(3)$	E_g (eV)	4.571 ± 0.010	4.598 ± 0.010
	Γ (eV)	0.112 ± 0.010	0.071 ± 0.010
	Type	M_2^{3D}	M_2^{3D}

difficult because of the strong interference of the $E_2(1)$ and $E_2(3)$ structures. The polarization dependences of the Schottky-barrier ER spectrum were measured for the four typical polarizations, [001], [11$\bar{2}$], [111], and [110]; and the direction of the applied electric field is [1$\bar{1}$0]. The results for the [001] and [110] polarizations are shown in Fig. 16.

We analyze the $E_2(1)$ critical point first. In this case, the polarization dependences are $(\Delta R/R)_{[110]} < (\Delta R/R)_{[111]} < (\Delta R/R)_{[11\bar{2}]} < (\Delta R/R)_{[001]}$. Since polarization dependences must be independent of spectral position, we obtain the ratio $|r| = (\Delta R/R)_{[001]}/(\Delta R/R)_{[110]} = 1.35 \pm 0.16$ and $|s| = (\Delta R/R)_{[111]}/(\Delta R/R)_{[11\bar{2}]} = 0.91 \pm 0.11$ at the negative peak of the structure. The combination of the observed polarization anisotropies and the type of the critical point (M_1) can be compared to the theoretical criteria for high-symmetry critical points listed in Table III. We consider only critical points along the Σ and Δ axes near the X point, since the critical points of these symmetry may contribute to the E_2 structures as a result of the energy band-structure calculations[3,47,49,52,60] and the other high-symmetry critical points at Γ and along Λ (or at L) are immediately ruled out: The Γ critical point ($\Gamma^v_{25'} \to \Gamma^c_{15}$, $\Gamma^v_{25'} \to \Gamma^c_{15}$, etc., in Si) will show an isotropic polarization dependence. The Λ ($\Lambda^v_3 \to \Lambda^c_1$ in Si) or L ($L^v_{3'} \to L^c_1$ in Si) critical point is assigned to the S_I structure in the 3.4 eV region and no other high-energy critical points may exist along the Λ axis or at the L point due to the flatness of the $\Lambda^v_3 - \Lambda^c_1$ interband differences ($\mu_T << |\mu_L|$), as shown in Sec. IV A. For the $\Sigma^v_2 \to \Sigma^c_3$ critical point (U_2 symmetry), the polarization anisotropies may be written from Table III as

$$r = \frac{2\left(\frac{1}{\mu_{T2}} + \frac{1}{\mu_L}\right)}{\frac{2}{\mu_{T1}} + \frac{1}{\mu_{T2}} + \frac{1}{\mu_L}} , \qquad (65)$$

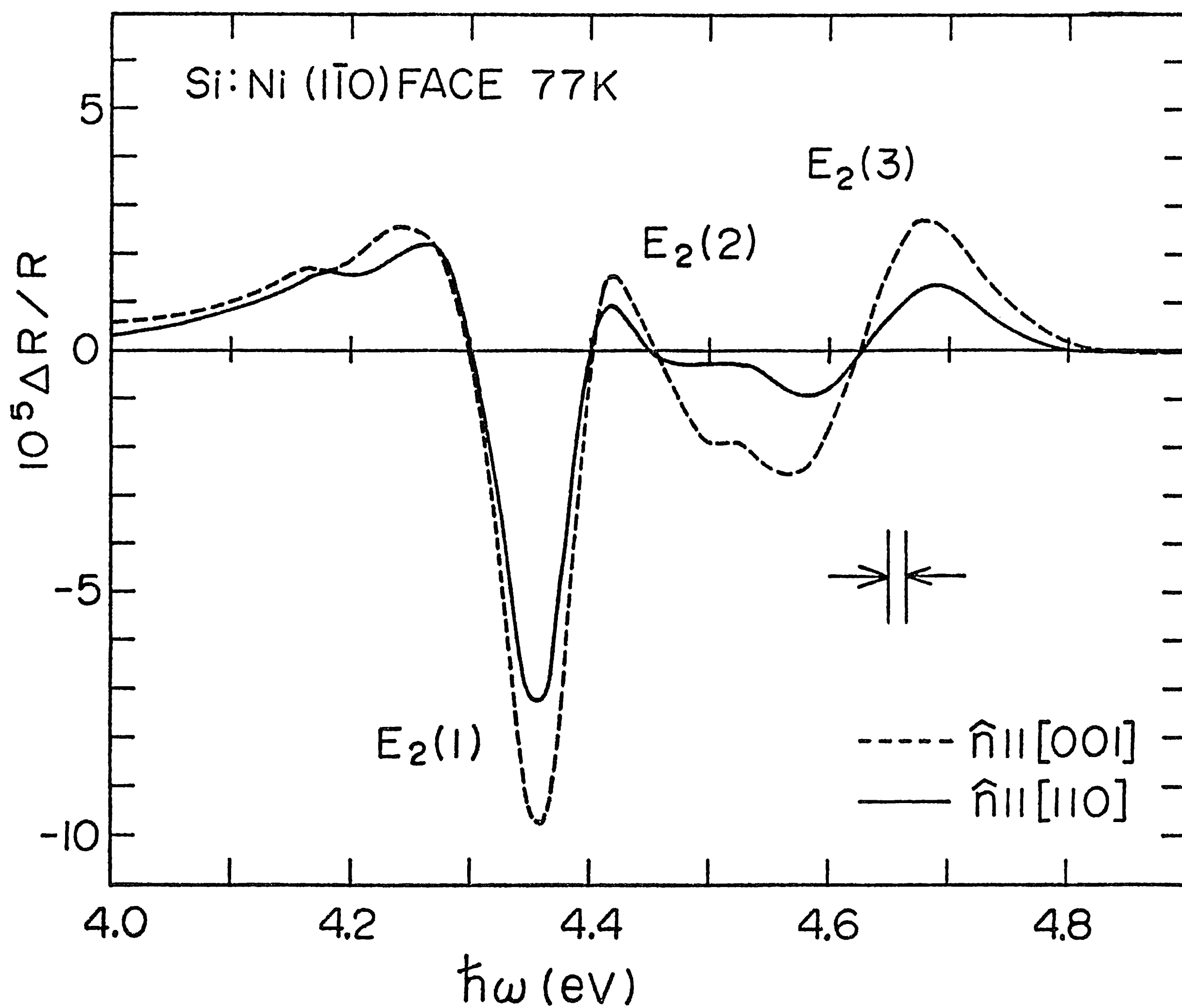

FIG. 16. Polarization anisotropy of the Schottky-barrier ER spectrum of Si in the energy range of E_2 transitions. Data are taken on (1$\bar{1}$0) face at 77 K in the low-field modulation limit. Solid line is the spectrum for $\hat{n} \parallel [110]$ and dashed line for $\hat{n} \parallel [001]$. (After Kondo and Moritani.[35])

and

$$s = \frac{4(\frac{1}{\mu_{T1}} + \frac{1}{\mu_{T2}} + \frac{1}{\mu_L})}{\frac{2}{\mu_{T1}} + \frac{5}{\mu_{T2}} + \frac{5}{\mu_L}}, \qquad (66)$$

where μ_L is the mass along the representative direction of the Σ critical point ([110] direction in this case). If we assume the relation, $1/\mu_{T2} + 1/\mu_L = 4/\mu_{T1}$, $\mu_{T1} > 0$, and $\mu_{T2}\mu_L < 0$, in Eqs. (65) and (66), the calculated polarization anisotropies become $r = \frac{4}{3}$ and $s = \frac{10}{11}$ and the effective-mass relation shows the M_1 type, which explain the experimental results. On the other hand, the critical points at X and along Δ, i.e., $X_4^v \rightarrow X_1^c$ (U_{5-} symmetry; $\mu_T = 3\mu_L$, $\mu_T > 0$, $\mu_L > 0$),[109] $\Delta_{2'}^v \rightarrow \Delta_{2'}^c$ (U_1 symmetry; $\mu_L = 2\mu_T$, $\mu_T > 0$, $\mu_L > 0$), and $\Delta_5^v \rightarrow \Delta_1^c$ or $\Delta_5^v \rightarrow \Delta_{2'}^c$ (U_5 symmetry; $\mu_T = 3\mu_L$, $\mu_T > 0$, $\mu_L > 0$), are ruled out, because they must be of type M_0 in order to explain the observed polarization anisotropies. Although the other critical points along Σ, i.e., $\Sigma_1^v \rightarrow \Sigma_1^c$ or $\Sigma_3^v \rightarrow \Sigma_3^c$ (U_1 symmetry; $2/\mu_{T1} + 1/\mu_L = 7/\mu_{T2}$, $\mu_{T2} > 0$, $\mu_{T1}\mu_L < 0$), and $\Sigma_1^v \rightarrow \Sigma_3^c$ (U_3 symmetry; $2/\mu_{T1} + 1/\mu_{T2} = 7/\mu_L$, $\mu_L > 0$, $\mu_{T1}\mu_{T2} < 0$), may be possible, they are not practical as compared with $\Sigma_2^v \rightarrow \Sigma_3^c$ in this energy region. Thus we conclude that the $E_2(1)$ critical point is attributed to the $\Sigma_2^v \rightarrow \Sigma_3^c$ transition.

We analyze the $E_2(3)$ critical point next. The polarization dependences are $(\Delta R/R)_{[110]} < (\Delta R/R)_{[111]} < (\Delta R/R)_{[11\bar{2}]} < (\Delta R/R)_{[001]}$. We obtain the polarization anisotropies $|r| = 2.0 \pm 1.0$ and $|s| = 0.8 \pm 0.4$ at the positive peak of the structure. In this case, the symmetry is not determined uniquely: $\Delta_{2'}^v \rightarrow \Delta_{2'}^c$ (U_1 symmetry; $|\mu_T| << \mu_L$, $\mu_T < 0$, $\mu_L > 0$), $\Delta_5^v \rightarrow \Delta_1^c$ or $\Delta_5^v \rightarrow \Delta_{2'}^c$ (U_5 symmetry; $\mu_L << |\mu_T|$, $\mu_T < 0$, $\mu_1 > 0$), $X_4^v \rightarrow X_1^c$ (U_{5-} symmetry; $\mu_L << |\mu_T|$, $\mu_T < 0$, $\mu_L > 0$), $\Lambda_3^v \rightarrow \Lambda_1^c$ or $L_{3'}^v \rightarrow L_1^c$ (U_3 or U_{3-} symmetry; $\mu_L = 2|\mu_T|$, $\mu_T < 0$, $\mu_L > 0$), $\Sigma_1^v \rightarrow \Sigma_1^c$ or $\Sigma_3^v \rightarrow \Sigma_3^c$ (U_1 symmetry; $|\mu_{T1}|$ and $|\mu_L| << \mu_{T2}$, $\mu_{T1} < 0$, $\mu_{T2} > 0$, $\mu_L < 0$), $\Sigma_2^v \rightarrow \Sigma_3^c$ (U_2 symmetry;

$|\mu_{T2}|$ and $|\mu_L| << \mu_{T1}$, $\mu_{T1} > 0$, $\mu_{T2} < 0$, $\mu_L < 0$), and $\Sigma_1^v \rightarrow \Sigma_3^c$ (U_3 symmetry; $|\mu_{T1}|$ and $|\mu_{T2}| << \mu_L$, $\mu_{T1} < 0$, $\mu_{T2} < 0$, $\mu_L > 0$) may be possible: The polarization anisotropies become r = 2 and s = 0.8 and the effective-mass relation shows the M_2 type. The $\Delta_5^v \rightarrow \Delta_1^c$, $X_4^v \rightarrow X_1^c$, $\Lambda_3^v \rightarrow \Lambda_1^c$, $L_{3'}^v \rightarrow L_1^c$, and $\Sigma_2^v \rightarrow \Sigma_3^c$ among the above transitions are ones between the highest-valence and the lowest-conduction bands. Therefore, we believe that the $\Delta_5^v \rightarrow \Delta_1^c$ transition near the X point is more practical for the $E_2(3)$ critical point. In this case, we find from the mass relation, $\mu_L << |\mu_T|$, that the critical point is rather one-dimensional.

The symmetry assignment of the $E_2(3)$ critical point may not be conclusive, because we have assumed critical points to be at (or along) high-symmetry points (or axes) in the symmetry analysis: An M_2 critical point at $(\frac{13}{24}, \frac{1}{4}, \frac{1}{4})$ in the ΓXUL plane predicted by Saravia and Brust[49] may be possible. However, it is difficult to evaluate this possibility by this method of symmetry analysis.

V. SYNTHESIS

Interband-energy contours in the reduced Brillouin zone[110] can be constructed from the experimentally obtained optical-critical-point set.[111] First, the $\vec{k}$ dependences of the interband energy in the vicinity of critical point may be written in the parabolic form as shown in Eq. (22)

$$E^{\tau}(\vec{k}) = E_g^{\tau} + \frac{\hbar^2}{2}\left[\frac{(k_{T1}-K_{0,T1})^2}{\mu_{T1}} + \frac{(k_{T2}-K_{0,T2})^2}{\mu_{T2}} + \frac{(k_L-K_{0,L})^2}{\mu_L}\right]. \quad (22)$$

Then, we can describe the interband-energy contours in the vicinity of critical point if we know the energy E_g, the location $\vec{K}_0$ in the Brillouin zone, and the relation among the interband-reduced masses μ_{T1}, μ_{T2}, μ_L. Second, we assemble the critical points obtained experimentally and connect them as smooth curves with regard to their topological relations.

We construct the $E_{4-5}(\vec{k})$ energy contours of Si in the reduced Brillouin zone. The first Brillouin zone of diamond lattice is shown in Fig. 17. The $\vec{k}$ dependences of the experimentally obtained optical-critical points are as follows:

E_0' : $\vec{K}_0 = \langle 0, 0, k_0\rangle$; $\Delta_5^v \rightarrow \Delta_1^c$ near the Γ point,

$$E^{\tau 0'}(\vec{k}) = E_g^{\tau 0'} + \frac{\hbar^2}{2}\left[\frac{(k_T-K_{0,T})^2}{|\mu_T|} + \frac{(k_L-K_{0,L})^2}{|\mu_L|}\right], \quad (67)$$

$\mu_T/\mu_L = 1-3$, $\mu_T > 0$, $\mu_L > 0$.

E_1 : $\vec{K}_0 = \langle k_0, k_0, k_0\rangle$; $\Lambda_3^v \rightarrow \Lambda_1^c$ or $L_{3'}^v \rightarrow L_1^c$,

$$E^{\tau 1}(\vec{k}) = E_g^{\tau 1} + \frac{\hbar^2}{2}\left[\frac{(k_T-K_{0,T})^2}{|\mu_T|} - \frac{(k_L-K_{0,L})^2}{|\mu_L|}\right], \quad (68)$$

$\mu_T \ll |\mu_L|$, $\mu_T > 0$, $\mu_L < 0$.

$E_2(1)$: $\vec{K}_0 = \langle k_0, k_0, 0\rangle$; $\Sigma_2^v \rightarrow \Sigma_3^c$,

$$E^{\tau 2(1)}(\vec{k}) = E_g^{\tau 2(1)} + \frac{\hbar^2}{2}\left[\frac{(k_{T1} - K_{0,T1})^2}{|\mu_{T1}|} - \frac{(k_{T2} - K_{0,T2})^2}{|\mu_{T2}|} + \frac{(k_L - K_{0,L})^2}{|\mu_L|}\right], \quad (69)$$

$1/\mu_{T2} + 1/\mu_L = 4/\mu_{T1}$, $\mu_{T1} > 0$, $\mu_{T2} < 0$, $\mu_L > 0$, in this case.

$E_2(3)$: $\vec{K}_0 = \langle 0, 0, k_0\rangle$; $\Delta_5^v \rightarrow \Delta_1^c$ near the X point,

$$E^{\tau 2(3)}(\vec{k}) = E_g^{\tau 2(3)} + \frac{\hbar^2}{2}\left[-\frac{(k_T - K_{0,T})^2}{|\mu_T|} + \frac{(k_L - K_{0,L})^2}{|\mu_L|}\right], \quad (70)$$

$\mu_L \ll |\mu_T|$, $\mu_T < 0$, $\mu_L > 0$.

The $E_{4-5}(\vec{k})$ energy contours in the ΓKWX, ΓKL, and ΓXUL planes constructed from Eq. (67) through (70) are shown in Fig. 18. This figure well explains the topological features of the optical-critical points of Si in the energy range from 3.0 to 5.0 eV. The shaded areas around the Γ point (E_0') show that the M_0^{3D} critical point on the Δ axis or some critical-point set exists in this region (see Sec. VI A). The E_1 critical point (M_1^{3D} type) is put at the L point and the contour lines near E_1 are written to be nearly flat along the Λ axis due to the relation $\mu_T \ll |\mu_L|$. There is the $E_2(1)$ critical point (M_1^{3D} type) on the Σ axis; the case $\mu_{T1} > 0$, $\mu_{T2} < 0$, and $\mu_L > 0$ is written in this figure in connection with the $E_2(3)$ critical point (M_2^{3D} type) on the Δ axis, in which the contour lines near $E_2(3)$ are written to be nearly flat in the directions transverse to Δ near the X point due to the relation, $\mu_L \ll |\mu_T|$. Note, however, that the exact positions of the critical points along the symmetry axes and the accurate shapes of the contour lines are not important in this figure.

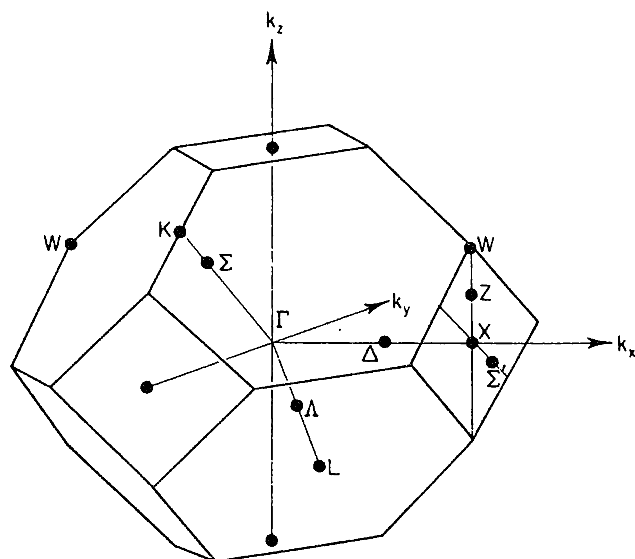

FIG. 17. The first Brillouin zone of diamond lattice showing the symmetry points and axes.

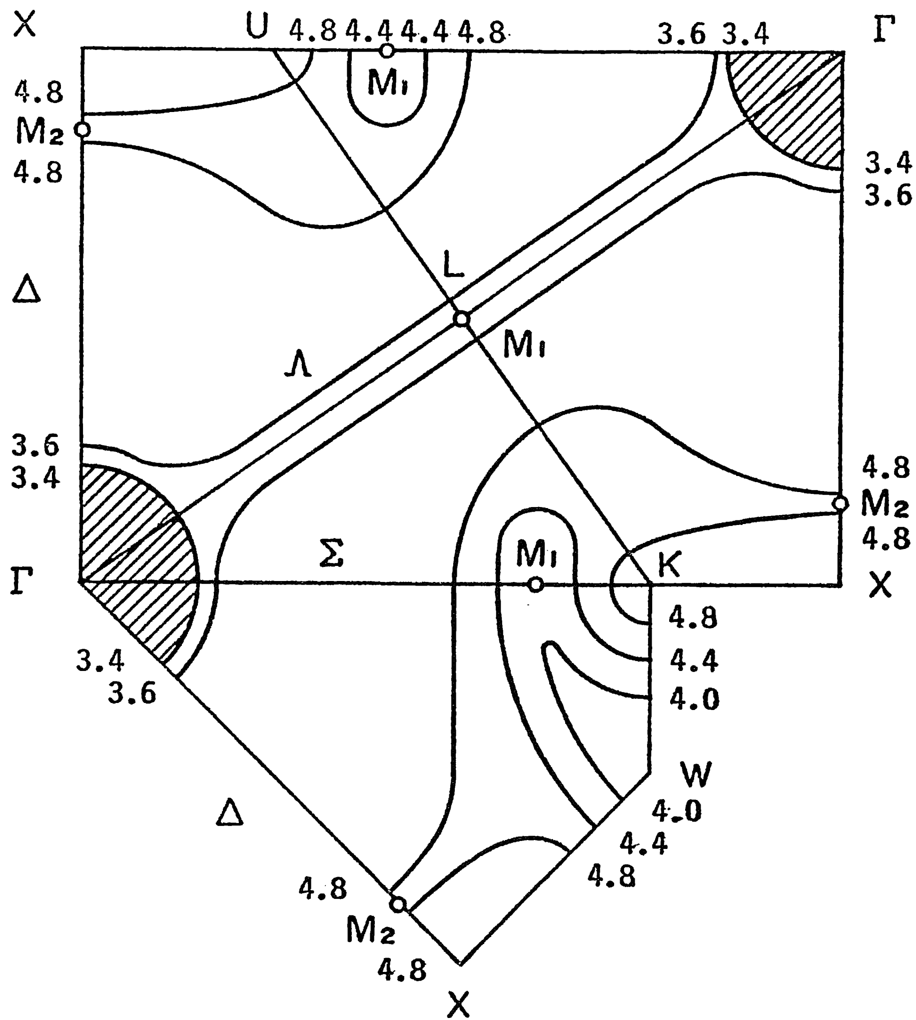

FIG. 18. The $E_{4-5}(\vec{k})$ energy contours of Si in the ΓKWX, ΓKL, and ΓXUL planes constructed from the experimental results (in eV). The critical points (c.p.) listed in this figure are as follows: E_0' : M_0^{3D} c.p. on the Δ axis near the Γ point ($\mu_T/\mu_L = 1-3$, $\mu_T > 0$, $\mu_L > 0$) or some c.p. set around the Γ point; E_1: M_1^{3D} c.p. at the L point ($\mu_T \ll |\mu_L|$, $\mu_T > 0$, $\mu_L < 0$); E_2: M_1^{3D} c.p. on the Σ axis ($1/\mu_{T2} + 1/\mu_L = 4/\mu_{T1}$, $\mu_{T1} > 0$, $\mu_{T2} < 0$, $\mu_L > 0$, in this case); and M_2^{3D} c.p. on the Δ axis near the X point ($|\mu_T| \gg \mu_L$, $\mu_T < 0$, $\mu_L > 0$). (After Kondo and Moritani.[111])

VI. DISCUSSION

A. E_0' and E_1 Structures

The experimental results obtained from the line-shape analysis in this spectral region are summarized in Table VIII, together with the data previously obtained with other modulation techniques. The critical-point energy and the phenomenological broadening energy can now be determined very accurately from ER line shapes; these values are estimated by Aspnes's three-point method[20,23] and more precisely by a method of least-squares fit. When two or more structures interfere with each other, however, which is usually seen in the higher-energy region, the best-fit analysis becomes more complicated. Our results of the 3.4 eV structures of Si disagree in some points with the results obtained by Grover and Handler[43] using the electrolyte ER technique in the flatband condition. The values of the critical-point energies determined in this work are somewhat larger than those determined by Grover and Handler. This is probably due to the difference between the line-shape functions used in the best-fit analysis (the two-dimensional electro-optic F and G functions[75] in their work and the low-field resonant functions[19,23] in this work), and also due to the large broadening effects in such a high-energy region. Moreover, Grover and Handler have shown that the main strucutre in the 3.4 eV region is attributed to the two-dimensional M_0 critical point along the Λ axis and the weak structure in the lower-energy side to the three-dimensional M_1 critical point. The former result is consistent with our result but the latter one is somewhat strange as was pointed out in their own paper. On this point, Seraphin and Bottka[40] have shown in their pioneering work that the weak structure is due to the three-dimensional M_0 critical point. This is in agreement with our results. Moreover, the results obtained by other authors listed in Table VIII agree with our results.

The 3.4 eV complexities of Si have been the origin of some controversy for a long time, as described in Sec. I. Pollak and Rubloff[38] have shown that the main structure is attributed to the $\Lambda_3^v \rightarrow \Lambda_1^c$ or $L_{3'}^v \rightarrow L_1^c$ transition from the uniaxial-stress effects on the wavelength-modulated reflectivity spectra. They also pointed out that the weak structure in the lower-energy side is due to the Δ critical point near the Γ point. Their assignments are in good agreement with our results of the symmetry analysis. The assignments are also supported by the results of the composition dependence of the Ge - Si alloy system reported by Kline et al.[112] They have found that the E_1 and E_0' doublets of Ge merge into the 3.4 eV structures of Si, indicating that both the Λ and Δ transitions may be responsible for this energy region.

Our measurements can also be compared to the energy-band-structure calculations of Si. The representative results are listed in Table XI. In the theoretical calculations, the relative position of the energy levels rather than their precise values may be important, and the results calculated by Herman et al.,[52] Dresselhaus and Dresselhaus,[48] Sravia and Brust,[49] Van Vechten,[115] Zucca et al.,[50] Kane,[114] and Van Dyke (orthogonalized plane wave)[116] may be consistent with our experimental results for the structures in the 3.4 eV energy region. It has been pointed out by Kane,[47] and by Saravia and Brust,[49] that the Λ_3 valence and the Λ_1 conduction bands of Si are nearly parallel from the Γ point to the L point The reduced-mass relations $\mu_T << |\mu_L|$, $\mu_T > 0$, and $\mu_L < 0$ at the $\Lambda_3^v - \Lambda_1^c$ (or $L_{3'}^v - L_1^c$) critical point obtained from the polarization anisotropies of the low-field ER spectra verify these situations.

The deformation-potential parameters determined from the stress effects of the $\Lambda_3^v - \Lambda_1^c$ (or $L_{3'}^v - L_1^c$) critical point are summarized in Table IX, together with other experimental results of Si and Ge. The

TABLE XI. Calculated critical-point energies of Si in the E_0' and E_1 spectral region (in eV).

Transition	Brust[a]	Cohen and Bergstresser[b]	Kane[c,d] 1966	Kane[c,d] 1971	Herman et al.[e] E (PERT)	Herman et al.[e] E (PERT)	Herman et al.[e] E (PERT)	Dresselhaus and Dresselhaus[f]
$\Gamma^v_{25'} \rightarrow \Gamma^c_{15}$	3.4	3.4	3.2	2.98	2.8	2.75	2.7	2.43
$\Lambda^v_3 \rightarrow \Lambda^c_1$	3.15	3.1	2.9	3.01	3.1	3.3	3.5	3.22
$L^v_{3'} \rightarrow L^c_1$					3.0	3.2	3.4	3.20
$\Delta^v_5 \rightarrow \Delta^c_1$					3.3	3.35	3.4	

Transition	Saravia and Brust[g] I	II	III	IV	Van Vechten[h]	Stukel and Euwema[i]	Zucca et al.[j]	Van Dyke[k] OPW	Van Dyke[k] Pseudo
$\Gamma^v_{25'} \rightarrow \Gamma^c_{15}$	3.44	3.39	3.34	3.39	3.40	2.79		3.01	3.15
$\Lambda^v_3 \rightarrow \Lambda^c_1$	3.13	3.37	3.60	3.33	3.60	2.78	3.13	3.08	3.11
$L^v_{3'} \rightarrow L^c_1$	3.49	3.54					3.46		
$\Delta^v_5 \rightarrow \Delta^c_1$	3.42	3.49	3.54			3.33	3.42		

[a] Reference 3.
[b] Reference 113.
[c] Reference 47.
[d] Reference 114.
[e] Reference 52.
[f] Reference 48.
[g] Reference 49.
[h] Reference 115.
[i] Reference 102.
[j] Reference 50.
[k] Reference 116.

values of the deformation parameters D_1^1 and $\mathcal{D}_3^3$ determined from measurements under [001] stress are in good agreement with those determined by Pollak and Rubloff.[38] However, the values of D_1^5 and $\mathcal{D}_3^5$ determined from measurements under [111] stress are smaller than those determined by them. It is probably due to the fact that our values were obtained in relatively low-stress region, while their values were obtained in high-stress region. These four values obtained in this work are in agreement with those determined by Sell and Kane[11] for the E_1 structure of Ge, which may be due to the analogy of the crystal structure between Si and Ge.
The pressure coefficient dE/dP is calculated from the pair-band hydrostatic-deformation parameter D_1^1 in the form

$$\frac{dE}{dP} = - \sqrt{3}\, D_1^1 (s_{11} + 2s_{12}), \tag{71}$$

and the value determined in this work is also listed in Table IX, together with previously reported experimental and calculated results for comparison. We find good agreement between our value and the other experimental and calculated values within the limit of our experimental errors.

We wish to point out the possibility that the weak S_{II} (E_0') structure is contributed by the critical point located at different points and axes or by some critical-point set located at different points in the Brillouin zone. With respect to this point, Saravia[53] has shown in his calculations that the weak structure is produced by some critical points surrounding the Γ point rather than the high-symmetry one and that the piezo-optical properties, especially the changes for [001] stress and parallel polarization, are explained by this critical-point set.

B. E_2 Structures

The experimental results obtained from the line-shape analysis in this spectral region are summarized in Table XII, together with the data previously obtained with other modulation techniques. Lukeš et al.[90] and Matatagui et al.[15] have shown that the E_2 structures consist of two critical points of type M_1 and M_2 from the lower energy side. Their results do not conflict with our results. However, Welkowsky and Braunstein[16] have shown that the $E_2(1)$ critical point is of type M_2 from the wavelength-modulated reflectivity measurements, which does not agree with our results. As for the symmetry assignment, Zucca and Shen[17] have shown that the $E_2(1)$ and $E_2(3)$ critical points are attributed to the $\Sigma_2^v \rightarrow \Sigma_3^c$ and $\Delta_5^v \rightarrow \Delta_1^c$ transitions, respectively, which is in agreement with our results of symmetry analysis.

Our measurements can be compared to the energy-band-structure calculations of Si. The representative results of the calculations are listed in Table XIII. Most of the calculated results has assigned the E_2 critical points to the $X_4^v \rightarrow X_1^c$ and $\Sigma_2^v \rightarrow \Sigma_3^c$ transitions. Brust[3] has shown that the E_2 structures consist of an M_1 critical point at the X point and an M_2 critical point on the Σ axis near $\vec{K}_0 = (0.4, 0.4, 0.0)$. Cardona and Pollak[60] have shown that the $X_4^v \rightarrow X_1^c$ transition is at 4.40 eV and the $\Sigma_2^v \rightarrow \Sigma_3^c$ transition at 4.37 eV. Moreover, Saravia and Brust[49] have shown that the E_2 structures are mainly contributed by an M_2 critical point at $(\frac{5}{12}, \frac{5}{12}, 0)$ on the Σ axis, an M_1 critical point at $(\frac{7}{12}, \frac{7}{12}, \frac{1}{4})$ near the KL line, and an M_2 critical point at $(\frac{13}{24}, \frac{1}{4}, \frac{1}{4})$ in the ΓXUL plane. We cannot estimate all of the above results by our experimental results, because the calculated ones scatter widely. However, it should be reconsidered that the critical point on the Σ axis is of type M_2.

We have shown that the $E_2(3)$ critical point is one dimensional from

TABLE XII. Critical-point parameters of Si in the energy range of E_2 transitions as obtained from electroreflectance (ER), wavelength-modulated reflectance (WMR), and thermoreflectance (TR) measurements.

		This work[a] ER (90 K)	Lukeš et al.[b] ER (90 K)	Zucca and Shen[c] WMR (5 K)	Welkowsky et al.[d] WMR (80 K)	Matatagui et al.[e] TR (77 K)
	E_g (eV)	4.336 ± 0.010	4.38 ± 0.02	4.44 ± 0.01	4.26	4.30
	Γ (eV)	0.066 ± 0.010				
$E_2(1)$	Symmetry	$\Sigma_2^v \rightarrow \Sigma_3^c$		$\Sigma_2^v \rightarrow \Sigma_3^c$	$\Sigma_2^v \rightarrow \Sigma_3^c$	
	Type	M_1^{3D}	M_1^{3D}		M_2^{3D}	M_1^{3D}
	(reduced-mass relations)	$1/\mu_{T2} + 1/\mu_L = 4/\mu_{T1}$ $\mu_{T1} > 0$, $\mu_{T2}\mu_L < 0$				
	E_g (eV)	4.459 ± 0.010			4.46	
	Γ (eV)	0.086 ± 0.010				
$E_2(2)$	Symmetry				$\Delta_5^v \rightarrow \Delta_1^c$ near X	
	Type	M_1^{3D}			M_1^{3D}	
	(reduced-mass relations)					

TABLE XII. *(Continued)*

		This work[a] ER (90 K)	Lukeš et al.[b] ER (90 K)	Zucca and Shen[c] WMR (5 K)	Welkowsky et al.[d] WMR (80 K)	Matatagui et al.[e] TR (77 K)
	E_g (eV)	4.598 ± 0.010	4.65 ± 0.05	4.60 ± 0.03		4.55
	Γ (eV)	0.071 ± 0.010				
$E_2(3)$	Symmetry	$\Delta_5^v \rightarrow \Delta_1^c$ near X		$\Delta_5^v \rightarrow \Delta_1^c$		
	Type	M_2^{3D}	M_2^{3D}			M_2^{3D}
	(reduced-mass relations)	$\mu_L << \|\mu_T\|$ $\mu_T < 0, \mu_L > 0$				

[a] Reference 35.
[b] Reference 90.
[c] Reference 17.
[d] Reference 16.
[e] Reference 15.

TABLE XIII. Calculated critical-point energies of Si in the E_2 spectral region (in eV).

Transition	Brust[a]	Cardona and Pollak[b]	Cohen and Bergstresser[c]	Kane[d]	Herman et al.[e]		
					E (PERT)	E (PERT)	E (PERT)
$\Gamma^v_{25'} \rightarrow \Gamma^c_{2'}$	3.8		3.8	3.3	3.35	3.8	4.2
$\Sigma^v_2 \rightarrow \Sigma^c_3$	4.4	4.37			4.0	4.15	4.3
$X^v_4 \rightarrow X^c_1$	4.0	4.40	4.0	4.1	4.0	4.05	4.1
$L^v_{3'} \rightarrow L^c_3$	5.4		5.2	5.3	5.05	5.0	4.95

Transition	Dresselhaus and Dresselhaus[f]	Van Vechten[g]	Stukel and Euwema[h]	Zucca et al.[i]	Van Dyke[j]	
					OPW	Pseudo
$\Gamma^v_{25'} \rightarrow \Gamma^c_{2'}$	3.74	4.10	2.75		3.65	3.63
$\Sigma^v_2 \rightarrow \Sigma^c_3$	4.43		4.15	4.41		
$X^v_4 \rightarrow X^c_1$	3.74	4.50	4.00		3.97	4.01
$L^v_{3'} \rightarrow L^c_3$	5.30	5.90	5.01		5.04	4.71

[a] Reference 3.
[b] Reference 60.
[c] Reference 113.
[d] Reference 47.
[e] Reference 52.
[f] Reference 48.
[g] Reference 115.
[h] Reference 102.
[i] Reference 50.
[j] Reference 116.

the mass relation, $\mu_L \ll |\mu_T|$. This one-dimensional critical point may not be related to the one-dimensional Penn gap.[117] Cardona and Pollak[118] have discussed more precisely about the one-dimensional critical point in the E_2 region.

C. Synthesis: Interband energy contours of Si

Figures 19 and 20 show the $E_{4-5}(\vec{k})$ energy contours of Si calculated by Kane[47] and by Saravia and Brust,[49] respectively. In Figs. 19 and 20, the contours are written to be nearly flat along the Λ direction, which is consistent with our experimental results, $\mu_T \ll |\mu_L|$. The difference lies in the type of critical point at the L point; i.e., the M_1 type in our measurements and the M_0 type in their calculated results.

The flatness along the Δ direction is shown by Brust,[59] Kane (see Fig. 19),[47] and Saravia and Brust (see Fig. 20).[49] However, this prediction is incompatible with our results, $\mu_L \ll |\mu_T|$.

The contour lines near the critical point on the Σ axis shown in Fig. 18 appear to be similar to those shown in Figs. 19 and 20. However, they are quite different from each other: the critical point is of type M_1 in the experimental results (Fig. 18) and of type M_2 in the calculated results (Figs. 19 and 20).

Finally, we wish to construct the "minimal set[2]" of critical points. The critical points are constrained by topological considerations to satisfy certain criteria, which is called the Morse's topological relations. Following Phillips,[2] this relation for the three-dimensional topological space can be written

$$N(M_0) \geqq 1,$$
$$N(M_1) \geqq 2 + N(M_0),$$
$$N(M_2) \geqq 2 + N(M_3), \qquad (72)$$

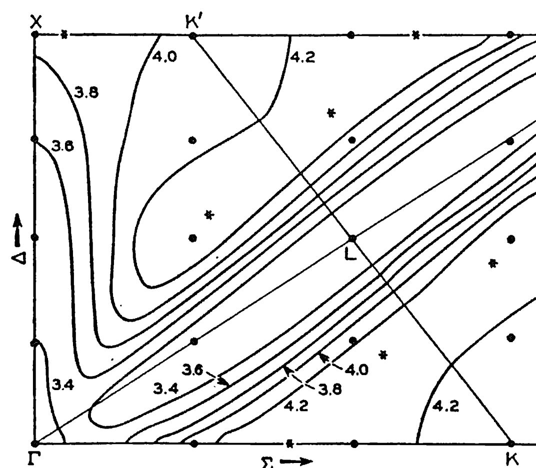

FIG. 19. The calculated $E_{4-5}(\vec{k})$ energy contours of Si in the ΓKL and ΓXUL planes. Asterisks indicate optical critical points. (After Kane.[47])

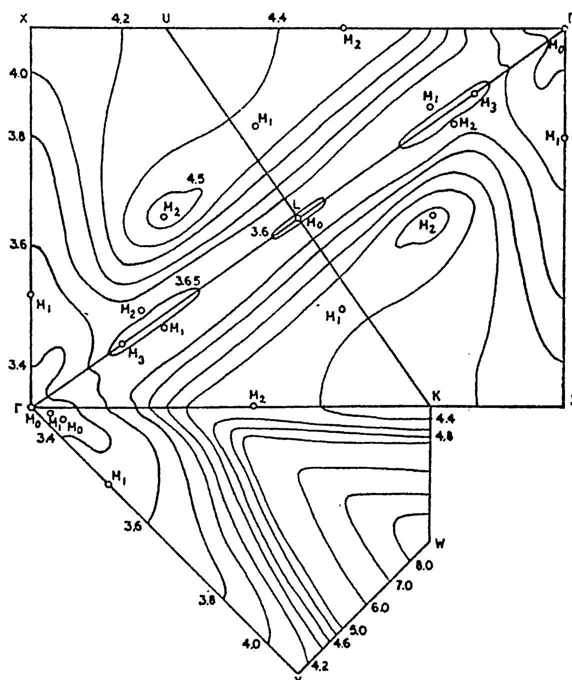

FIG. 20. The calculated $E_{4-5}(\vec{k})$ energy contours of Si in the ΓKWX, ΓKL, and ΓXUL planes. Open circles indicate optical critical points. (After Saravia and Brust.[49])

$$N(M_3) \geqq 1,$$

$$N(M_0) + N(M_2) = N(M_1) + N(M_3),$$

where $N(M_\ell)$ is the number of M_ℓ critical point. The symmetry set satisfying these equations is called the "minimal set". It is of interest that the number of M_0 critical points plus the number of M_2 critical points must equal the number of M_1 critical points plus the number of M_3 critical points.

In constructing the minimal set, one must take into account the number of equivalent critical points in the Brillouin zone. All points in the Brillouin zone may be divided into classes by the symmetry properties.[110] For diamond-type crystals, all points in the first Brillouin zone may be divided into eight groups Γ, Δ, Λ, Σ, C, O, J, A and all points on the first-Brilluoin-zone surfaces may be divided into seven groups X, L, W, S, Z, B, Q. The symmetries and the number of equivalent points for these groups are listed in Table XIV.

Using Eq. (72), Table XIV, and the experimentally obtained critical points, we can find the minimal set for the $E_{4-5}(\vec{k})$ interband energy surfaces

$$\begin{aligned} M_0 &: \ E_0' \, [\, 1\,\Gamma,\ 6\,\Delta \text{ near } \Gamma,\ 12\,\Sigma \text{ near } \Gamma \,], \\ M_1 &: \ E_1 \, [\, 4\,L \,],\ E_2(1) \, [\, 12\,\Sigma \,],\ E_2(2) \, [\, 6\,W \,], \\ M_2 &: \ E_2(3) \, [\, 6\,\Delta \,], \\ M_3 &: \ [\, 3\,X \,], \end{aligned} \tag{73}$$

where Γ: $\Gamma^v_{25'} \rightarrow \Gamma^c_{15}$, Δ: $\Delta^v_5 \rightarrow \Delta^c_1$, Σ: $\Sigma^v_2 \rightarrow \Sigma^c_3$, L: $L^v_{3'} \rightarrow L^c_1$, and X: $X^v_4 \rightarrow X^c_1$. The total number of critical points in the above minimal set is 50. In the minimal set, E_0' consists of some points at Γ and along Δ and Σ. E_1 consists of L points. $E_2(1)$, $E_2(2)$, and $E_2(3)$ consist of Σ, W, and Δ points, respectively. These results are consistent with the experimental results.

TABLE XIV. Symmetry group of $\vec{K}_0$ for the first Brillouin zone in diamond-type (Fd3m) crystals.

Internal points (Symmorphic group)

Point	Coordinates	Schönflies	(International)	Number
Γ	(0, 0, 0)	O_h	(m3m)	1
Δ	$(0, 0, k_0)$	C_{4v}	(4mm)	6
Λ	(k_0, k_0, k_0)	C_{3v}	(3m)	8
Σ	$(k_0, k_0, 0)$	C_{2v}	(mm2)	12
C	(k_0, k_0, k_1)	C_{1h}	(m)	24
O	$(k_0, k_1, 0)$	C_{1h}	(m)	24
J	(k_0, k_1, k_0)	C_{1h}	(m)	24
A	(k_0, k_1, k_2)	C_1	(1)	48

Surface points (Non-symmorphic group)

Point	Coordinates	Schönflies	(International)	Number
X	(0, 0, 1)			3
L	$(\frac{1}{2}, \frac{1}{2}, \frac{1}{2})$	D_{3d}		4
W	$(\frac{1}{2}, 1, 0)$			6
S	$(k_0, 1, k_0)$			12
Z	$(k_0, 1, 0)$			12
B	$(k_0, 1, k_1)$			24
Q	$(\frac{1}{2}, \frac{1}{2}+k_0, \frac{1}{2}-k_0)$	C_2		24

VII. CONCLUSIONS

A. Theory

(i) A method of the symmetry analysis on optical-critical points was explained, i.e., the location $\vec{K}_0$ can be deduced from the polarization dependences and the line shapes of low-field ER spectra. Polarization dependences of longitudinal ER spectrum on the $(1\bar{1}0)$ face were calculated and summarized in Table III for high-symmetry Γ, Δ, Λ, L, and Σ critical points in diamond-type crystals. Criteria of the symmetry analysis were also listed in Table III.

(ii) Uniaxial-stress effects on low-field ER spectra were calculated for the degenerate $\Lambda_3^v - \Lambda_1^c$ (or $L_{3'}^v - L_1^c$), $\Delta_5^v - \Delta_1^c$, and $\Gamma_{25'}^v - \Gamma_{15}^c$ critical points. The results were summarized in Tables V, VI, and VII, respectively.

B. Experiment

(iii) The 3.4 eV optical structures of Si were found to consist of two critical points with different origin, E_0' and E_1, from the line-shape analysis. The types of the E_0' and E_1 critical points were determined to be the three-dimensional M_0 and M_1, respectively. Energies and broadening parameters were also obtained and listed in Table VIII.

(iv) The location of the E_0' critical point was not determined uniquely by this method of symmetry analysis. However, only a possibility $\Delta_5^v \rightarrow \Delta_1^c$ near the Γ point has remained according to the results of the stress measurements. In this case, the effective-mass relations may be $\mu_T/\mu_L = 1-3$, $\mu_T > 0$, $\mu_L > 0$.

(v) The E_1 critical point was assigned conclusively to the $\Lambda_3^v \rightarrow \Lambda_1^c$ or $L_{3'}^v \rightarrow L_1^c$ transition. The reduced-mass relations were $\mu_T \ll |\mu_L|$, $\mu_T > 0$, and $\mu_L < 0$. Moreover, we found from the mass relation,

$\mu_T << |\mu_L|$, that the critical point may be nearly two-dimensional M_0 type.

(vi) The pair-band deformation potential parameters for the degenerate $\Lambda_3^v - \Lambda_1^c$ critical point have been determined from the uniaxial stress measurements. These values were presented in Table IX.

(vii) Three structures were found in the E_2 spectral region from the line-shape analysis. The types of these critical points were determined to be the three-dimensional M_1, M_1, and M_2, respectively. Energies and broadening parameters were also obtained and listed in Table XII.

(viii) The symmetry location of the $E_2(1)$ critical point was conclusively determined to be the $\Lambda_2^v \rightarrow \Lambda_3^c$ transition. The reduced-mass relations were $1/\mu_{T2} + 1/\mu_L = 4/\mu_{T1}$, $\mu_{T1} > 0$, $\mu_{T2}\mu_L < 0$.

(ix) The $E_2(3)$ critical point were tentatively attributed to the $\Delta_5^v \rightarrow \Delta_1^c$ transition near the X point. The reduced-mass relations were $\mu_L << |\mu_T|$, $\mu_T < 0$, $\mu_L > 0$. Moreover, we found from the mass relation, $\mu_L << |\mu_T|$, that the critical point may be nearly one dimensional.

(x) The $E_{4-5}(\vec{k})$ energy contours of Si have been constructed from the experimental results, for the first time.

APPENDIX A: COMPLEX SERAPHIN COEFFICIENTS FOR THE THREE-PHASE SYSTEM

In this Appendix, we show the complex Seraphin coefficients for a three-phase system. Consider a system consisting of three parallel layers denoted by subscripts 0, 1, 2 as shown in Fig. 21. Let each layer i be described by a complex refractive index,

$$N_i = n_i + ik_i = (\epsilon_{1,i} + i\epsilon_{2,i})^{\frac{1}{2}}, \tag{A1}$$

where n_i is the real refractive index and k_i is the real attenuation index. We take both layers 0 and 2 to be semi-infinite in extent and the thickness of the layer 1 to be d.

If a plane wave propagates from a layer i to the next layer j across the interface, the wave will be divided into a reflected and a refracted parts and the complex reflectivity r_{ij} at the interface can be described by Fresnel's formula. In case of the normal incidence it can be written[119]

$$r_{ij} = \frac{N_j - N_i}{N_j + N_i}. \tag{A2}$$

The reflectivity of the three-phase system can be calculated by considering the multi-reflection in the layer 1 as

$$r = \frac{r_{01} + r_{12}\exp(i\,2\omega N_1 d/c)}{1 + r_{01}r_{12}\exp(i\,2\omega N_1 d/c)}, \tag{A3}$$

where ω is the frequency of the plane wave.

When the properties of the layer 2 is modified by some perturbation, the refractive index N_2 will change. If this change is sufficiently small, the resultant change ΔN_2 may be represented as a first-order correction. If once this first-order correction is known, the complex reflectivity will be given to first order by

$$\frac{\Delta r}{r} = \frac{[1 - (r_{01})^2][1 - (r_{12})^2]\exp(i\ 2\omega N_1 d/c) \times \Delta\epsilon}{4(N_2)^2[r_{01} + r_{12}\exp(i\ 2\omega N_1 d/c)][1 + r_{01}r_{12}\exp(i\ 2\omega N_1 d/c)]}, \quad \text{(A4)}$$

where the relations,

$$\Delta N_0 = 0, \quad \text{(A5)}$$

$$\Delta N_1 = 0, \quad \text{(A6)}$$

$$\Delta N_2 = (2N_2)^{-1} \times \Delta\epsilon, \quad \text{(A7)}$$

have been used in the calculation.

On the other hand, the complex reflectivity can be defined in the usual manner

$$r = R^{\frac{1}{2}} \exp(i\theta), \quad \text{(A8)}$$

where R and θ are real. Then, we have

$$\frac{\Delta r}{r} = \frac{1}{2}\frac{\Delta R}{R} + i\theta. \quad \text{(A9)}$$

Comparing Eqs. (A4) and (A9), we obtain the three-phase Seraphin coefficients

$$\tilde{C}_s \equiv \alpha - i\beta, \quad \text{(A10)}$$

$$= \frac{[1 - (r_{01})^2][1 - (r_{12})^2]\exp(i\ 2\omega N_1 d/c)}{2(N_2)^2[r_{01} + r_{12}\exp(i\ 2\omega N_1 d/c)][1 + r_{01}r_{12}\exp(i\ 2\omega N_1 d/c)]}. \quad \text{(A11)}$$

As a specific case, the Seraphin coefficients for the usual two-phase system can be obtained by taking $N_1 = N_0$ in Eq. (A11),

$$\tilde{C}_s = \frac{2N_1}{N_2(N_2 + N_1)(N_2 - N_1)}. \quad \text{(A12)}$$

Equations (A11) and (A12) are the same as derived by Aspnes.[120–122]

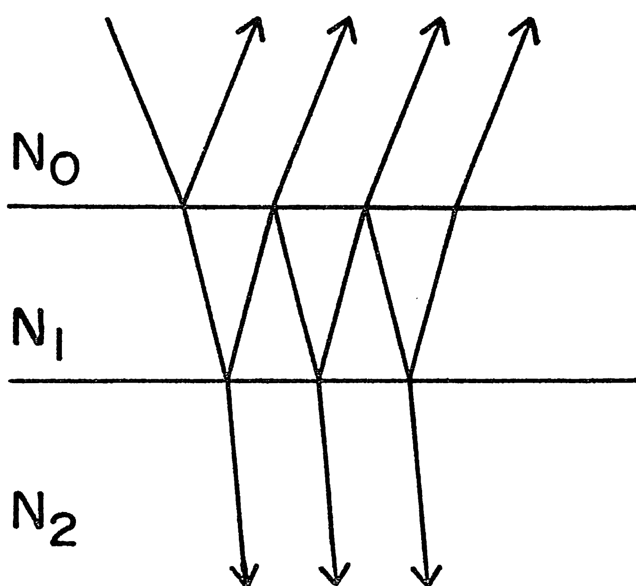

FIG. 21. Schematic diagram of a three-phase optical system. The complex refractive indices of the phases are denoted by N_0, N_1, and N_2.

APPENDIX B. APPLICATION TO DOPING INHOMOGENEITY MEASUREMENTS ON SEMICONDUCTOR SURFACES

In this appendix, we describe the theoretical basis for measuring doping inhomogeneity on semiconductor surfaces by the low-field ER technique.[123−125] The expression of the relative reflectivity change $\Delta R/R$ measured in the low-field modulation limit is given in Eq. (36)

$$\frac{\Delta R}{R}(\hbar\omega, \Gamma) = \mathrm{Re}\left\{ \tilde{C}\,[\alpha(\hbar\omega) - i\beta(\hbar\omega)] \sum_{\tau} i^{\ell-3} L^{\tau}(\hbar\omega + i\Gamma) \right\} F^{\tau} \mathcal{E}^2, \tag{36}$$

where the function $L^{\tau}(\hbar\omega + i\Gamma)$ mainly determines the line shape of ER spectrum, which is given in Eq. (37). The factor F^{τ} in Eq. (36) shows the effects of the polarization of the light and the applied electric field, which is given in Eq. (38). Typical examples of the factor F are listed in Table XV for high-symmetry Γ, Δ, Λ, L, and Σ critical points in diamond-type crystals; where the cases of longitudinal configuration ($\hat{n} \perp \hat{\mathcal{E}}$) with unpolarized light on the (001), (111), and $(1\bar{1}0)$ faces are given.

On the other hand, the relation between the electric field $\hat{\mathcal{E}}$ and the potential ϕ are written in the space-charge region by Poisson equation[34]

$$\mathcal{E}^2 = \frac{2e}{\epsilon_r \epsilon_0}\left[N_d\left(\frac{kT}{e}\exp\left(\frac{e\phi}{kT}\right) - \phi - \frac{kT}{e}\right) + N_a\left(\frac{kT}{e}\exp\left(-\frac{e\phi}{kT}\right) + \phi - \frac{kT}{e}\right)\right], \tag{B1}$$

where N_d and N_a are the ionized donor and acceptor impurity concentration on semiconductor surfaces, respectively. $\epsilon_r \epsilon_0$ is the static dielectric constant. $\frac{kT}{e}$ is the thermal voltage, which is 25.9 mV at $T = 300\,\mathrm{K}$. We consider an n-type sample and neglect the second term of Eq. (B1). In the fully depleted space-charge region ($\phi < 0$), the term $(\frac{kT}{e})\exp(\frac{e\phi}{kT})$ and $\frac{kT}{e}$ are negligible compared to ϕ. Moreover, the inversion layer cannot be formed in the Schottky-barrier, p-n junction, and hetero-junc-

TABLE XV. Electroreflectance form factor F for high symmetry Γ, Δ, Λ, L, and Σ critical points in diamond-type crystals. Longitudinal geometry with unpolarized light is used for the (0 0 1), (1 1 1), and $(1\bar{1}0)$ faces. μ_{T1}, μ_{T2}, and μ_L are defined by Eq. (23).

Critical point location	Pair state symmetry	Low-field electroreflectance form factor F $\hat{\mathcal{E}} \parallel (001)$	$\hat{\mathcal{E}} \parallel (111)$	$\hat{\mathcal{E}} \parallel (1\bar{1}0)$
Γ	U_{4-}	$\frac{1}{\mu} f^0$	$\frac{1}{\mu} f^0$	$\frac{1}{\mu} f^0$
Δ	U_1	$\frac{2}{\mu_T} f^0$	$\frac{2}{3}(\frac{2}{\mu_T}+\frac{1}{\mu_L})\ f^0$	$\frac{1}{2}(\frac{3}{\mu_T}+\frac{1}{\mu_L})\ f^0$
	U_5	$2(\frac{1}{\mu_T}+\frac{1}{\mu_L})\ f^0$	$\frac{4}{3}(\frac{2}{\mu_T}+\frac{1}{\mu_L})\ f^0$	$\frac{1}{2}(\frac{5}{\mu_T}+\frac{3}{\mu_L})\ f^0$
Λ	U_1	$\frac{8}{9}(\frac{2}{\mu_T}+\frac{1}{\mu_L})\ f^0$	$\frac{8}{27}(\frac{8}{\mu_T}+\frac{1}{\mu_L})\ f^0$	$\frac{4}{9}(\frac{5}{\mu_T}+\frac{1}{\mu_L})\ f^0$
	U_3	$\frac{16}{9}(\frac{2}{\mu_T}+\frac{1}{\mu_L})\ f^0$	$\frac{16}{27}(\frac{5}{\mu_T}+\frac{4}{\mu_L})\ f^0$	$\frac{4}{9}(\frac{7}{\mu_T}+\frac{5}{\mu_L})\ f^0$
L	U_{2-}	$\frac{4}{9}(\frac{2}{\mu_T}+\frac{1}{\mu_L})\ f^0$	$\frac{4}{27}(\frac{8}{\mu_T}+\frac{1}{\mu_L})\ f^0$	$\frac{2}{9}(\frac{5}{\mu_T}+\frac{1}{\mu_L})\ f^0$
	U_{3-}	$\frac{8}{9}(\frac{2}{\mu_T}+\frac{1}{\mu_L})\ f^0$	$\frac{8}{27}(\frac{5}{\mu_T}+\frac{4}{\mu_L})\ f^0$	$\frac{2}{9}(\frac{7}{\mu_T}+\frac{5}{\mu_L})\ f^0$

TABLE XV. *(Continued)*

Critical point location	Pair state symmetry	Low-field electroreflectance form factor F		
		$\hat{\mathcal{E}} \parallel (0\,0\,1)$	$\hat{\mathcal{E}} \parallel (1\,1\,1)$	$\hat{\mathcal{E}} \parallel (1\,\bar{1}\,0)$
Σ	U_1	$(\frac{2}{\mu_{T1}}+\frac{1}{\mu_{T2}}+\frac{1}{\mu_L})\, f^0$	$\frac{2}{3}(\frac{2}{\mu_{T1}}+\frac{3}{\mu_{T2}}+\frac{1}{\mu_L})\, f^0$	$\frac{1}{4}(\frac{6}{\mu_{T1}}+\frac{7}{\mu_{T2}}+\frac{3}{\mu_L})\, f^0$
	U_2	$2(\frac{1}{\mu_{T2}}+\frac{1}{\mu_L})\, f^0$	$\frac{4}{3}(\frac{1}{\mu_{T1}}+\frac{1}{\mu_{T2}}+\frac{1}{\mu_L})\, f^0$	$\frac{1}{2}(\frac{2}{\mu_{T1}}+\frac{3}{\mu_{T2}}+\frac{3}{\mu_L})\, f^0$
	U_3	$(\frac{2}{\mu_{T1}}+\frac{1}{\mu_{T2}}+\frac{1}{\mu_L})\, f^0$	$\frac{2}{3}(\frac{2}{\mu_{T1}}+\frac{1}{\mu_{T2}}+\frac{3}{\mu_L})\, f^0$	$\frac{1}{4}(\frac{6}{\mu_{T1}}+\frac{3}{\mu_{T2}}+\frac{7}{\mu_L})\, f^0$

$$f^0 \equiv <0|p_{\gamma\alpha}|\psi_{\gamma\alpha}>^2$$

tion configurations, because the minority carriers, which diffuse from the bulk and are excited thermally or optically in the space-charge region, are extracted at the interface. Thus, Eq. (B1) becomes

$$\mathcal{E}^2 = -\frac{2e}{\epsilon_r \epsilon_0} N_d \phi\,; \quad \phi < 0. \tag{B2}$$

a. Modulation in the Schottky-Barrier Configuration

When an external voltage V_{ext} is applied to a Schottky-barrier, the surface potential ϕ_s may be written

$$\phi_s = V_{int} + V_{ext}, \tag{B3}$$

where V_{int} is the built-in potential in the absence of external voltage. V_{ext} consists of dc bias V_{dc} and ac-modulation voltage $V_{ac}(t)$. Since a time-varying signal measured by a phase-sensitive detection is observed as the root-mean-square value of the fundamental harmonic component (rms,fun) of the ac signal, the relative reflectivity change measured experimentally can be written using Eqs. (36), (B2), and (B3)

$$\frac{\Delta R}{R}(\hbar\omega, \Gamma) = \left[\frac{\Delta R}{R}(\hbar\omega, \Gamma, t)\right]_{rms,fun}, \tag{B4}$$

$$= \mathrm{Re}\left\{ \tilde{C}\,[\alpha(\hbar\omega) - i\beta(\hbar\omega)] \sum_{\tau} i^{\ell - 3} L^{\tau}(\hbar\omega + i\Gamma)\right\} \times \frac{2eF}{\epsilon_r \epsilon_0} \times N_d\,[V_{ac}(t)]_{rms,fun}. \tag{B5}$$

As shown in Eq. (B5), $\Delta R/R$ is proportional directly to the impurity concentration N_d, if we hold the modulation voltage $V_{ac}(t)$ constant.

b. Modulation in the Electrolyte-Semiconductor Configuration

The electric properties of the electrolyte-semiconductor interface may be similar to those of the p-n junction.[126] The relation between the

externally applied voltage V_{ext} and the surface potential ϕ_s can be written[127]

$$\phi_s = V_{int} + V_{ext} - V_{Gouy} - V_{elec}, \tag{B6}$$

$$= [V_{int} + V_{dc} - V_{Gouy,dc} - V_{elec,dc}] + [V_{ac}(t) - V_{Gouy}(t) - V_{elec}(t)], \tag{B7}$$

where V_{Gouy} is the potential drop in the Gouy layer, which is the space-charge region in the electrolyte. A dc bias applied externally is divided into the semiconductor-space-charge region, the Gouy layer, and the electrolyte. However, it is the purpose of dc bias for the semiconductor-space-charge region to be fully depleted and the dc bias does not affect the low-field ER spectra measured experimentally. The ac component $V_{ac}(t)$ may be also divided into the surface potential $\phi_s(t)$, the Gouy layer $V_{Gouy}(t)$, and the electrolyte $V_{elec}(t)$. However, the latter two potential drops may be negligible compared to the surface potential $\phi_s(t)$, since the solute effectively provides a lot of carriers (10^{22} cm^{-3}) compared to the majority carriers in the usual semiconductors ($10^{14}-10^{21}$ cm^{-3}). Therefore, the relative reflectivity change $\Delta R/R$ may be written in the same form as Eq. (B5).

c. Doping Inhomogeneity Measurements on Semiconductor Surfaces

When we fix the orientation of the applied electric field and the polarization of the probe light, we can find the relation

$$\frac{[\frac{\Delta R}{R}]_{\hbar\omega,i}}{N_{d,i}V_{ac,i}} = \frac{[\frac{\Delta R}{R}]_{\hbar\omega,0}}{N_{d,0}V_{ac,0}}, \tag{B8}$$

where $[\frac{\Delta R}{R}]_{\hbar\omega,i}$ shows the relative reflectivity change measured at point i using the probe light of energy $\hbar\omega$. $N_{d,i}$ and $V_{ac,i} = [V_{ac,i}(t)]_{rms,fun}$ are the doping concentration and the ac-modulation voltage at point i,

respectively. In Eq. (B8), $N_{d,0}V_{ac,0}$ can be determined from the best-fit analysis on the low-field ER spectrum measured at point 0, $[\frac{\Delta R}{R}(\hbar\omega, \Gamma)]_0$. Therefore, the doping concentration $N_{d,i}$ at any point i on the sample surface can be immediately obtained from $[\frac{\Delta R}{R}]_{\hbar\omega,i}$ and $V_{ac,i}$.

d. Estimation of the Absolute Values of Doping Concentrations

From Eqs. (37) and (B5), the product $N_d\,[V_{ac}(t)]_{rms,fun}$ may be written

$$N_d\,[V_{ac}(t)]_{rms,fun} = 4\pi\epsilon_0 \frac{4\pi^2 m^2}{e^4\hbar^4}\frac{8}{\pi^2}\left|\frac{\hbar^6}{8\mu_{T1}\mu_{T2}\mu_L}\right|^{\frac{1}{2}}\frac{\epsilon_r\epsilon_0}{2eF}\,C, \tag{B9}$$

where C is the energy-independent amplitude factor of the low-field ER spectrum, which can be determined from the best-fit analysis.

As an example, we estimate Eq. (B9) for Si crystal. When we use the E_1 structure (Λ critical point with U_3 symmetry in Si), the longitudinal ER geometry, unpolarized light, and the $(1\bar{1}0)$ face for the plane of reflection, the ER form factor F may be written from Table XV

$$F = \frac{4}{9}\left(\frac{7}{\mu_T} + \frac{5}{\mu_L}\right) f^0, \tag{B10}$$

$$= \frac{28}{9}\frac{1}{\mu_T} f^0; \quad (\mu_{T1} = \mu_{T2} = \mu_T,\ \mu_T << |\mu_L|,\ \mu_T > 0,\ \mu_L < 0) \tag{B11}$$

where f^0 is the momentum matrix element between the Λ_3 valence and the Λ_1 conduction bands and, in this case,[60] $f^0 = (1.2\hbar/a_B)^2$. Using the values, $\epsilon_r = 12$,[34] $|\mu_L| = 9.6$,[48] and Eq. (B11), equation (B9) becomes

$$N_d\,[V_{ac}(t)]_{rms,fun} = 2.4 \times 10^{96}\,C \quad [V/m^3]. \tag{B12}$$

REFERENCES

1. L. Van Hove, Phys. Rev. 89, 1189 (1953).
2. J. C. Phillips, Phys. Rev. 104, 1263 (1956).
3. D. Brust, Phys. Rev. 134, A1337 (1964).
4. B. O. Seraphin and R. B. Hess, Phys. Rev. Lett. 14, 138 (1965).
5. B. O. Seraphin, R. B. Hess, and N. Bottka, J. Appl. Phys. 36, 2242 (1965).
6. B. O. Seraphin and N. Bottka, Phys. Rev. 139, A560 (1965).
7. M. Cardona, Modulation Spectroscopy (Academic, New York, 1969).
8. B. O. Seraphin, R. L. Aggarwal, D. F. Blossey, P. Handler, B. Batz, I. Balslev, D. E. Aspnes, and N. Bottka, in Semiconductors and Semimetals, edited by R. K. Willardson and A. C. Beer (Academic, New York, 1972), Vol. 9.
9. W. E. Engeler, H. Fritzsche, M. Garfinkel, and J. J. Tiemann, Phys. Rev. Lett. 14, 1069 (1965).
10. G. W. Gobeli and E. O. Kane, Phys. Rev. Lett. 15, 142 (1965).
11. D. D. Sell and E. O. Kane, Phys. Rev. 185, 1103 (1969).
12. A. Gavini and M. Cardona, Phys. Rev. B 1, 672 (1970).
13. B. Batz, Solid State Commun. 4, 241 (1966).
14. B. Batz, Solid State Commun. 5, 985 (1967).
15. E. Matatagui, A. G. Thompson, and M. Cardona, Phys. Rev. 176, 950 (1968).
16. R. Braunstein and M. Welkowsky, in Proceedings of the Tenth International Conference on the Physics of Semiconductors, Cambridge, U. S. A., edited by S. P. Keller, J. C. Hensel, and F. Stern, (United States Atomic Energy Commission, Cambridge, U. S. A., 1970), p. 439; M. Welkowsky and R. Braunstein, Phys. Rev. B 5, 497 (1972).
17. R. R. L. Zucca and Y. R. Shen, Phys. Rev. B 1, 2668 (1970).

18. M. Welkowsky and R. Braunstein, Rev. Sci. Instrum. 43, 399 (1972).

19. D. E. Aspnes and J. E. Rowe, Solid State Commun. 8, 1145 (1970); Phys. Rev. B 5, 4022 (1972).

20. D. E. Aspnes and J. E. Rowe, Phys. Rev. Lett. 27, 188 (1971).

21. D. E. Aspnes, Phys. Rev. Lett. 28, 168 (1972).

22. D. E. Aspnes, Phys. Rev. Lett. 28, 913 (1972).

23. D. E. Aspnes, Surf. Sci. 37, 418 (1973).

24. J. C. Phillips, Phys. Rev. 146, 584 (1966).

25. B. O. Seraphin, in Optical Properties of Solids, edited by E. D. Haidemenakis (Gordon and Breach, New York, 1969), Chap. IX, p. 213.

26. N. Bottka and J. E. Fischer, Phys. Rev. B 3, 2514 (1971).

27. V. Rehn, Surf. Sci. 37, 443 (1973).

28. R. Enderlein, in Proceedings of the Twelfth International Conference on the Physics of Semiconductors, Stuttgart, Federal Republic of Germany, edited by M. Pilkuhn (Teubner, Stuttgart, 1974), p. 161.

29. D. E. Aspnes and A. A. Studna, Phys. Rev. B 7, 4605 (1973).

30. D. E. Aspnes, Phys. Rev. B 12, 2297 (1975).

31. K. Kondo and A. Moritani, Phys. Rev. B 14, 1577 (1976); K. Kondo, A. Moritani, C. Hamaguchi, and J. Nakai, Solid State Commun. 15, 1525 (1974).

32. I. Goroff and L. Kleinman, Phys. Rev. 132, 1080 (1963).

33. U. Gerhardt, Phys. Rev. Lett. 15, 401 (1965); Phys. Status Solidi 11, 801 (1965).

34. S. M. Sze, Physics of Semiconductor Devices (John Wiley & Sons, New York, 1969).

35. K. Kondo and A. Moritani, Phys. Rev. B 15, (1977). (to be published)

36. J. Tauc and A. Abrahám, in Proceedings of the International Conference on the Physics of Semiconductors, Prague, Czechoslovakia (Czechoslovakian Academy of Sciences, Prague, 1961), p. 375; J. Phys. Chem. Solids 20, 190 (1961).

37. J. Koo, Y. R. Shen, and R. R. L. Zucca, Solid State Commun. 9, 2229 (1971).

38. F. H. Pollak and G. W. Rubloff, Phys. Rev. Lett. 29, 789 (1972).

39. B. O. Seraphin, Phys. Rev. 140, A1716 (1965).

40. B. O. Seraphin and N. Bottka, Phys. Rev. 145, 628 (1966).

41. M. Cardona, F. H. Pollak, and K. L. Shaklee, J. Phys. Soc. Jpn. Suppl. 21, 89 (1966); M. Cardona, K. L. Shaklee, and F. H. Pollak, Phys. Rev. 154, 696 (1967).

42. A. K. Ghosh, Phys. Lett. 23, 36 (1966).

43. J. W. Grover and P. Handler, Phys. Rev. B 9, 2600 (1974).

44. R. A. Forman, D. E. Aspnes, and M. Cardona, J. Phys. Chem. Solids 31, 227 (1970).

45. E. Schmidt and K. Vedam, Solid State Commun. 9, 1187 (1971).

46. F. H. Pollak and M. Cardona, Phys. Rev. 172, 816 (1968).

47. E. O. Kane, Phys. Rev. 146, 558 (1966).

48. G. Dresselhaus and M. S. Dresselhaus, Phys. Rev. 160, 649 (1967).

49. L. R. Saravia and D. Brust, Phys. Rev. 171, 916 (1968).

50. R. R. L. Zucca, J. P. Walter, Y. R. Shen, and M. L. Cohen, Solid State Commun. 8, 627 (1970).

51. D. Brust, J. C. Phillips, and F. Bassani, Phys. Rev. Lett. 9, 94 (1962).

52. F. Herman, R. L. Kortum, C. D. Kuglin, and R. A. Short, in Quantum Theory of Atoms, Molecules and the Solid State, edited by P. O. Löwdin (Academic, New York, 1966), p. 381; J. Phys. Soc. Jpn. Suppl. 21, 7 (1966).

53. L. R. Saravia, J. Phys. Chem. Solids 35, 1469 (1974).

54. J. C. Phillips, Phys. Rev. 125, 1931 (1962).

55. J. C. Phillips, Phys. Rev. 133, A452 (1964).

56. J. C. Phillips, in Solid State Physics, edited by F. Seitz and D. Turnbull (Academic, New York, 1966), Vol. 18, p. 55.

57. D. Brust, M. L. Cohen, and J. C. Phillips, Phys. Rev. Lett. 9, 389 (1962).

58. M. L. Cohen and J. C. Phillips, Phys. Rev. 139, A912 (1965).

59. D. Brust, Phys. Rev. 139, A489 (1965).

60. M. Cardona and F. H. Pollak, Phys. Rev. 142, 530 (1966).

61. J. F. Nye, Physical Properties of Crystals (Oxford, London, 1957).

62. See articles by J. Friedel, G. Harbeke, F. Abelés, B. O. Seraphin, J. Tauc, V. M. Agranovich, J. G. Mavroides, M. Balkanski, H. Pick, W. E. Spicer, J. Ducuing, and C. Flytzanis, in Optical Properties of Solids, edited by F. Abelés (North-Holland, Amsterdam, 1972).

63. E. O. Kane, Phys. Rev. 178, 1368 (1969).

64. L. I. Schiff, Quantum Mechanics (Mcgraw-Hill, New York, 1955).

65. G. F. Koster, J. O. Dimmock, R. G. Wheeler, and H. Statz, Properties of the Thirty-Two Point Groups (MIT, Cambridge, U. S. A., 1963).

66. J. M. Luttinger and W. Kohn, Phys. Rev. 97, 869 (1955).

67. R. J. Elliott, Phys. Rev. 108, 1384 (1957).

68. D. E. Aspnes, Phys. Rev. B 10, 4228 (1974).

69a. E. O. Kane, in Ref. 63, Table XII.

69b. The interband-energy surfaces near the degenerate critical points may not be expressed in the parabolic form as shown in Eq. (22). The exact interband surfaces may be calculated by diagonalizing the kinetic energy Hamiltonian of Eq. (7). An example of the warped surface at the degenerate Γ point has been shown by G. Dresselhaus,

A. F. Kip, and C. Kittel, Phys. Rev. 98, 368 (1955).

70. W. Franz, Z. Naturforsch. 13a, 484 (1958).

71. L. V. Keldysh, Zh. Eksperim. i Teor. Fiz. 34, 1138 (1958) [Sov. Phys. JETP 7, 788 (1958)].

72. D. E. Aspnes, Phys. Rev. 147, 554 (1966).

73. D. E. Aspnes, Phys. Rev. 153, 972 (1967).

74. D. E. Aspnes, P. Handler, and D. F. Blossey, Phys. Rev. 166, 921 (1968).

75. D. E. Aspnes and N. Bottka, in Ref. 8, Chap. 6, p. 457.

76. D. E. Aspnes, in Proceedings of the Eleventh International Conference on the Physics of Semiconductors, Warsaw, Poland (PWN-Polish Scientific, Warsaw, 1972), p. 1371.

77. D. E. Aspnes and A. Frova, Solid State Commun. 7, 155 (1969).

78. J. E. Rowe and D. E. Aspnes, Phys. Rev. Lett. 25, 162 (1970).

79. B. O. Seraphin, in Ref. 8, Chap. 1, p. 1.

80. Y. Hamakawa, P. Handler, and F. A. Germano, Phys. Rev. 167, 709 (1968).

81. C. Herring and E. Vogt, Phys. Rev. 101, 944 (1956).

82. W. H. Kleiner and L. M. Roth, Phys. Rev. Lett. 2, 334 (1959).

83. H. Brooks, in Advances in Electronics and Electron Physics, edited by L. Marton (Academic, New York, 1955), Vol. 7, p. 85.

84. G. E. Pikus and G. L. Bir, Fiz. Tverd. Tela 1, 1642 (1959) [Sov. Phys. Solid State 1, 1502 (1959)]; G. L. Bir and G. E. Pikus, Symmetry and Strain-Induced Effects in Semiconductors (John Wiley & Sons, New York, 1974).

85. I. Balslev, in Ref. 8, Chap. 5, p. 403.

86. D. D. Sell, Surf. Sci. 37, 896 (1973).

87. In cubic crystals, the dilation coefficient may be written

$\delta = e_{xx} + e_{yy} + e_{zz} = (s_{11} + 2s_{12})T/\sqrt{3}$,

which is defined to be positive for dilation and negative for compression. See C. Kittel, *Introduction to Solid State Physics* (John Wiley & Sons, New York, 1953).

88. A. Moritani, K. Kondo, and J. Nakai, Japan. J. Appl. Phys. 15, 1549 (1976).

89. Y. Sasaki, C. Hamaguchi, M. Yamada, and J. Nakai, Rev. Sci. Instrum. 44, 705 (1973).

90. F. Lukeš, E. Schmidt, and J. Humliček, in *Proceedings of the Eleventh International Conference on the Physics of Semiconductors*, Warsaw, Poland (PWN-Polish Scientific, Warsaw, 1972), p. 1382.

91. R. A. Forman, W. R. Thurber, and D. E. Aspnes, Solid State Commun. 14, 1007 (1974).

92. We have calculated the three-phase Seraphin coefficients at room temperature using the reflectivities of Si and Ni measured by the method shown in Ref. 88. The data used in the calculations are as follows: Si: 0—3 eV (Philipp and Taft, Ref. 93), 3—4 eV (Moritani et al., Ref. 88), 4—10 eV (philipp and Taft, Ref. 93), 10—20 eV (Philipp and Ehrenreich, Ref. 94), above 20 eV (extrapolation equation, Ref. 95); Ni: 0—3 eV (Ehrenreich et al., Ref. 96), 3—4 eV (Moritani et al., Ref. 88), 4—20 eV (Vehse and Arakawa, Ref. 97), above 20 eV (extrapolation equation, Ref. 95).

93. H. R. Philipp and E. A. Taft, Phys. Rev. 120, 37 (1960).

94. H. R. Philipp and H. Ehrenreich, Phys. Rev. 129, 1550 (1963).

95. M. Cardona and D. L. Greenaway, Phys. Rev. 133, A1685 (1964). Note that a typographical error in Eq. (5) is corrected by M. Cardona and G. Harbeke, Phys. Rev. 137, A1467 (1965).

96. H. Ehrenreich, H. R. Philipp, and D. J. Olechna, Phys. Rev. 131, 2469 (1963).

97. R. C. Vehse and E. T. Arakawa, Phys. Rev. 180, 695 (1969).

98. See, for example, Table II and Fig. 6 of Ref. 49.

99. H. J. McSkimin, J. Appl. Phys. 24, 988 (1953).

100. R. Zallen and W. Paul, Phys. Rev. 155, 703 (1967).

101. C. V. de Alvarez and M. L. Cohen, Solid State Commun. 14, 317 (1974).

102. D. J. Stukel and R. N. Euwema, Phys. Rev. B 1, 1635 (1970).

103. D. Brust and L. Liu, Phys. Rev. 154, 647 (1967).

104. See Table IX of Ref. 63.

105. D. E. Aspnes and A. A. Studna, Solid State Commun. 11, 1375 (1972).

106. We have calculated the three-phase Seraphin coefficients at 90 K by the method shown in Ref. 88. In the calculations, values of the reflectivities of Si and Ni measured at room temperature and at 77 K were used for energies outside the range between 3.0 and 5.0 eV. The data are as follows: Si: 0—3 eV (Philipp and Taft, Ref. 93, room temperature), 3—5 eV (Kondo and Moritani, unpublished, 90 K), 5—10 eV (Philipp and Taft, Ref. 93, room temperature), 10—20 eV (Philipp and Ehrenreich, Ref. 94, room temperature), above 20 eV (extrapolation equation, Ref. 95); Ni: 0—3 eV (Hanus et al., Ref. 107, 77 K), 3—5 eV (Kondo and Moritani, unpublished, 90 K), 5—10 eV (Hanus et al., Ref. 107, 77 K), 10—20 eV (Vehse and Arakawa, Ref. 97, room temperature), above 20 eV (extrapolation equation, Ref. 95). The calculated results will not be affected by this approximation.

107. J. Hanus, J. Feinleib, and W. J. Scouler, Phys. Rev. Lett. 19, 16 (1967).

108. K. Kondo and A. Moritani, (unpublished).

109. Although it has been shown by Kane (Ref. 47), by Herman et al. (Ref. 52), and by Saravia and Brust (Ref. 49) that the $X_4^v \rightarrow X_1^c$ transition has a weak contribution to the optical structures in the

E_2 region, we consider this one as one of the possibilities. If we neglect the $\vec{k}$-linear term at the X point, the $X_4^v - X_1^c$ critical point has the same polarization dependences as the Δ critical point with U_5 symmetry (see Table III).

110. See, for example, C. J. Bradley and A. P. Cracknell, The Mathematical Theory of Symmetry in Solids (Clarendon, Oxford, 1972).

111. K. Kondo and A. Moritani, in Proceedings of Taormina Research Conference on the Structure of Matter, Taormina, Italy (Il Nuovo Cimento, Italy,). (to be published)

112. J. S. Kline, F. H. Pollak, and M. Cardona, Helv. Phys. Acta 41, 968 (1968).

113. M. L. Cohen and T. K. Bergstresser, Phys. Rev. 141, 789 (1966).

114. E. O. Kane, Phys. Rev. B 4, 1910 (1971).

115. J. A. Van Vechten, Phys. Rev. 187, 1007 (1969).

116. J. P. Van Dyke, Phys. Rev. B 5, 1489 (1972).

117. D. R. Penn, Phys. Rev. 128, 2093 (1962).

118. M. Cardona and F. H. Pollak, The Physics of Opto-Electronic Materials (Plenum, New York, 1971), p. 81.

119. See, for example, G. Harbeke, in Ref. 62, p. 21.

120. D. E. Aspnes, J. Opt. Soc. Am. 63, 1380 (1973).

121. D. E. Aspnes, C. G. Olson, and D. W. Lynch, J. Appl. Phys. 47, 602 (1976).

122. D. E. Aspnes, in Optical Properties of Solids: New Developments, edited by B. O. Seraphin (North-Holland, Amsterdam, 1976), Chap. 15, p. 799.

123. R. Sittig and W. Zimmermann, Phys. Status Solidi (a) 12, 633 (1972).

124. R. Sittig, Surf. Sci. 37, 987 (1973).

125. H. Yokomoto, K. Kondo, and J. Nakai, Japan. J. Appl. Phys. 15, 2137

(1976).

126. M. Cardona, in Ref. 7. See Sec. 25 *c*.

127. D. E. Aspnes and A. Frova, Phys. Rev. B 2, 1037 (1970).

VITA

Kazuo Kondo was born in Kyoto, Japan, on December 19, 1948. He graduated from Kozu High School, Osaka, in March, 1967 and entered Osaka University in April, 1968. He graduated from Osaka University in March of 1972 and entered the Graduate School of Osaka University in April of that year. He received the Master of Engineering degree in Electronics in March of 1974 from Osaka University.

He is a member of the Physical Society of Japan and the Japan Society of Applied Physics.